Università degli Studi di Torino
Doctoral School of the University of Torino
PhD Programme in Chemical and Materials Sciences XXXV Cycle

ZrO_2/CeO_2-based catalysts: understanding their structural and chemical role towards CO_2 valorisation reactions

Davide Salusso

Supervisor:
Prof. Silvia Bordiga

Università degli Studi di Torino

Doctoral School of the University of Torino

PhD Programme in Chemical and Materials Sciences XXXV cycle

ZrO_2/CeO_2-based catalysts: understanding their structural and chemical role towards CO_2 valorisation reactions

Candidate: **Davide Salusso**

Supervisor: Prof. **Silvia Bordiga**

Jury Members:

Prof. **Maria Cristina Paganini**
Università degli studi di Torino
Dipartimento di Chimica

Prof. **Paolo Ghigna**
Università degli Studi di Pavia
Dipartimento di Chimica

Prof. **Anatoly Frenkel**
Stony Brook University
Department of Materials Science and Chemical Engineering

Head of the Doctoral School: Prof. Alberto Rizzuti
PhD Programme Coordinator: Prof. Bartolome Civalleri

Torino, 2022

Table of Contents

1 Introduction

1.1 CO_2: Excess of everything is bad

"Excess of everything is bad". This old proverb should remind to everyone, scientists and not, that CO_2 itself is not a problem. If we look at the CO_2 atmospheric concentration in the past hundreds of thousands of years, it is immediately clear as its concentration oscillated between 280 and 170 ppm, leading to warmer and colder ages, respectively.[1] The relation between CO_2 concentration and the planet average temperature, is a direct consequence of the molecule chemical configuration. CO_2 belongs to the greenhouse gases family containing all the molecules (e.g. H_2O, CH_4, N_2O, O_3) able to absorb and emit energy in the thermal infrared range.[1–3] This particular property occurs thanks to the molecule (non-symmetrical) electrical charges distribution during its vibration. This means that the concentration of CO_2 in the atmosphere, summed with the one of the other greenhouse gases, controls the amount of IR thermal radiation emitted by our planet after sun irradiation. Therefore, coming back to the proverb, the presence of CO_2 in our atmosphere is mandatory for having a planet with average temperature above 0°C however, having an excess of CO_2 is not a good thing. In the last centuries, the level of CO_2 increased to more than 400 ppm, inducing a constant increase of our planet average temperature.[1] It is then clear than we are not crucifying carbon dioxide, but rather its excess in our atmosphere.

For understanding the origin of CO_2 atmospheric excess, we should quickly analyse CO_2 natural cycle. With a rapid balance it can be found as ground and sea life emit 439 and 332 Gt/y of CO_2, respectively compensated with an absorption rate of 450 and 338 Gt/y, making the average CO_2 cycle positive with an absorption of 17 Gt/y. However, considering in this delicate balance the anthropogenic emissions changes completely the equation outcome. Since the industrial revolution (XVIIIth century) our CO_2 emissions increased due to energy and food production, industries, cement,

and wastes, until reaching the current 37.8 Gt/y, causing a 50% increase of CO_2 atmospheric concentration (from 280 to 421 ppm).[4,5]

Until nowadays we considered CO_2 as a waste and atmosphere was used as dump with unlimited space. Nevertheless, as in the last century we learned to recycle wastes such as glass, plastic and paper to prevent landfill saturation and primary sources depletion, it is now time to consider CO_2 recycling as a serious option to reduce its atmospheric concentration and avoid draining our non-renewable sources (e.g. fossil fuels and coals).[6–8]

In the panorama of CO_2 emissions reduction strategies, Carbon Capture Storage (CCS) and Utilisation (CCU) technologies are potential short and long-term solutions.[4,7–12] A synergic development of these two strategies implies the collaboration between researchers and industrial partners from different field i.e., from capture and reaction plant design to chemical research or market perspective economic analysis. This synergy is the heart of the COZMOS project where I was actively involved during my PhD thesis.♣ The project started on May 2019 and will last until 2023. It unifies the efforts from several universities and research centres e.g., University of Turin, University of Oslo (UiO), CNRS Lyon, KAUST, ICC and University of Sheffield and companies e.g., SINTEF, TOPSOE, Linde, Tata-steel and Tüpras (see link for more detailed information♣) aiming to directly convert CO_2 to C_3 fuels and chemical building blocks.

As it will be described withing the thesis, I was actively involved in the project for the catalyst's structural characterization.

♣ https://www.aspire2050.eu/cozmos

1.2 CO_2 as a C1 raw source

Life Cycle Analysis of our industrial activities showed as we were, mostly involuntary, already absorbing roughly 0.23 Gt/y of CO_2 to our own profit for example for fertilizers production (57%), enhanced oil recovery (34%) and food/beverages production (9%).[4] Nevertheless, it is clear as this is not enough to balance our current emission (37.8 Gt/y).[5] Indeed, the International Energy Agency (IEA) estimated as a minimum of 3 Gt/y of CO_2 should be absorbed without any associated emissions, this being a crucial point for a CO_2 correct balance.[4] When considering any CCU or CCS technology, the amount of CO_2 that is stored/converted should imply that less CO_2 is emitted during the process, leading to a global positive balance. This concept is then the heart of new generation catalysts development, aiming to reduce CO_2 recycle reaction activation energy.[6,8,10] Depending on the final molecule targeted by CCU the required energy will vary, dividing the catalytic processes in: I) low energy and II) high energy processes, depending on the CO_2 carbon atom final oxidation state, easily identifiable by the increase of C/O ratio (1:2 in CO_2). Production of carbonates (-OCOO-), carbamates (-HN-COO-), and urea ($CO(NH_2)_2$) are then considered low energy processes whilst conversion of CO_2 to methanol (CH_3OH), methane (CH_4), formaldehyde (CH_2O), olefins (C_nH_{2n}) and saturated hydrocarbons (C_nH_{2n+2}) are high energy processes.[10,13,14]

This energetic definition also describes the chapters division of this thesis where the role of ZrO_2 and CeO_2 based catalyst for high energy and a low energy process is studied.

1.3 High energy reactions

High energy process mostly exploits CO_2 reduction with the use of H_2 to obtain CH_3OH, formaldehyde, methane, hydrocarbons, and olefines.[13,14] The possibility of obtaining high energy chemicals and fuels is opening to these reactions an impressive market. Indeed, according to the IEA the use of CO_2 to produce fuels could in principle reduced CO_2 emissions in the order >5Gt/y.[4] Nevertheless, this must imply

the use of green hydrogen♣ i.e., hydrogen produced without emitting CO_2 (from fossil fuels combining CCS or by water electrolysis using electricity from renewable sources). To obtain hydrocarbons and olefines the COZMOS project aimed to develop a tandem catalyst like the one represented in Figure 1 consisting of two components: an oxidic part aiming to hydrogenate CO_2 to methanol and an acid zeolite/zeotype for direct conversion of methanol to olefins and hydrocarbons.[12,15–18]

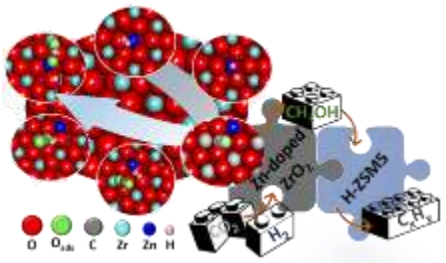

Figure 1 Pictorial representation of a tandem catalysts studied within this thesis where the oxidic catalyst (Zn-doped ZrO_2) and the acidic zeolite (H-ZSM5) are represented.

By mixing the two catalysts a cascade reaction gives access to the direct conversion of CO_2 to hydrocarbons. However, this requires compromising temperature and pressure for the equilibrium of the two reactions i.e., the former requiring low temperatures/high pressures whilst high temperatures enhance methanol dehydration and C-C coupling in the zeolite.[19] In this contest the scope of the thesis chapter dedicated to high energy reaction focuses on the structural understanding of the

♣ The original IEA document refers to low carbon hydrogen, considering then both blue hydrogen (from fossil fuels combining CCS) and green hydrogen (water electrolysis using electricity from renewable sources). The former implies a massive use of CCS and at some point, we should recycle all the stored CO_2, likely by combining it with H_2 for high energy processes. Since using blue hydrogen either implies a secondary CO_2 recycling circle or CO_2 (unsustainable) long-term storage, I have preferred to keep in the text the concept of using only green hydrogen.

oxidic catalyst component prepared and tested by several partners of the project (i.e. UiO, SINTEF, ICC, TOPSOE and KAUST). As it can be seen from the yearly published articles, 10% of the growing scientific interest for CO_2 hydrogenation is related to ZrO_2 based catalysts.

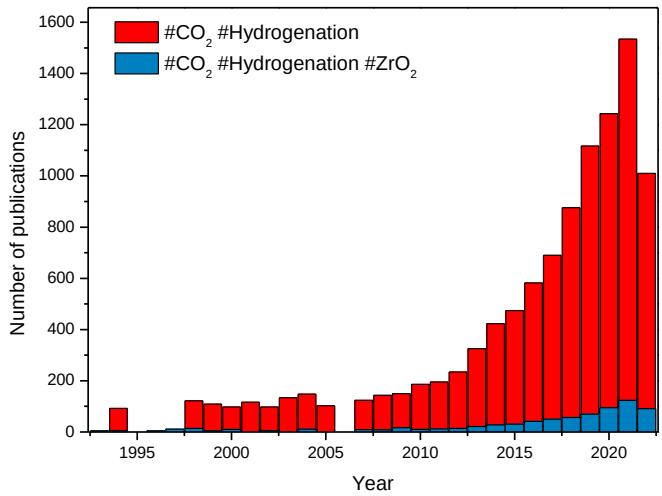

Figure 2 Yearly published articles related to CO_2 hydrogenation (red bars) and CO_2 hydrogenation ZrO_2 (blue bars). Citation Report graphic source: https://www.webofscience.com

The common denominator of these studies is about finding of the right guest atom and its concentration leading to the higher catalytic activity. Most of the studies are applying a systematic try-and-error approach screening several elements in different proportion without deeply investigating the fundamental drivers impacting the catalytic performance.[20] The high activity of aliovalent element doped ZrO_2 is attributed to the generation of stoichiometric oxygen vacancies to improve CO_2 and H_2 activation through carbonates and hydrides formation, respectively.[20] Since the chemical reactants/catalysts interactions occurs at a local level it means that they depend on the catalyst local structure. In the case of well-ordered crystals, there is no distinction between average and local structure, which is not the case when local

distortions cause deviations between local and average structure.[21] With the observation of a single-phase powder X-Ray diffractogram, doped-ZrO_2 is usually defined as a solid solution, hence implying the guest atom replacing Zr in its unit cell position. Nevertheless, diffractograms simplicity should not be automatically reflected to structure simplicity. Its Rietveld refinement in reciprocal space determines a global view of the catalyst structure however, only local probes can unveil the catalyst local structure, ultimately defining its catalytic behaviour.

Powder X-Ray Diffraction combined with Hard-X-Ray Absorption Spectroscopy (XAS) were then applied to determine the local electronic state, coordination and structure between guest atom and host matrix. Indeed, we investigated the origin of the catalytic differences between ZrO_2 doped with Ce, Zn and Ga. Even though the two catalysts presented the same crystallographic phases, measuring the XAS K-edges of all the elements (Zr, Ce, Zn and Ga) gave a complete view of the local structure in the investigated catalysts. The short-range ordering of the three catalysts presented formation of domains of different size which influenced dramatically the catalytic properties.

1.3.1 Secondary works on high energy reactions catalysts.

I would like to mention that during the thesis I worked also on other catalysts for CO_2 hydrogenation where the active site for CO_2 and H_2 activation was a metal sites grafted (PdZn alloy) over ZrO_2 and $CeZrO_x$ or included (Ni) in a CeO_2 lattice. The first catalyst was studied within the COZMOS project for direct conversion of CO_2 to propane. They were prepared and tested by UiO, CNR Lyon and KAUST whist I was actively involved in the XAS characterization of the PdZn alloy. The second catalyst ($NiCeO_x$) was instead part of an external collaboration built during the thesis with Dr. Spyros Zafeiratos from the ICPEES institute (Strasbourg, France). The catalyst was prepared and fully studied by Dr. Zafeiratos group for CO_2 conversion to methane and I had the opportunity to contribute to some NEXAFS measurements. I believe that my contribution to these topics was not intense as the efforts spent for

characterization of the oxides aforementioned. For this reason, there is not a chapter dedicated to these samples within the thesis. However, the work on these catalysts led to three publication which I reported in Appendix C, D and E for sake of clarity.

1.4 Low energy reactions

As aforementioned, in low energy reactions C/O ratio does not change hence CO_2 reactivity does not require a redox process.[13] This is the key point making these reactions market appetible and ready for the short-term implementation.[22] Indeed, all the high energy process discussed in the previous paragraph imply the massive use of green H_2, slowing down their short-term application. Contrarily, CO_2 conversion to organic carbonates by reaction with alcohol is an interesting H_2-free chemistry which could represent an immediate boost to CCU. Dimethyl carbonate (DMC) is the simplest carbonate with an increasing market as fuel additive, mild methylating agent and Li-ion batteries electrolyte.[13,23–28] Nevertheless, DMC is currently produced through the three reactions reported below, all implying toxic reagents and/or environmental unfriendly process.[23]

I) $COCl_2 + 2CH_3OH \rightarrow CH_3O(CO)OCH_3 + 2HCl$

II) $2CH_3OH + CO + ½\ O_2 \rightarrow CH_3O(CO)OCH_3 + H_2O$

III) $(CH_3O)_2SO_4 + Na_2CO_3 \rightarrow CH_3O(CO)OCH_3 + Na_2SO_4$

However, CO_2 can be used for direct production of DMC through the reaction with two molecules of methanol reported below.

IV) $CO_2 + 2CH_3OH \rightarrow CH_3O(CO)OCH_3 + H_2O$

Even though $300kt_{CO2}/y$ would be avoided with CO_2-based DMC, currently the reaction has a low efficiency, limiting its real-scale application.[29] Many homogenous catalysts have been proposed however, the separation simplicity, low cost, and negligible toxicity of (heterogenous) metal oxide catalysts make then optimal prototype systems for industrially-relevant applications.[25] However, the reaction yield is rarely higher than 10% (in absence of a sacrificial dehydrating agent), due to the high amount of water, causing catalysts deactivation. The conversion should increase at least to 20% to perform environmentally better than the conventional processes.[30] It is then of outmost importance to understand the catalyst reaction

mechanism for a rational design of new generation catalysts. The first investigated catalysts were ZrO_2 and CeO_2 with almost 100% selectivity but conversion lower than 5%. Even though the first reaction mechanism was proposed by Bell and coworkers[31] for ZrO_2, most of the recent research (Figure 3) is devoted to CeO_2, particularly to the role of oxygen vacancies towards CO_2 activation.

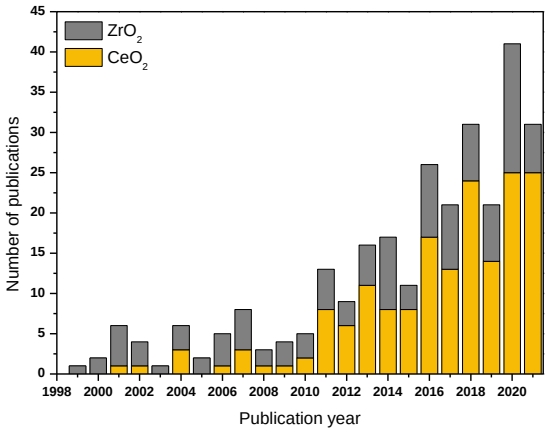

Figure 3 Publications/year distribution related to DMC production from CO_2 and CH_3OH over CeO_2 and ZrO_2 catalysts. Citation Report graphic source: https://www.webofscience.com/ (accessed Apr 28, 2022).

ZrO_2. Through a careful discussion of the surface chemistry of CO_2 and methanol dosed from gas phase, Bell and coworkers proposed a reaction mechanism involving the reaction of a methoxide species with CO_2 bent over a Zr-O Lewis Pair to form monomethylcarbonate (MMC) as reaction intermediate.[32] The last methylation occurs then through an electron donor-acceptor behaviour between methanol and Zr-O Lewis sites. Even though this mechanism followed a very precise analysis of the methoxide and carboxylates IR bands evolution, the complex band evolution might have hidden spectral components heavily overlapped with carbonates and MMC main vibrations. Moreover, working in a condensed phase does not completely reproduce DMC synthesis over oxides since it is usually carried out in liquid phase.[25]

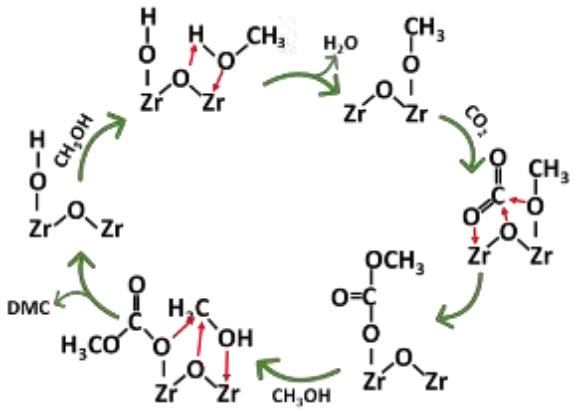

Figure 4 Proposed reaction mechanism of CO_2 and CH_3OH conversion over ZrO_2 catalyst.[31]

Aiming to characterize the surface species involved in the CO_2-to-DMC conversion reaction under realistic conditions we have studied the reaction over ZrO_2 in liquid phase by ATR-IR spectroscopy at temperatures ranging from 10 to 70°C. For a complete understanding of the band kinetic evolution the collected datasets were analysed with MCR-ALS.[33–35] Lastly the same spectra analysis approach was applied to the gas phase reaction repeating the experiment reported by Bell and coworkers,[31] unveiling the presence of spectral components previously not deconvolved.

CeO_2. CeO_2 and its solid solutions with Zr are the oxidic catalysts of major interest for DMC production (Figure 3). Particular attention has been recently dedicated to the role of oxygen vacancies (V_O) which have been proposed to contribute to the CO_2 activation through formation of a bidentate carbonate.[36] Indeed, the presence of the V_O increases charge delocalization over Ce^{4+}/Zr^{4+} improving the interaction with CO_2. Particularly, Liu and co-workers showed as in $CeZrO_x$ catalyst Ce^{3+} has an active role for CO_2 activation.[36]

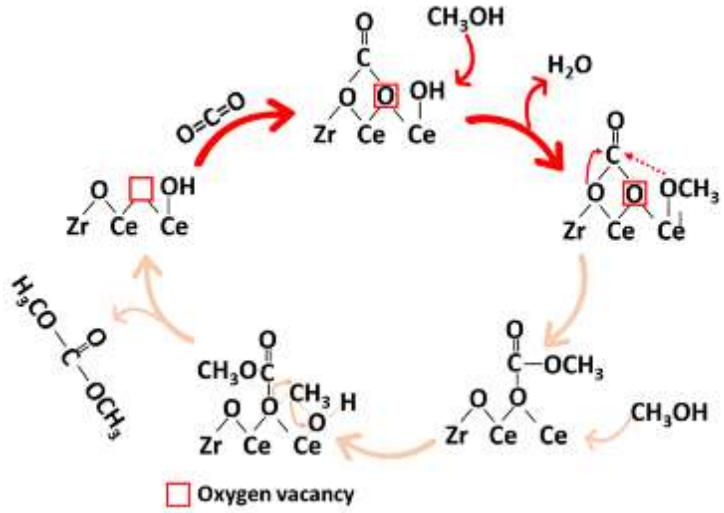

Figure 5 Reaction mechanism of CO_2 and CH_3OH conversion over $CeZrO_2$ catalyst. Darker arrows indicate the new mechanism part involving V_O whilst lighter arrows indicate the mechanism part unchanged respect to the first mechanism proposed by Bell et al.[31]

Their proposed mechanism (Figure 5) implies CO_2/Ce^{3+} redox interaction for a non-redox reaction which is however, not clearly discussed within their manuscript.[36] Moreover, the mechanism was proposed after an operando-FTIR experiment where carbonates bands were superficially assigned without considering the most recent demonstration of all the possible different carbonates vibrating at similar frequencies.[37] Furthermore, it was not considered as Aresta and co-workers reported CeO_2 catalyst deactivation caused by Ce^{3+} formation.[38,39] It is then evident as the proposed mechanism cannot completely describe the CO_2-to-DMC conversion over Ce^{3+}-rich catalyst. To remove the variable related to working with a solid solution i.e., clustering (see Chapter 3 results and discussion) or acidity/basicity differences induced by the guest atom, we have studied CO_2 and CH_3OH adsorption over 4 pure CeO_2 samples with different degree of defectivity and Ce^{3+} content by FT-IR, UV-Vis and XPS. Carbonates assignment was done after a careful analysis of $^{12}CO_2/^{13}CO_2$ IR band shifts whilst Ce^{3+}/CO_2 interaction was studied by Ce(3d) and

O(1s) XPS and UV-Vis spectra. It is noteworthy as the sample with lower Ce^{3+} concentration was not active towards MMC formation (evaluated by FT-IR bands formation) whilst the one with the highest Ce^{3+} content (≈35%) led to formation of Frustrated Lewis Pair (described below) giving access to a more complex and complete reaction mechanism.

Frustrated Lewis Pair (FLP). A FLP, reported in Figure 6 for clarity, consists of a Lewis acid (LA) and a Lewis base (LB) with bulky ligands that prevent these species from neutralizing each other.[40–42]

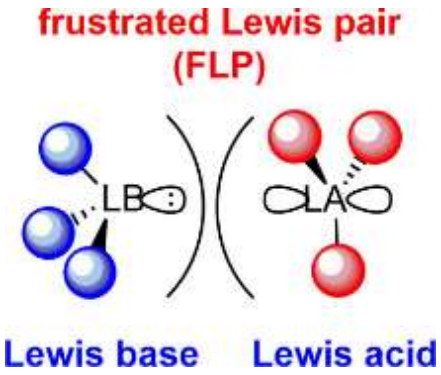

Figure 6 Pictorial representation of a Frustrated Lewis Pair reproduced from Stephan manuscript.[42]

Historically discovered in 1923 and firstly named in 2010,[43] FLP were firstly limited to homogeneous catalysis but extended recently to heterogeneous catalysis.[40,41,44–46] In particular, CeO_2 has been shown to form FLPs between two adjacent Ce^{3+} (LA) and an O_2- (LB) separated by an oxygen vacancy at a distance of ~4Å.[47,48] This particular condition was shown to occur only when surface Ce^{3+} concentration (>30%) ensured clustering of Ce^{3+}-V_O-Ce^{3+} over CeO_2 (101) planes.[49] CeO_2 FLPs improved reactivity of alkenes and alkynes, syngas and recently CO_2 .[47,48,50–52] In the latter case CO_2 activation over heterogeneous catalysts proceed via acid-base interaction with catalyst surface inducing bending of CO_2 double bond and making the C atom more electrophilic.[53] Considering CeO_2 FLPs, Zhang et al. predicted CO_2

activation through the formation of a bidentate carbonate ascribing to its formation the improved CO_2 conversion towards olefins and cyclic carbonates.[52] Nevertheless, the mechanism on how the FLP site activates CO_2 remains unclear. Indeed, FLP presence and activity is very difficult to be observed since it mainly consists of missing oxygens on a catalysts surface well known for its oxygen storage and mobility properties.[54] For this reason, associating improved CO_2 conversion at high temperature over Ce^{3+}-rich CeO_2 to FLP is not straightforward. The MMC formation if then a perfect a case study to disclose details on CO_2/FLP since it implies CO_2 whole incorporation in a new molecule ($CH_3O(CO_2)$-) at a moderate temperature (≈150°C) which prevents CeO_2 oxygen mobility i.e., reducing surface-to-bulk FLP mobility.

References

(1) Rockström, J.; W. Steffen; K. Noone; Å. Persson; F. S. Chapin; E. F. Lambin; T. M. Lenton; M. Scheffer; C. Folke; H. J. Schellnhuber; B. Nykvist; C. A. de Wit; T. Hughes; S. van der Leeuw; H. Rodhe; S. Sörlin; P. K. Snyder; R. Costanza; U. Svedin; M. Falkenmark; L. Karlberg; R. W. Corell; V. J. Fabry; J. Hansen; B. Walker; D. Liverman; K. Richardson; P. Crutzen; J. A. Foley. A Safe Operation Space for Humanity. *Nature* **2009**, *461* (September), 472–475.

(2) Cassia, R.; Nocioni, M.; Correa-Aragunde, N.; Lamattina, L. Climate Change and the Impact of Greenhouse Gasses: CO2 and NO, Friends and Foes of Plant Oxidative Stress. *Front. Plant Sci.* **2018**, *9* (March), 1–11. https://doi.org/10.3389/fpls.2018.00273.

(3) IPCC. Climate Change 2001. Synthesis Report. IPCC Third Assessment Report (TAR). *Ipcc* **2001**, 409.

(4) Putting CO 2 to Use. **2019**, No. September.

(5) Crippa, M.; Oreggioni, G.; Guizzardi, D.; Muntean, M.; Schaaf, E.; Lo Vullo, E.; Solazzo, E.; Monforti-Ferrario, F.; Olivier, J. G. .; Vignati, E. *Fossil CO2 and GHG Emissions of All World Countries - 2019 Report Publications Office of the EU*; 2019. https://doi.org/10.2760/687800.

(6) Aresta, M. *Carbon Dioxide as a Chemical Feedstock*; Prof. Dr. Michele Aresta, Ed.; Wiley-VCH Verlag GmbH & Co. KGaA.

(7) Royal Society. The Potential and Limitations of Using Carbon Dioxide. **2017**, 1–11.

(8) Aresta, M.; Dibenedetto, A.; Angelini, A. Catalysis for the Valorization of Exhaust Carbon : From CO2 to Chemicals, Materials, and Fuels.

Technological Use of CO2. *Chem. Rev.* **2014**, 1–18. https://doi.org/10.1002/9781119951438.eibc2257.

(9) Co, U. *Carbon Capture and Utilisation in the Green Economy*.

(10) Aresta, M.; Dibenedetto, A.; Angelini, A. The Changing Paradigm in CO_2 Utilization. *J. CO2 Util.* **2013**, *3–4*, 65–73. https://doi.org/10.1016/j.jcou.2013.08.001.

(11) Tabanelli, T.; Bonincontro, D.; Albonetti, S.; Cavani, F. *Conversion of CO 2 to Valuable Chemicals : Organic Carbonate as Green Candidates for the Replacement of Noxious Reactants*, 1st ed.; Elsevier B.V., 2019; Vol. 178. https://doi.org/10.1016/B978-0-444-64127-4.00007-0.

(12) Zhou, W.; Cheng, K.; Kang, J.; Zhou, C.; Subramanian, V.; Zhang, Q.; Wang, Y. New Horizon in C1 Chemistry: Breaking the Selectivity Limitation in Transformation of Syngas and Hydrogenation of CO_2 into Hydrocarbon Chemicals and Fuels. *Chem. Soc. Rev.* **2019**, *48* (12), 3193–3228. https://doi.org/10.1039/C8CS00502H.

(13) Sakakura, T.; Choi, J. C.; Yasuda, H. Transformation of Carbon Dioxide. *Chem. Rev.* **2007**, *107* (6), 2365–2387. https://doi.org/10.1021/cr068357u.

(14) Saeidi, S.; Amin, N. A. S.; Rahimpour, M. R. Hydrogenation of CO2 to Value-Added Products - A Review and Potential Future Developments. *J. CO2 Util.* **2014**, *5*, 66–81. https://doi.org/10.1016/j.jcou.2013.12.005.

(15) Wang, S.; Zhang, L.; Zhang, W.; Wang, P.; Qin, Z.; Yan, W.; Dong, M.; Li, J.; Wang, J.; He, L.; Olsbye, U.; Fan, W. Selective Conversion of CO_2 into Propene and Butene. *Chem* **2020**, *6* (12), 3344–3363. https://doi.org/10.1016/j.chempr.2020.09.025.

(16) Liu, X.; Zhou, W.; Yang, Y.; Cheng, K.; Kang, J.; Zhang, L.; Zhang, G.; Min,

X.; Zhang, Q.; Wang, Y. Design of Efficient Bifunctional Catalysts for Direct Conversion of Syngas into Lower Olefins: Via Methanol/Dimethyl Ether Intermediates. *Chem. Sci.* **2018**, *9* (20), 4708–4718. https://doi.org/10.1039/c8sc01597j.

(17) Cheng, K.; Gu, B.; Liu, X.; Kang, J.; Zhang, Q.; Wang, Y. Direct and Highly Selective Conversion of Synthesis Gas into Lower Olefins : Design of a Bifunctional Catalyst Combining Methanol Synthesis and Carbon – Carbon Coupling. **2016**, 4725–4728. https://doi.org/10.1002/anie.201601208.

(18) Cheng, K.; Zhou, W.; Kang, J.; He, S.; Shi, S.; Zhang, Q.; Pan, Y.; Wen, W.; Wang, Y. Bifunctional Catalysts for One-Step Conversion of Syngas into Aromatics with Excellent Selectivity and Stability. *Chem* **2017**, *3* (2), 334–347. https://doi.org/10.1016/j.chempr.2017.05.007.

(19) Thomas, W. J.; Portalski, S. . Thermodynamic in Methanol Synthesis. *Ind. Eng. Chem. Res.* **1958**, *50* (June), 967–970.

(20) Dang, S.; Gao, P.; Liu, Z.; Chen, X.; Yang, C.; Wang, H.; Zhong, L.; Li, S.; Sun, Y. Role of Zirconium in Direct CO2 Hydrogenation to Lower Olefins on Oxide/Zeolite Bifunctional Catalysts. *J. Catal.* **2018**, *364*, 382–393. https://doi.org/10.1016/j.jcat.2018.06.010.

(21) Takeshi, E.; Billinge, S. J. L. *Underneath the Bragg Peaks: Structural Analysis of Complex Materials*; 2012; Vol. 16.

(22) Chauvy, R.; Meunier, N.; Thomas, D.; De Weireld, G. Selecting Emerging CO2 Utilization Products for Short- to Mid-Term Deployment. *Appl. Energy* **2019**, *236* (December 2018), 662–680. https://doi.org/10.1016/j.apenergy.2018.11.096.

(23) Delledonne, D.; Rivetti, F.; Romano, U. Developments in the Production and Application of Dimethylcarbonate. **2001**, *221*, 241–251.

(24) Aricò, F.; Tundo, P. Dimethyl Carbonate as a Modern Green Reagent and Solvent. *Russ. Chem. Rev.* **2010**, *79* (6), 479–489. https://doi.org/10.1070/rc2010v079n06abeh004113.

(25) Keller, N.; Rebmann, G.; Keller, V. Catalysts , Mechanisms and Industrial Processes for the Dimethylcarbonate Synthesis. **2010**, *317*, 1–18. https://doi.org/10.1016/j.molcata.2009.10.027.

(26) Tamboli, A. H.; Chaugule, A. A.; Kim, H. Catalytic Developments in the Direct Dimethyl Carbonate Synthesis from Carbon Dioxide and Methanol. *Chem. Eng. J.* **2017**, *323*, 530–544. https://doi.org/10.1016/j.cej.2017.04.112.

(27) Assabumrungrat, S. Techno-Economic Evaluation of Different CO 2 -Based Processes for Dimethyl Carbonate Production. *Chem. Eng. Res. Des.* **2014**, 1–15. https://doi.org/10.1016/j.cherd.2014.07.013.

(28) Azapagic, A.; Cue, R. M. Carbon Capture , Storage and Utilisation Technologies : A Critical Analysis and Comparison of Their Life Cycle Environmental Impacts. **2015**, *9*, 82–102. https://doi.org/10.1016/j.jcou.2014.12.001.

(29) Otto, A.; Grube, T.; Schiebahn, S.; Stolten, D. Closing the Loop: Captured CO2 as a Feedstock in the Chemical Industry. *Energy Environ. Sci.* **2015**, *8* (11), 3283–3297. https://doi.org/10.1039/c5ee02591e.

(30) Garcia-Herrero, I.; Cuéllar-Franca, R. M.; Enríquez-Gutiérrez, V. M.; Alvarez-Guerra, M.; Irabien, A.; Azapagic, A. Environmental Assessment of Dimethyl Carbonate Production: Comparison of a Novel Electrosynthesis Route Utilizing CO2 with a Commercial Oxidative Carbonylation Process. *ACS Sustain. Chem. Eng.* **2016**, *4* (4), 2088–2097. https://doi.org/10.1021/acssuschemeng.5b01515.

(31) Jung, K. T.; Bell, A. T. An *in Situ* Infrared Study of Dimethyl Carbonate

Synthesis from Carbon Dioxide and Methanol over Zirconia. *J. Catal.* **2001**, *347*, 339–347. https://doi.org/10.1006/jcat.2001.3411.

(32) Zhao, S. Y.; Wang, S. P.; Zhao, Y. J.; Ma, X. Bin. An *in Situ* Infrared Study of Dimethyl Carbonate Synthesis from Carbon Dioxide and Methanol over Well-Shaped CeO2. *Chinese Chem. Lett.* **2017**, *28* (1), 65–69. https://doi.org/10.1016/j.cclet.2016.06.003.

(33) Jaumot, J.; Gargallo, R.; De Juan, A.; Tauler, R. A Graphical User-Friendly Interface for MCR-ALS: A New Tool for Multivariate Curve Resolution in MATLAB. *Chemom. Intell. Lab. Syst.* **2005**, *76* (1), 101–110. https://doi.org/10.1016/j.chemolab.2004.12.007.

(34) Ruckebusch, C.; Blanchet, L. Multivariate Curve Resolution: A Review of Advanced and Tailored Applications and Challenges. *Anal. Chim. Acta* **2013**, *765*, 28–36. https://doi.org/10.1016/j.aca.2012.12.028.

(35) Alcaráz, M. R.; Schwaighofer, A.; Goicoechea, H.; Lendl, B. Application of MCR-ALS to Reveal Intermediate Conformations in the Thermally Induced α-β Transition of Poly-L-Lysine Monitored by FT-IR Spectroscopy. *Spectrochim. Acta - Part A Mol. Biomol. Spectrosc.* **2017**, *185* (May 2017), 304–309. https://doi.org/10.1016/j.saa.2017.05.005.

(36) Liu, B.; Li, C.; Zhang, G.; Yao, X.; Chuang, S. S. C.; Li, Z. Oxygen Vacancy Promoting Dimethyl Carbonate Synthesis from CO2 and Methanol over Zr-Doped CeO2 Nanorods. *ACS Catal.* **2018**, *8* (11), 10446–10456. https://doi.org/10.1021/acscatal.8b00415.

(37) Vayssilov, G. N.; Mihaylov, M.; Petkov, P. S.; Hadjiivanov, K. I.; Neyman, K. M. Reassignment of the Vibrational Spectra of Carbonates , Formates , and Related Surface Species on Ceria : A Combined Density Functional and Infrared Spectroscopy Investigation. *J. Phys. Chem. C* **2011**, *115* (47), 23435–

23454.

(38) Aresta, M.; Dibenedetto, A.; Pastore, C.; Cuocci, C.; Aresta, B.; Cometa, S.; De Giglio, E. Cerium(IV)Oxide Modification by Inclusion of a Hetero-Atom: A Strategy for Producing Efficient and Robust Nano-Catalysts for Methanol Carboxylation. *Catal. Today* **2008**, *137* (1), 125–131. https://doi.org/10.1016/j.cattod.2008.04.043.

(39) Aresta, M.; Dibenedetto, A.; Pastore, C.; Angelini, A.; Aresta, B.; Pápai, I. Influence of Al2O3 on the Performance of CeO2 Used as Catalyst in the Direct Carboxylation of Methanol to Dimethylcarbonate and the Elucidation of the Reaction Mechanism. *J. Catal.* **2010**, *269* (1), 44–52. https://doi.org/10.1016/j.jcat.2009.10.014.

(40) Stephan, D. W. Frustrated Lewis Pairs: From Concept to Catalysis. *Acc. Chem. Res.* **2015**, *48* (2), 306–316. https://doi.org/10.1021/ar500375j.

(41) Stephan, D. W.; Erker, G. Frustrated Lewis Pairs: Metal-Free Hydrogen Activation and More. *Angew. Chemie - Int. Ed.* **2010**, *49* (1), 46–76. https://doi.org/10.1002/anie.200903708.

(42) Stephan, D. W. Frustrated Lewis Pairs. *J. Am. Chem. Soc.* **2015**, *137* (32), 10018–10032. https://doi.org/10.1021/jacs.5b06794.

(43) McCahill, J. S. J.; Welch, G. C.; Stephan, D. W. Reactivity of "Frustrated Lewis Pairs": Three-Component Reactions of Phosphines, a Borane, and Olefins. *Angew. Chemie* **2007**, *119* (26), 5056–5059. https://doi.org/10.1002/ange.200701215.

(44) Stephan, D. W.; Erker, G. Frustrated Lewis Pair Chemistry: Development and Perspectives. *Angew. Chemie - Int. Ed.* **2015**, *54* (22), 6400–6441. https://doi.org/10.1002/anie.201409800.

(45) Pérez, M.; Mahdi, T.; Hounjet, L. J.; Stephan, D. W. Electrophilic Phosphonium Cations Catalyze Hydroarylation and Hydrothiolation of Olefins. *Chem. Commun.* **2015**, *51* (56), 11301–11304. https://doi.org/10.1039/c5cc03572d.

(46) Stephan, D. W. The Broadening Reach of Frustrated Lewis Pair Chemistry. *Science (80-.).* **2016**, *354* (6317). https://doi.org/10.1126/science.aaf7229.

(47) Zhang, S.; Huang, Z. Q.; Ma, Y.; Gao, W.; Li, J.; Cao, F.; Li, L.; Chang, C. R.; Qu, Y. Solid Frustrated-Lewis-Pair Catalysts Constructed by Regulations on Surface Defects of Porous Nanorods of CeO2. *Nat. Commun.* **2017**, *8* (May), 1–11. https://doi.org/10.1038/ncomms15266.

(48) Huang, Z. Q.; Liu, L. P.; Qi, S.; Zhang, S.; Qu, Y.; Chang, C. R. Understanding All-Solid Frustrated-Lewis-Pair Sites on CeO2 from Theoretical Perspectives. *ACS Catal.* **2018**, *8* (1), 546–554. https://doi.org/10.1021/acscatal.7b02732.

(49) Nolan, M.; Parker, S. C.; Watson, G. W. The Electronic Structure of Oxygen Vacancy Defects at the Low Index Surfaces of Ceria. *Surf. Sci.* **2005**, *595* (1–3), 223–232. https://doi.org/10.1016/j.susc.2005.08.015.

(50) Huang, Z. Q.; Li, T. H.; Yang, B.; Chang, C. R. Role of Surface Frustrated Lewis Pairs on Reduced CeO2(110) in Direct Conversion of Syngas. *Chinese J. Catal.* **2020**, *41* (12), 1906–1915. https://doi.org/10.1016/S1872-2067(20)63627-0.

(51) Lim, C. H.; Holder, A. M.; Hynes, J. T.; Musgrave, C. B. Roles of the Lewis Acid and Base in the Chemical Reduction of CO 2 Catalyzed by Frustrated Lewis Pairs. *Inorg. Chem.* **2013**, *52* (17), 10062–10066. https://doi.org/10.1021/ic4013729.

(52) Zhang, S.; Xia, Z.; Zou, Y.; Cao, F.; Liu, Y.; Ma, Y.; Qu, Y. Interfacial

Frustrated Lewis Pairs of CeO2 Activate CO2 for Selective Tandem Transformation of Olefins and CO2 into Cyclic Carbonates. *J. Am. Chem. Soc.* **2019**, *141* (29), 11353–11357. https://doi.org/10.1021/jacs.9b03217.

(53) Borges, M.; Ø, J. J. Ø. C.; Olcina, J. G.; Hu, L.; Cornu, D.; Huang, R.; Stoian, D.; Urakawa, A. CO2 Activation over Catalytic Surfaces. *ChemPhysChem* **2017**, *18*, 3135–3141. https://doi.org/10.1002/cphc.201700782.

(54) Montini, T.; Melchionna, M.; Monai, M.; Fornasiero, P. Fundamentals and Catalytic Applications of CeO2-Based Materials. *Chem. Rev.* **2016**, *116* (10), 5987–6041. https://doi.org/10.1021/acs.chemrev.5b00603.

2 Materials and methods

2.1 Materials

All the samples described in Chapter 3 were characterized as received from one of the COZMOS partner. Most of the reported data were measured from one of the partners as well. When catalytic results were not available, literature data are reported for sake of comparison.

Zn-doped ZrO_2 samples described in Chapter 3 have been characterized as received from the University of Oslo (Norway). Briefly, catalysts were prepared by coprecipitation of $Zn(NO_3)_2$ and ZrN_2O_7 salts as described elsewhere.[1] Catalysts will be referred to as ZnZr(X) where "X" indicates Zn wt% evaluated by either ICP or EDX analysis. Pure ZrO_2 related to these samples was prepared with the same synthesis strategy without Zn salts.

Ga-doped ZrO_2 was prepared at the ICC Institute following the published receipt.[2] Ga content was evaluated by EDX analysis.

$ZnCeZrO_x$ catalyst described in Chapter 3.7 was prepared by ICC following the published receipt.[3] Zn and Ce contents were determined by ICP analysis.

Zeolites/Zeotypes. Even though the core of the studies withing this thesis were the employed oxides materials, few details on the reported zeolites and zeotypes employed for the reported catalytic test should be reported. **H-ZSM5 and SAPO-34** were commercial catalysts purchased by Zeolyts and ACS materials, respectively. Their characterization is fully described in the published manuscript reported in Appendix A.[1] **H-SSZ-13** was prepared by ICC following a receipt which is currently under publication. **H-RUB-13** was prepared by ICC partner as described in the respective published manuscript.[3]

ZrO_2 described in Chapter 4 was prepared by sol-gel synthesis according to the literature.[4]

CeO_2 catalysts reported in Chapter 4 were prepared by microwave (MW)-assisted sol-gel synthesis adapted from a conventional protocol.[5] As shown in Figure 7, microwaves were chosen as a heat source since they allow to rapidly obtain a homogenous temperature in the reactor cell, implying fast and reproducible synthesis with the formation of small crystallites due to high nucleation/low growth rates.

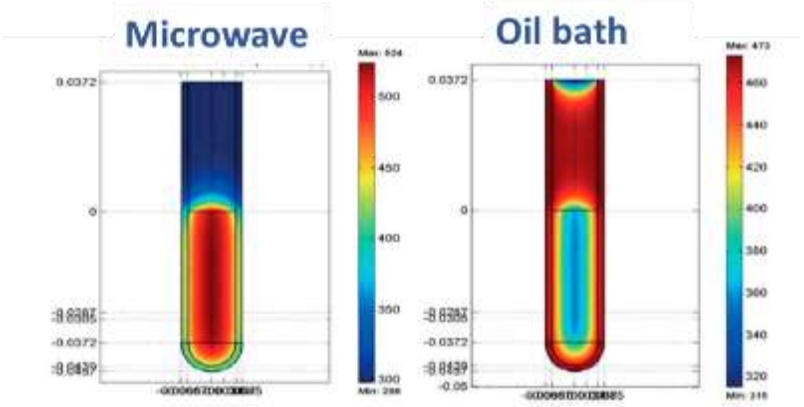

Figure 7 Thermal profile of a glass vial heated in a conventional oil bath and in a microwave reactor. The figure is reproduced from Zhu et al.[6]

The obtained CeO_2 powder was then divided into two batches, **MW(100)** and **MW(650)**, which were calcined under air for 8 h at 100 °C and 650 °C, respectively. Reference material was also prepared by conventional sol-gel synthesis and calcined at 650°C for 8h (**conv(650)**). [5]

2.2 Methods

2.2.1 Specific surface area.

Since the work of the thesis is dedicated to the catalysts characterization rather than the improvement of a synthesis strategy, the specific surface area (SSA) is used as valuable information to verify if a series of samples presented a comparable surface area hence excluding it from influencing the catalysts different properties. The SSAs

were determined by applying the Brunauer–Emmett–Teller (BET) method to the adsorption/desorption isotherms of N_2 at 77K obtained with a Micromeritics ASAP 2020 physisorption analyzer.[7]

2.2.2 Powder X-Ray Diffraction

Powder X-Ray diffraction (PXRD) patterns were collected to investigate the average structural properties of the catalysts i.e., phase composition and lattice parameters. In-situ PXRD measurements were particularly useful to follow the unit cell volume variation during thermal treatments.

The Laboratory PXRD patterns were collected at room temperature (RT) with a PW3050/60 X'Pert PRO MPD diffractometer (PANalytical) in the Bragg–Brentano geometry using either a flat glass sample holder or a spinning zero-noise Si holder. Patterns from the Cu $K\alpha_{1,2}$ X-ray source were recorded from 10 to 90° 2θ with a step size of 0.0167° and an integration time of 40 s. The Rietveld refinement method implemented in the FullProf software package[8] was used to extract phase abundances, lattice parameters and peak shapes following the procedure described in the manuscript reported in appendix.[1]

Ex situ Synchrotron PXRD patterns were recorded in transmission mode at BM31 beamline (ESRF) in Debye-Scherrer configuration employing monochromatic radiation (λ~0.270Å). Debye-Scherrer cones were collected from a CCD camera and were further integrated to obtain the reported line graphs. Samples were contained in a quartz capillary (Ø=0.5 mm). In-situ PXRD patterns were measured in the same capillary by flowing a 50 mL/min H_2:He flow (1:2) whilst heat was provided by a heat blower.

Unit cell volume variation with temperature was extracted from the in-situ PXRD pattern by using FullProf implemented sequential mode.

2.2.3 Fourier Transform Infrared spectroscopy (FTIR)

FTIR is an important technique to study catalyst surfaces adsorption properties. Indeed, the vibrational spectra of adsorbed molecules such as CO, CO_2, and CH_3OH gave important information on the catalysts' defectivity, oxidation state, and reactivity. In the case of ***ex situ*** **experiments** the sample was pressed to form a self-standing pellet of ≈10 cm^2 placed in a gold envelope. The envelope was then placed in a home-made cell equipped with KBr windows and suitable for thermal treatments under high vacuum (5E-04mbar) or gas environment (O_2/H_2). After the activation process (see below) the cell was mounted on the FT-IR instrument where a dedicated glass line allowed the dosing of controlled pressures/volume of specific molecules.

Ce^{3+}. FTIR spectra of the sample as prepared or as activated (see activation procedure hereafter) are already very informative. Indeed, as it will be discussed within Chapter 4, the presence of Ce^{3+} can be already qualitatively determined from the presence of a band at 2127 cm^{-1} in the sample spectra prior to the adsorption of any molecule. Indeed, this band is related to the $^2F_{5/2} \rightarrow {}^2F_{7/2}$ electronic adsorption which is present only in Ce^{3+}($[Xe]4f^15d^06s^0$) and absent in Ce^{4+} ($[Xe]4f^05d^06s^0$).[9,10]

CO. Carbon monoxide is employed since decades as simple accessible probe molecule to investigate the chemical nature of surface sites.[11,12] Once CO interacts with metal/ions sites on the catalyst surface, depending on the cation ionic potential, the predominant charge withdrawing direction can be divided into CO-to-cation or cation-to-CO, defining the interaction as σ-donation or π-backdonation, respectively. The former depletes charge density from CO slightly antibonding level, increasing its bond strength and causing a hypsochromic shift from the ideal CO stretching vibration (2143 cm^{-1}), whilst the latter fills CO strongly antibonding levels, weakening the triple bond and inducing a bathochromic shift. Typically, for cationic sites σ-donation prevails, for metallic sites π-backdonation prevails, thus causing bathochromic and hypsochromic, respectively, of the stretching vibration of adsorbed CO. As a consequence, CO adsorption allows to determine whether: a)

strong and weak Lewis acid sites (Ce^{4+} and Zr^{4+}),[13,14] are still present over the catalyst surface after grafting and reduction treatments (bands shifted to lower wavenumbers) and b) if Ce^{3+} is present on the surface from a typical band shifted around 2130 cm^{-1}.

CO adsorption experiments were carried out with an ad-hoc cell equipped with KBr windows allowing to cool the pellet temperature down to liquid nitrogen temperature (nominal 100K).

The adsorption of **CO_2** and **CH_3OH** is discussed within the text.

Activation. Before IR measurements, catalysts generally underwent an activation meant to clean the surface and to leave an oxidised/reduced state. In both cases, the followed protocol consisted on: i) outgassing and heating the catalyst at 5°C/min from RT to 150°C under vacuum, ii) heating from 150°C to 400°C (5°C/min) under static 100 mbar O_2 for CeO_2 (to prevent CeO_2 self-reduction) and under vacuum (5E-04 mbar) for ZrO_2 , iii) holding at 400°C for 30' under O_2 atmosphere, iv) cooling under O_2 until 150°C and then evacuating. In the case of reduced CeO_2 (MW(100)-red) the sample was kept at 150°C under H_2 for 30' then cooled to RT under vacuum (5E-04 mbar).

Operando IR experiments. Operando IR experiments were performed using FTIR in the case of gas-phase experiments and in ATR-IR mode for liquid-phase experiments. ATR-IR set-up description can be found in the submitted manuscript reported in the Appendix F. Gas phase experiments were conducted to study CO_2/CH_3OH alone and coupled adsorption/desorption kinetics on ZrO_2 surface. ZrO_2 sample was pressed into a self-standing pellet of ~10 mg mass and ~100 mm^2 area which was placed into a commercial water-cooled cell heatable stainless steel cell (Aabspec) suitable for thermal treatments (RT-400°C) under gas flow mounted in a Bruker Invenio spectrometer. Input gas flow was connected to the set-up reported in Figure 8 whilst the output stream was connected to a Mass Spectrometer.

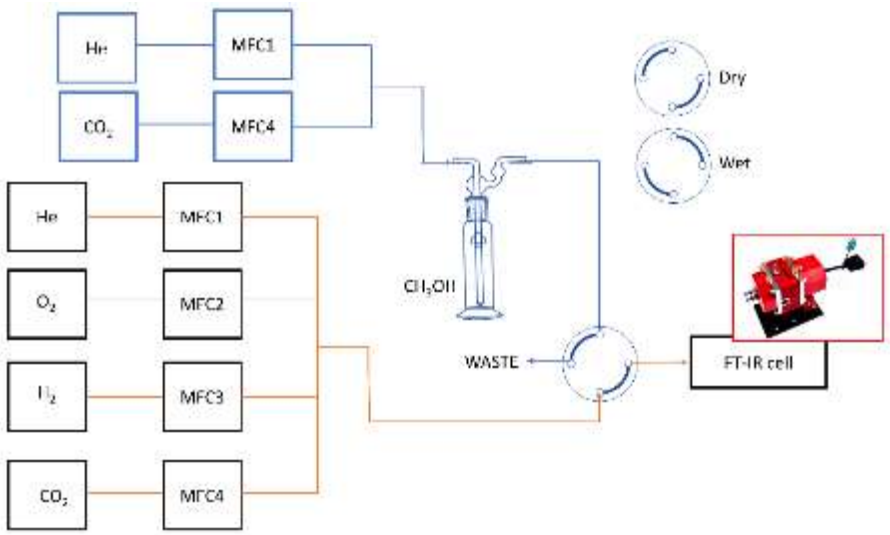

Figure 8 Scheme of the reaction set-up employed for operando IR. The employed 4-way valve is represented in both configurations allowing to send either dry or wet gases to the FT-IR cell.

A constant flow of 40 mL/min of all the employed gases was kept constant through the experiments. Prior CO_2/CH_3OH adsorption, desorption or reaction the catalyst underwent an activation procedure consistent into heating from RT to 400°C under an He:O_2 flow (50:50) and by holding the temperature at 400°C for 60'. After the activation the sample was cooled to RT or 150°C under He flow. CO_2 (99.999%) was provided through a Brookhaven mass-flowmeter whilst CH_3OH flow was obtained by flowing He through a gas-liquid bubbler filled with CH_3OH and kept at constant temperature. CH_3OH concentration in the bubbler output was calculated using the equation below.

$$F_{v,out} = F_{c,in} * \frac{P_v}{P_{head} . P_v}$$

The output vapour flow ($F_{v,out}$) is calculated in function of the incoming carrier flow ($F_{c,in}$), the liquid vapour pressure (P_v) which is temperature dependent (Figure 9) and

the bubbler head pressure (P_{head}) which is assumed to be equal to the ambient pressure.

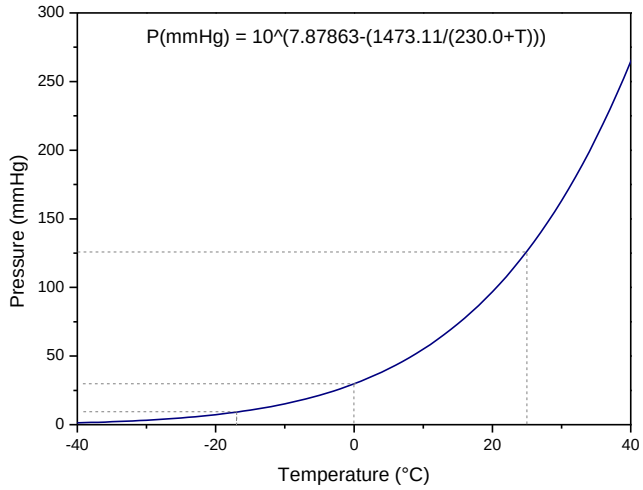

Figure 9 Graph reporting methanol vapour pressure relation with temperature. Source Langest's Handbook of Chemistry 10th ed.

2.2.4 UV-Vis Spectroscopy

UV-Vis spectra gave information on the catalyst's average electronic properties. Diffuse Reflectance UV-Vis spectra of CeO_2 samples described in CHAPTER 4.4 were collected in a Varian Cary 5000 spectrophotometer, equipped with an integrating sphere with an inner surface coated by Spectralon®(the same material used as white reference). The powders were placed in a quartz bulb cell, allowing thermal treatments. Pre-treatments and CO_2 interaction were performed in the same way as for the IR measurements. DR-UV-Vis spectra for Ga/Zn/Ce-ZrO_2 samples described in CHAPTER 3 were recorded on pellets with Avantes optic fibers.

2.2.5 X-ray Photoelectron Spectroscopy (XPS)

X-Ray Photoelectron Spectroscopy (XPS) is based on the measurement of the photoelectrons emitted after the absorption of an incoming photon. A dual anode X-Ray source (Al K_α) causes the emission of photoelectrons in the 0-1000 eV binding

energy range whilst an analyzer allows photoelectron energy discrimination, particularly in the Ce(3d) (870-980 eV), O(1s)(520-540 eV) and C(1s)(280-290 eV) energy regions. Quasi *in situ* X-Ray Photoelectron Spectroscopy (XPS) measurements were carried out at ICPEES (Strasbourg) in the laboratory of Dr. Spyros Zafeiratos. The ultrahigh vacuum (UHV) spectrometer was equipped with a variable pressure reactor allowing thermal/gas treatments of the catalyst in controlled atmosphere and consequent transfer to the XPS analysis chamber without exposing it to air. All the details concerning the measurement and the following data analysis are described in the manuscript under submission reported in the Appendix G.

Beam damage of as-prepared MW(100) (see Chapter 3) was evaluated for I) beam exposure during time and II) sample heating under vacuum. Considering dual anode beam damage (Figure 10a,b) we observed as by collecting spectra with 5min/scan (Figure 10a) the $Ce^{4+/3+}$ regions begin to vary after 30'. The first scan (5') presented Ce^{3+} abundance of 11% whilst averaging the 6 spectra in Figure 10a led to Ce^{3+}≈14%. Since there is not a considerable difference between the two spectra and fit results, we proceeded by collecting spectra with 30' time/scan for 330', observing as Ce^{3+} concentration increased to 15% after 60' of exposure while the sample temperature increased to 25°C. Eventually, Ce^{3+} concentration increased up to 25% after 330' exposure and temperature grew up to 35°C. On the contrary, catalyst damage induced by temperature under UHV (Figure 10b,c) showed a drastic increase of Ce^{3+} concentration already at 150°C, reaching values >45% at 400°C. These results showed as: I) dual anode exposure increased Ce^{3+} abundance of 4% in the first 60' and II) heating under vacuum had a stronger effect on Ce^{3+} oxidation state. Since at 50°C we observed 27% Ce^{3+} and after 330' of sample exposure to dual anode its temperature/Ce^{3+} reached 32°C/23%, we can conclude that heating from the X-Ray beam caused most of the damage from its exposure. To minimize the beam exposure effect on Ce(3d) region and following the evidence in Figure 10a, we then measured this region as the first one limiting the measurement to 30' time/scan.

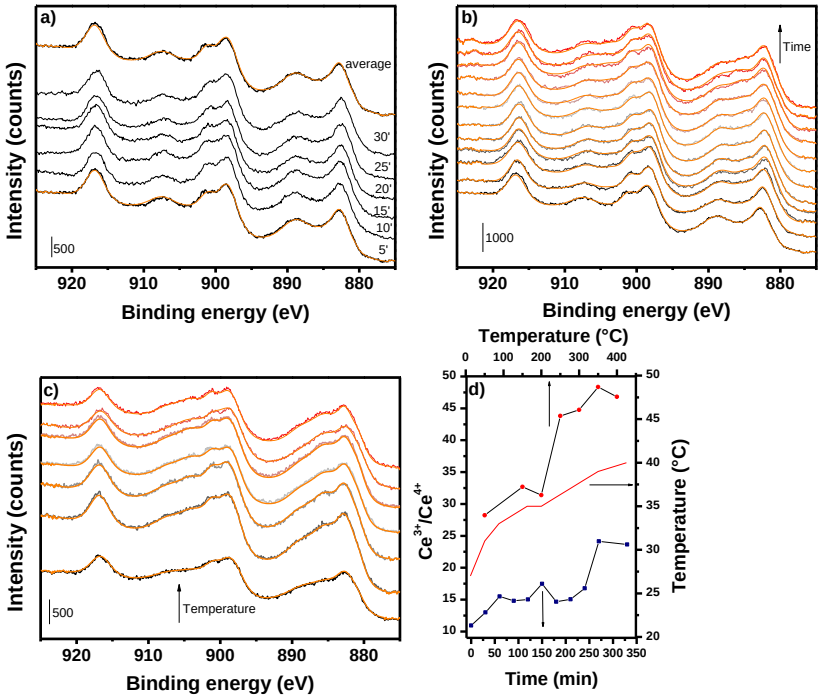

Figure 10 XPS experimental data and best fit curves (orange lines) collected : a) with 5' time/scan for 30' exposure to dual anode beam, b) with 30' time/scan for 330' exposure to dual anode beam (time increases from black to red line) and c) with 30' time/scan during heating under UHV (temperature increases from black to red line). d) Ce^{+3}/Ce^{+4}concentration evaluated by best-fit curves during the time and temperature measurements. Samples stage temperature profile evolution during time experiment is reported with red line.

2.2.6 X-Ray Absorption Fine Structure (XAFS)

XAFS is a well-known technique referring to the X-Ray absorption properties of an atom core-level. Particularly at energies lower and higher than the core-level binding energy the absorption probability is modulated by the absorber chemical and physical state. This makes XAFS an element selective technique sensitive to little concentration of the absorber. The XAFS spectrum is usually divided into two regions: I) x-ray absorption near edge (XANES) region, containing information on

the formal oxidation state and local geometry (tetrahedral, octahedral, etc.) and II) extended x-ray absorption fine structure (EXAFS) which is employed to determine structural information on the absorber environment (e.g., distances and coordination number with surrounding atoms). Multi-edge fit is a well-known approach to determine local disorder in alloys and oxides.[ref] Nevertheless, this approach is rarely employed in the catalysis community where catalysts are often claimed to be homogenous solid solutions by simple PXRD and single edge-fit, employing the determined structure to predict catalyst behaviour such as reaction mechanisms. Since the knowledge of the catalyst local structure is extremely important for these types of studies, this thesis aims to employ the multi-edge fit approach to the limit of its interpretability. However, as discussed in the thesis, often the catalyst presented such a high degree of disorder to imply the use of single edge-fit applied to all the measured sample edges. Zn, Zr and Ce K-edges were all recorded in transmission mode during several beamtimes at ESRF (BM31 and BM23 beamlines) and SOLEIL (Rock Beamline) synchrotrons, hence the experimental details are well reported in the Appendix.[1,15]

Ga K-edge spectra were recorded in fluorescence mode to discard to the contribution of Hf $L_{2,1}$-edges which were always present since Hf is a natural dopant of Zr. Spectra were energy aligned to the respective metal despite for Ce K-edge which was aligned to a reference CeO_2 sample provided by Sigma Aldrich (>99%). Energy alignment, background subtraction and edge-jump normalization were conducted with the Athena software from the Demeter package.[16] FT-EXAFS fit was conducted with the Artemis software from the same package. EXAFS fit procedure (fully described in the published manuscript reported in Appendix B[15]) was applied to extract scattering paths coordination numbers and radial distances. Concerning the fit of data collected during thermal treatments, the thermal Debye-Waller factors were modelled using the Einstein model as described in Appendix B.[15]

Hf as an internal reference. Hf is a natural dopant of Zr salts which is not-easily separate from ZrO_2 hence its concentration was evaluated by ICP analysis.[17,18] Hf participates neither to the CO_2 hydrogenation reaction nor in ZrO_2 tetragonal polymorph stabilization. Since its presence can be considered stable and constant during the whole reaction process, it can be used as an internal reference. By taking 3 ZnZr(X) samples (Figure 11a) normalized at the Zn K-edge we can observe as there is variation of Hf L_3-edge jump. This becomes clearer by normalizing the spectra at the Hf edge (Figure 11b) where Zn K-edge jump is observed to increase with Zn concentration. Indeed, by considering the latter normalization, we expressed Zn edge jump in function of Zn concentration obtaining the calibration line in Figure 11c. Since the same Zr salt precursor was used to prepare all the ZnZr(X) samples discussed in the thesis, this calibration line was used to evaluate the amount of Zn in samples with unknown concentrations and which available amount was too little to perform elemental analysis (e.g., ICP).

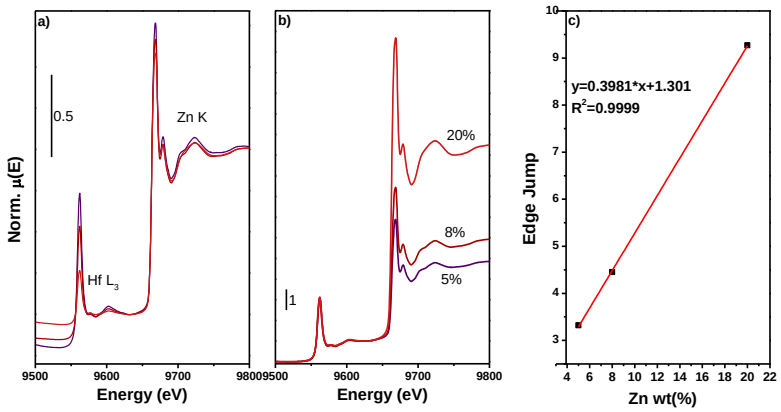

Figure 11 Zn K-edge and Hf L_3-edge energy regions for ZnZr(X) samples normalized at a) Zn K-edge and b) Hf L_3-edge. c) Zn concentration calibration line.

Ga K-edge XANES fit. Following the available literature[19,20] Ga K-edge XANES were fitted with pseudo-Voight (PV) (1) and arctangent function (2)

$$f(x) = \frac{A}{[1 + M(x - x_0)^2/\beta^2]\exp\{(1 - M)[(ln2)(x - x_0)^2/\beta^2]\}}$$

(1) Employed pseudo-Voight function where A, β, x0 and M are the curve height, full width half maximum, peak position and Lorentzian contribution ratio, respectively.

$$g(x) = B\left\{\left(\frac{1}{\pi}\right) arctan\left(\frac{x - x_0'}{\Gamma/2}\right) + (1/2)\right\}$$

(2) Employed arctangent function where B, Γ and x0' are the curve height, full width half maximum and inflection point, respectively.

For fitting Ga K-edge spectra 2 PV and 2 arctan functions were used to describe Ga tetrahedral (Td) and octahedral (Oh) coordination, respectively. M was fixed to 0.2 after its optimization through fitting Ga_2O_3 XANES as reference (Ga_2O_3 XANES fit results

	Tetrahedral				Octahedral			
	x0 (eV)	β (eV)	Γ (eV)	%	x0 (eV)	β (eV)	Γ (eV)	%
Ga2O3	10373.5	3.8	2.6	49	10376.7	4.1	1.2	51

) trying to maintain β, Γ, x0, x0' parameters for each couple included in their range found in literature (Table 1).[19,20] "A" was not constrained whilst B was fixed to 0.5 since spectra edge-jump was normalized to 1. Ga(Td) : Ga(Oh) ratio was quantitatively evaluated from the peak area ratio. The ratio obtained from Ga_2O_3 (as close as possible to 1) was used as feedback for evaluating the goodness of fit.

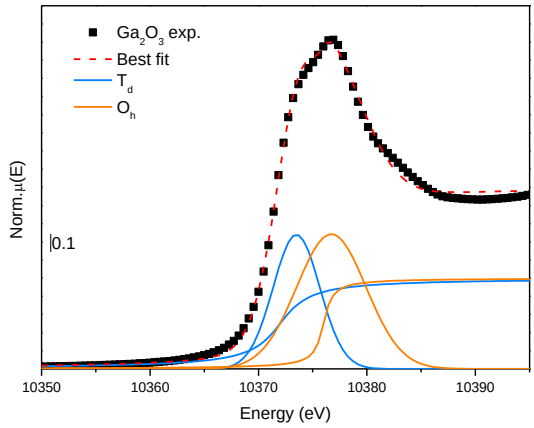

Figure 12 Ga_2O_3 XANES experimental spectra (squares) and best fit (dashed red line). Ga T_d and O_h pseudo Voight/arctan components are reported with blue and orange lines, respectively.

Table 1 Ga_2O_3 XANES fit results

	Tetrahedral				Octahedral			
	x0 (eV)	β (eV)	Γ (eV)	%	x0 (eV)	β (eV)	Γ (eV)	%
Ga_2O_3	10373.5	3.8	2.6	49	10376.7	4.1	1.2	51

Multi-edge approach. To have a complete description of the investigated catalysts a "multi-edge" approach was necessary. Indeed, XAFS spectra were measured not only for the guest element but also for the host matrix under the same conditions, allowing an improved parametrization of EXAFS fitting and a more complete description of the structure of the catalyst. For some specific elements such as Ce, we explored both K- and M_5-edges, which are in the hard and soft x-ray regions, respectively. The sensitivity of the two regions to bulk and surface properties gave access to important details of $Ce^{+3/+4}$ redox behaviour.

2.2.7 Multivariate Curve Resolution – Alternating Least Squares (MCR-ALS)

MCR-ALS is a powerful method to deconvolute a series of overlapping spectra presenting a significant variance. Briefly, a matrix D(m x n) is deconvoluted into two matrices C(m x k) and S^T(k x n) according to the equation : $D = SC^T + E$.

Spectroscopically speaking, D is a matrix where the rows represent energy points and columns the spectra, S is the matrix of the pure spectral profiles, C (^{T}: transpose) contains rows of concentration profiles related to each spectrum in S and E is the error matrix. The final aim of MCR analysis is then to identify the spectral components source of the variation observed in the dataset whilst the ALS procedure perform an alternated optimization of concentration and spectral profile at each cycle. It is then clear as this is a powerful chemometric approach to identify and quantify pure spectral components without possessing reference spectra of those components.

MCR requires an initial estimation of the number of components in the system. This it is done by Singular Value Decomposition (SVD) which describes the data into orthogonal vectors (e.g., linearly independent) helping the determination of the data matrix rank. This is probably the most complex and physically difficult task in the MCR process and has been carefully described in literature.[21] In all the reported MCR-ALS data the rank determination did not follow such a rigorous procedure as reported by Martini et al. [21] The elbow in the scree plot between variance and the component number was used to differentiate meaningful components from the data noise. This “non-golden rule” often leads to an ambiguous ranking assignment. Implicit assumption and “good practice” were then considered in support to the number of components determination. Another important step of MCR analysis is the rational application of constraints such as non-negativity and closure, which employment strongly depended on the dataset origin.

Indeed, MCR-ALS was applied to both XAS and FT-IR data in order to extract the pure spectral components and their concentration profiles. The main difference between the two datasets is on the applied constraints i.e., whilst non-negativity is applied to both XAS and FTIR spectral and concentration, closure is applied only to XAS data since in FTIR, due to different extinction coefficient of the formed species (e.g., carbonates, methoxides), closure is no longer valid.

References

(1) Ticali, P.; Salusso, D.; Ahmad, R.; Ahoba-Sam, C.; Ramirez, A.; Shterk, G.; Lomachenko, K. A.; Borfecchia, E.; Morandi, S.; Cavallo, L.; Gascon, J.; Bordiga, S.; Olsbye, U. CO 2 Hydrogenation to Methanol and Hydrocarbons over Bifunctional Zn-Doped ZrO 2 /Zeolite Catalysts. *Catal. Sci. Technol.* **2021**. https://doi.org/10.1039/D0CY01550D.

(2) Zhang, P.; Ma, L.; Meng, F.; Wang, L.; Zhang, R.; Yang, G.; Li, Z. Boosting CO2 Hydrogenation Performance for Light Olefin Synthesis over GaZrOx Combined with SAPO-34. *Appl. Catal. B Environ.* **2022**, *305* (December 2021), 121042. https://doi.org/10.1016/j.apcatb.2021.121042.

(3) Wang, S.; Zhang, L.; Zhang, W.; Wang, P.; Qin, Z.; Yan, W.; Dong, M.; Li, J.; Wang, J.; He, L.; Olsbye, U.; Fan, W. Selective Conversion of CO_2 into Propene and Butene. *Chem* **2020**, *6* (12), 3344–3363. https://doi.org/10.1016/j.chempr.2020.09.025.

(4) Gionco, C.; Paganini, M. C.; Giamello, E.; Sacco, O.; Vaiano, V.; Sannino, D. Rare Earth Oxides in Zirconium Dioxide: How to Turn a Wide Band Gap Metal Oxide into a Visible Light Active Photocatalyst. *J. Energy Chem.* **2017**, *26* (2), 270–276. https://doi.org/10.1016/j.jechem.2016.07.006.

(5) Manzoli, M.; Menegazzo, F.; Signoretto, M.; Cruciani, G.; Pinna, F. Effects of Synthetic Parameters on the Catalytic Performance of Au/CeO2 for Furfural Oxidative Esterification. *J. Catal.* **2015**, *330*, 465–473. https://doi.org/10.1016/j.jcat.2015.07.030.

(6) Zhu, Y. J.; Chen, F. Microwave-Assisted Preparation of Inorganic Nanostructures in Liquid Phase. *Chem. Rev.* **2014**, *114* (12), 6462–6555. https://doi.org/10.1021/cr400366s.

(7) Brunauer, S.; Emmett, P. H.; Teller, E. Adsorption of Gases in Multimolecular

Layers. *J. Am. Chem. Soc.* **1938**, *60* (2), 309–319. https://doi.org/10.1021/ja01269a023.

(8) Rodríguez-Carvajal, J. Recent Developments of the Program Fullprof. *Newsl. Comm. Powder Diffr. IUCr* **2001**, *26* (International Union of Crystallography), 12–19.

(9) Bozon-Verduraz, F.; Bensalem, A. IR Studies of Cerium Dioxide: Influence of Impurities and Defects. *J. Chem. Soc. Faraday Trans.* **1994**, *90* (4), 653–657. https://doi.org/10.1039/FT9949000653.

(10) Binet, C.; Badri, A.; Lavalley, J. C. A Spectroscopic Characterization of the Reduction of Ceria from Electronic Transitions of Intrinsic Point Defects. *J. Phys. Chem.* **1994**, *98* (25), 6392–6398. https://doi.org/10.1021/j100076a025.

(11) Hadjiivanov, K. I.; Vayssilov, G. N. Characterization of Oxide Surfaces and Zeolites by Carbon Monoxide as an IR Probe Molecule. *Adv. Catal.* **2002**, *47*, 307–511. https://doi.org/10.1016/S0360-0564(02)47008-3.

(12) Zecchina, A.; Scarano, D.; Bordiga, S.; Ricchiardi, G.; Spoto, G.; Geobaldo, F. IR Studies of CO and NO Adsorbed on Well Characterized Oxide Single Microcrystals. *Catal. Today* **1996**, *27* (3–4), 403–435. https://doi.org/10.1016/0920-5861(95)00202-2.

(13) Pokrovski, K.; Jung, K. T.; Bell, A. T. Investigation of CO and CO2 Adsorption on Tetragonal and Monoclinic Zirconia. *Langmuir* **2001**, *17* (14), 4297–4303. https://doi.org/10.1021/la001723z.

(14) Li, C.; Sakata, Y.; Arai, T.; Domen, K.; Maruya, K. Carbon Monoxide and Carbon Dioxide Adsorption on Cerium Oxide Studied by Fourier- Transform Infrared Spectroscopy. **1989**, *85* (4), 929–943.

(15) Salusso, D.; Borfecchia, E.; Bordiga, S. Combining X-Ray Diffraction and X-

Ray Absorption Spectroscopy to Unveil Zn Local Environment in Zn-Doped ZrO2Catalysts. *J. Phys. Chem. C* **2021**, *125* (40), 22249–22261. https://doi.org/10.1021/acs.jpcc.1c06202.

(16) Ravel, B.; Newville, M. ATHENA , ARTEMIS , HEPHAESTUS : Data Analysis for X-Ray Absorption Spectroscopy Using IFEFFIT. *J. Synchrotron Radiat.* **2005**, 537–541. https://doi.org/10.1107/S0909049505012719.

(17) Chertihin, G. V.; Andrews, L. Reactions of Laser Ablated Titanium, Zirconium, and Hafnium Atoms with Oxygen Molecules in Condensing Argon. *J. Phys. Chem.* **1995**, *99* (17), 6356–6366. https://doi.org/10.1021/j100017a015.

(18) Zheng, W.; Bowen, K. H.; Li, J.; Dąbkowska, I.; Gutowski, M. Electronic Structure Differences in ZrO 2 vs HfO 2. *J. Phys. Chem. A* **2005**, *109* (50), 11521–11525. https://doi.org/10.1021/jp053593e.

(19) Akatsuka, M.; Yoshida, T.; Yamamoto, N.; Yamamoto, M.; Ogawa, S.; Yagi, S. XAFS Analysis for Quantification of the Gallium Coordinations in Al2O3-Supported Ga2O3 Photocatalysts. *J. Phys. Conf. Ser.* **2016**, *712* (1), 3–7. https://doi.org/10.1088/1742-6596/712/1/012056.

(20) Nishi, K.; Shimizu, K. I.; Takamatsu, M.; Yoshida, H.; Satsuma, A.; Tanaka, T.; Yoshida, S.; Hattori, T. Deconvolution Analysis of Ga K-Edge XANES for Quantification of Gallium Coordinations in Oxide Environments. *J. Phys. Chem. B* **1998**, *102* (50), 10190–10195. https://doi.org/10.1021/jp982704p.

(21) Martini, A.; Borfecchia, E. Spectral Decomposition of X-Ray Absorption Spectroscopy Datasets: Methods and Applications. *Crystals* **2020**, *10* (8), 1–46. https://doi.org/10.3390/cryst10080664.

3 ZrO_2 doped with aliovalent elements (Ce, Zn, Ga): the need for a structural understanding of guest atom nature

3.1 Catalytic properties

The scientific community and particularly the COZMOS project are investigating doped ZrO_2 catalysts for their CO_2 hydrogenation properties.[1,2] M-doped ZrO_2 (M : Zn, Ce, Ga) catalysts showed interesting results concerning selective CO_2 hydrogenation to methanol with respect to pure ZrO_2 (Figure 13a) without implying the use of rare earth or noble elements e.g., Pt, Pd and Ni.[2–4] The catalysts' selectivity to methanol is exploited for increasing CO_2 conversion (<10%). Indeed, the oxides are physically mixed with an acid zeolite/zeotype (e.g. H-ZSM5, SAPO-34/18, H-SSZ13, etc.) which can directly convert methanol into hydrocarbons improving the global CO_2 conversion (Figure 13b).[5–11] As reported in Figure 13, whilst $ZnZrO_x$ and $GaZrO_x$ presented similar properties for CO_2-to-methanol conversion, once mixed with the acid zeolite $GaZrO_x$ outperform $ZnZrO_x$ and $CeZrO_x$ for both CO_2 conversion and propane selectivity.

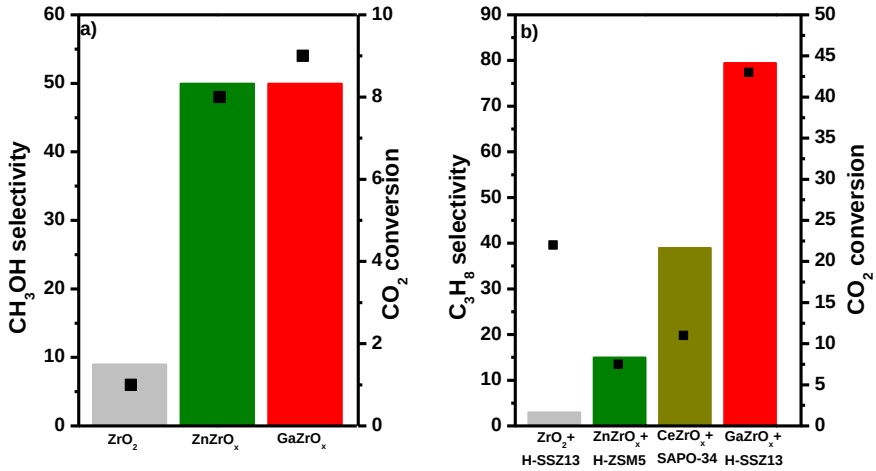

Figure 13 CH_3OH/Propane selectivity (bars) and CO_2 conversion (squares) properties of ZrO_2, $ZnZrO_x$,[7] $CeZrO_x$,[11] and $GaZrO_x$ [12] catalysts a) alone and b) physically mixed with acid zeolites.

Most of the reported studies focus on finding the best oxide/zeolite combination however, without providing a complete understanding of the oxidic catalyst structure.[6,9,10] The results reported in this chapter focuses on the structural comprehension of $ZnZrO_x$ and $GaZrO_x$ catalysts through PXRD and FT-EXAFS analysis. $CeZrO_x$ is used as an additional case study to support the obtained results.

3.2 $CeZrO_x$: understanding solid solution long- and short-range ordering

When describing ZrO_2 solid solutions, a typical example consists in CeO_2-ZrO_2 mixtures, which are well known catalysts widely employed because of their oxygen storage capacity and oxygen vacancies content.[13] The catalysts properties are very sensitive to the material local structure, making literature rich of their structural description using diffraction and FT-EXAFS.[14–16] Three major cases can be distinguished: A) CeO_2 and ZrO_2 are not well mixed forming nanoaggregates of different dimensions interacting only at their interface (Figure 14 left) (long-ordered domain type), B) CeO_2 and ZrO_2 are mixed on the long-range but a partial un-mixing remains at short range (Figure 14 middle) (shortly ordered domain type) and C) CeO_2 and ZrO_2 are perfectly mixed forming an ideal solid solution (Figure 14 right).

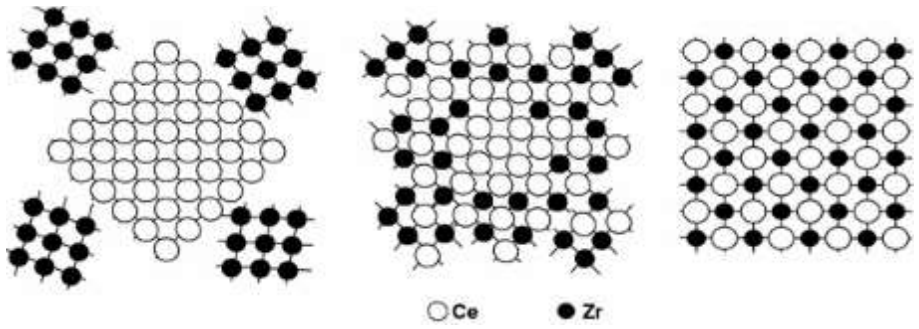

Figure 14 Pictorial representation of different solid solution scenario (from left to right): mixture of nanoscale oxides, partial local ordering, and perfect solid solution. Figure reproduced from Nagai et al.[14]

3.2.1 Average structural and electronic properties

Techniques such as PXRD and UV-Vis spectroscopy (Figure 15) probe the catalyst average structural and electronic properties, hence giving a macroscopic description of the catalyst. For example, in case of a commercial $CeZrO_4$ (Ce:Zr ratio of 58:42, full description of the catalyst reported in Appendix D)[4] PXRD pattern reported in Figure 15 shows a tetragonal ($P4_2/nmc$) average structure distinguished from the cubic CeO_2 Fm-3m from the presence of the (102) reflection. Indeed in the tetragonal polymorph the oxygen atoms are displaced along the [001] direction generating a modulation and inducing reflections of (odd odd even) type.[17] This polymorph is usually observed for $CeZrO_x$ catalysts and is often associated to the presence of oxygen vacancies introduced by Ce^{4+} and Zr^{4+} having different ionic radii (0.97 vs 0.84 Å)[18] hence causing expulsion of some oxygens during lattice relaxation. $CeZrO_4$ UV-Vis spectrum (Figure 15b) presents an absorption band different from ZrO_2 and CeO_2. Indeed, none of the two references band gap is observed in the catalysts and a broad absorption band is observed centred around 450 nm, usually associated to a Ce^{3+}-Ce^{4+} charge transfer,[19] suggesting the absence of clustering of one of the two oxides.

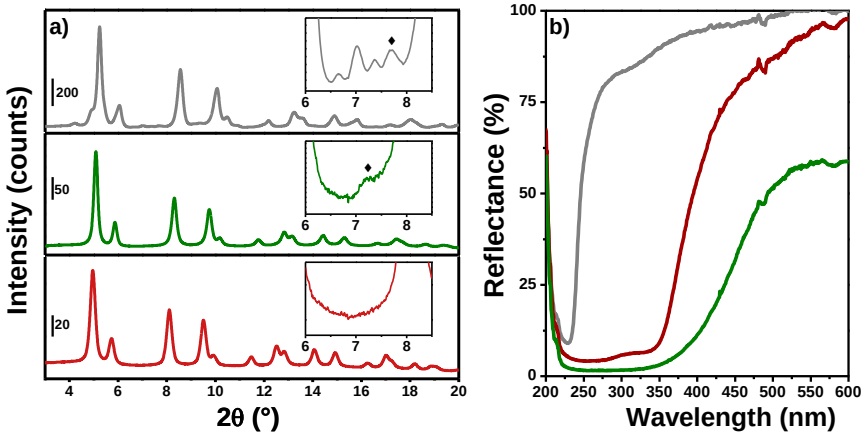

Figure 15 a) PXRD pattern ($\lambda \approx 0.27$Å) and b) UV-Vis spectra of ZrO_2 (gray lines), CeO_2 (red lines) and $CeZrO_4$ (green lines). (102) tetragonal reflection is indicated with a diamond in the insets in part a).

3.2.2 Zr/Ce local structure

From a local perspective, Zr K-edge XANES spectra (Figure 16a) presented a 1s→4p pre-edge related to non-centrosymmetric Zr-O coordination e.g., the ZrO_8 double tetrahedra coordination of the tetragonal polymorph.[20] On the contrary Ce K-edge XANES spectra is comparable with CeO_2 (cubic symmetry) with edge position shifted to lower energy (Figure 16b), highlighting the presence of Ce^{3+} already observed by UV-Vis spectroscopy (Figure 15b). A disordered Zr and Ce local environment is suggested from a first qualitative inspection of the phase-uncorrected FT-EXAFS regions which first and second shells intensities are dampened respect to the reference oxides. The first coordination shells position is comparable to the Zr-O and Ce-O from reference oxides whilst the second shells were initially assigned with a direct comparison with the pure oxides Zr-Zr and Ce-Ce intense shells positions.

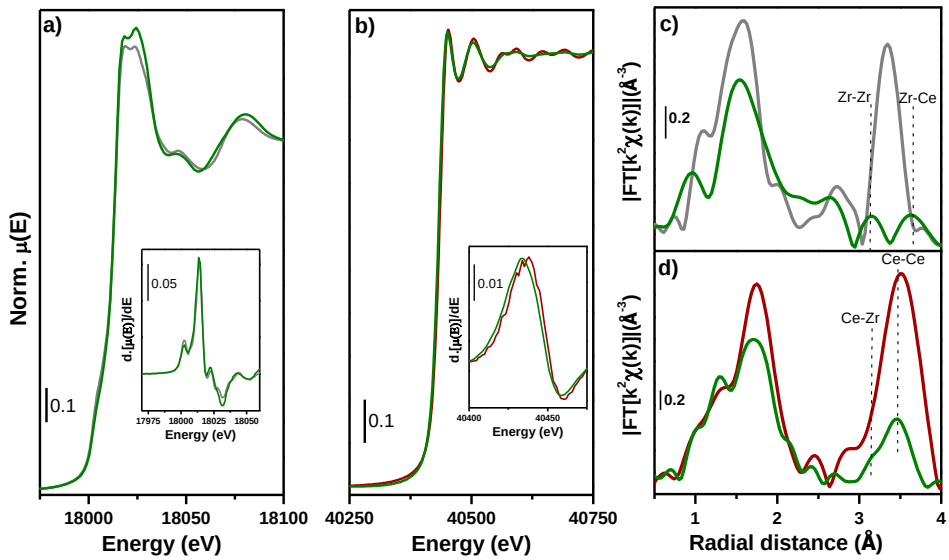

Figure 16 ZrO_2 (gray lines), CeO_2 (red lines) and $CeZrO_4$ (green lines) a,c) Zr K-edge a) XANES and c) phase uncorrected FT-EXAFS spectra (extracted in the 2-12 $Å^{-1}$ range) and b,d) Ce K-edge b) XANES and d) phase uncorrected FT-EXAFS (extracted in the 2-15 $Å^{-1}$ range) spectra. Detail of Zr K- and Ce K-edge XANES first derivative are shown in insets in panel (a) and (b) respectively.

To deep into Ce and Zr local structure we attempted a double edge fit where Ce-Zr and Zr-Ce radial distances and mean square displacements were constrained to the same values, accordingly to the potential presence of Zr-O-Ce chemical bond. Tetragonal ZrO_2 ($P4_2/nmc$) and cubic CeO_2 ($Fm\text{-}3m$) were used as input structures. Zr-Ce and Ce-Zr coordination number were instead constrained to Ce:Zr ratio evaluated by EDX analysis i.e., Ce = 4.8. The obtained results reported in

Table 2 consisted of physical values. However, whilst the fit well describes the experimental spectra at Ce K-edge (Figure 17 red panel), the same does not occur at Zr K-edge (Figure 17 blue panel), indicating as the employed $CeZrO_4$ solid solution model might not fully describe Zr local environment. Ce K-edge XANES (Figure 16 b) did not present any pre-edge fingerprints stemming from a CeO_8 non-centrosymmetricity hence we considered the local Ce-O cubic symmetry. Ce first coordination shell was then described with 8 equidistant oxygen atoms (Ce-O) which evaluated radial distance is well comparable with PXRD results (

Table 2). The second coordination shell was fit considering Ce-Ce and Ce-Zr scattering paths, both with same initial radial distance taken from PXRD refinement (≈3.72 Å) and correlated CN i.e., Ce-Zr CN : X and Ce-Ce : 12-X where X : number of Zr atoms as Ce next nearest neighbours (NNN) fixed according to Ce:Zr ratio evaluated by EDX. The evaluated radial distances unveiled a R(Ce-Zr) comparable with PXRD results and a R(Ce-Ce) closer to pure CeO_2 values (3.79 vs 3.84 Å) hence confirming the assignment hypothesized in Figure 16d. Following the local coordination evaluated from Zr K-edge XANES pre-edge, its FT-EXAFS first coordination shell was fit considering a double tetrahedra coordination with four closer ($Zr\text{-}O_I$) and four farther ($Zr\text{-}O_{II}$) oxygen atoms. On the contrary the second shell was described considering a Zr-Zr scattering path with independent radial distances and MSD, and a Zr-Ce path constrained to the Ce-Zr one. Interestingly, by considering the obtained Zr-Zr and Ce-Ce radial distances we noticed as their average (3.725 ± 0.043 Å) corresponds to the distance evaluated by PXRD (≈3.726 Å), highlighting the difference between a local and an average probe. However, whilst the fit well describes the experimental spectra at Ce K-edge (Figure 17 red panel), the same does not occur at Zr K-edge (Figure 17 blue panel), indicating as the employed $CeZrO_4$ solid solution model might not fully describe Zr local environment.

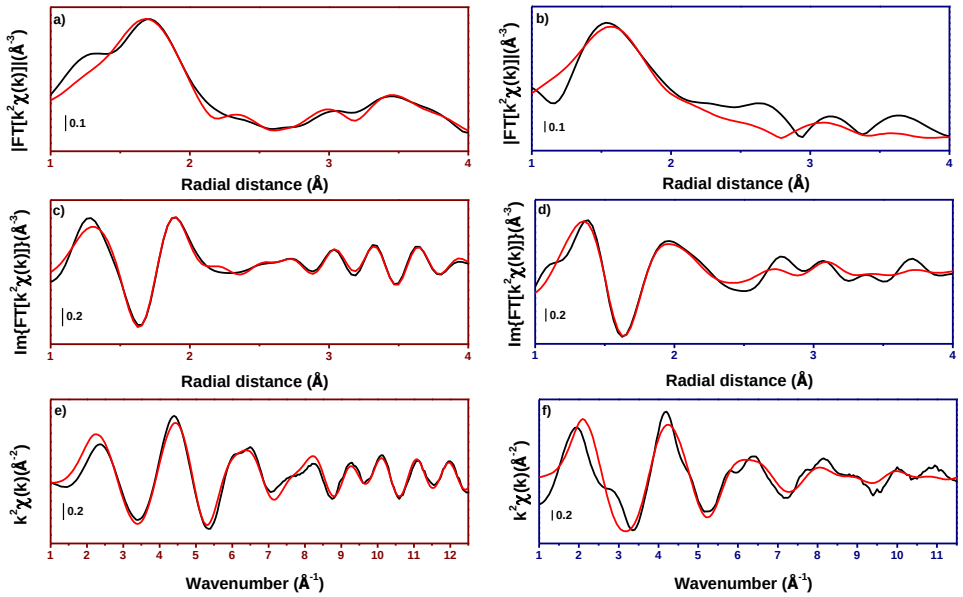

Figure 17 Ce K-edge (red panels) and Zr K-edge (blue panel) experimental (black lines) and best fit (red lines) of e,f) EXAFS and FT-EXAFS a,b) magnitude and c,d) imaginary part. Ce and Zr K-edges FT-EXAFS was extracted in the 3-12.4 and 3-11.4 $Å^{-1}$ k-range respectively. EXAFS fit was conducted in the 1-4 Å R-range at both edges.

Table 2 Radial distances (R), coordination number (CN) and Debye Waller factors (σ^2) obtained from $CeZrO_4$ PXRD Rietveld Refinement and Ce K- and Zr K-edges FT-EXAFS fitting. Fixed CN are indicated with *. Unphysical values are indicated with **bold** characters. SA : Sigma Aldrich. [a] Determined by PXRD refinement. [b] Determined by FT-EXAFS fit.

Sample	**Scatt. Path**	**R(Å)[a]**	**R(Å)[b]**	**CN**	**σ^2 (Å^2)**
$CeZrO_4$	Ce - O	2.28271	2.304±0.014	8	0.0111±0.0008
	Ce – Ce	3.7265	3.798±0.013	3±2	0.0063±0.0009
	Ce – Zr		3.744±0.013	9±2	0.016±0.003
	Zr – O_I	2.28271	2.12±0.05	4	0.008±0.003
	Zr - -O_{II}		2.26±0.09	4	0.012±0.010
	Zr – Zr	3.7265	3.667±0.041	9±2	0.017±0.005
	Zr - Ce		3.73±0.03	3±2	0.016±0.003

3.2.3 Deducing Ce-Zr short range ordering

Considering a perfect structural mixing between Ce and Zr the same radial distances and MSD should be obtained for common scattering path, as observed for example in CeZr clusters in UiO-66 catalysts.[21] From a mathematical viewpoint this result was achieved however, with an important misfit at the Zr K-edge second shell. Indeed, the difference between best fit and experimental data suggested as from Zr viewpoint at least one scattering component was missing in the second shell. Nevertheless, with the available data we did not try to model the local disorder to describe the missing scattering path. It is well reported as $CeZrO_x$ solid solution local structure (domain type vs solid solution) strongly depends on the synthesis strategy.[16] In the ideal solid solutions scenario (Figure 14 right), Zr second shell should be almost equal to Ce one (Ce:Zr≈1:1) whilst in scenario A (Figure 14 left), it should present an intense Zr-Zr component related to ZrO_2. The obtained lack of fit cannot

discard the formation of a perfect solid solution however, they clearly confirmed as the employed $CeZrO_4$ model does not describe Zr local environment. We then hypothesize as this particular sample might be located in the case scenario B (Figure 14 centre) where one of the cation (Ce) presents an higher degree of short range ordering respect to the other one (Zr).

3.3 Zn-doped ZrO_2: comprehension of Zn local environment

3.3.1 Powder X-Ray Diffraction (PXRD)

ZnZr(X) (X : Zn wt%) PXRD patterns (Figure 18) contain the same Bragg reflections, despite a series of extra peaks in the ZnZr(30) sample associated with a hexagonal ZnO extra phase. The tetragonal polymorph, further confirmed also from the Zr K-edge XAS analysis (vide infra), was used for Rietveld refinement of ZnZr(X) PXRD patterns (Figure 18) to extract lattice parameters, crystallite size, and phase composition. h-ZnO ($P6_3mc$) phase[22] was added to refine the extra reflections in the ZnZr(30) pattern. The effective Zn doping in the ZrO_2 structure can be simply verified by refined lattice parameters and the so-calculated unit cell volume. As the Zn^{2+} ionic radius (0.60 Å) is smaller than the Zr^{4+} one (0.84 Å), higher Zn loading consistently translates into a smaller unit cell volume (Figure 18d). It should be noteworthy as the unit cell volume evolution respect to Zn concentration does not respect the Vegard's Law which states a linear dependence between lattice expansion and guest atom concentration.[23] It should be stressed as this is only a qualitative interpretation of the unit cell volume behaviour. Indeed, to better understand ZnO solubility in ZrO_2, their binary phase diagram should be discussed. Unfortunately, as far as we could search into the literature, we did not find such diagram. Moreover, we should also expect as the ZnZr(X) tetragonal polymorph might be a metastable phase, suggesting that am hypothetical phase diagram might not be respected as well.

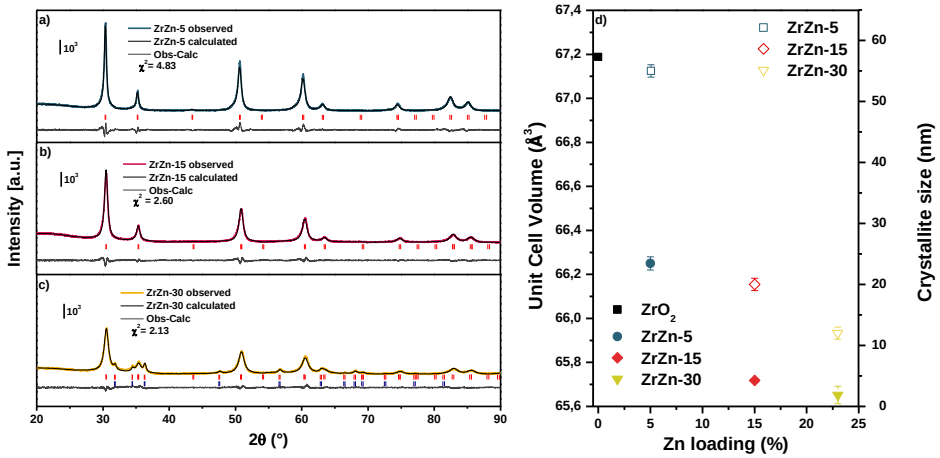

Figure 18 a,b,c) Laboratory PXRD (λ ≈ 1.54 Å) patterns measured for the three ZnZr(X) samples in transmission mode using glass capillary sample holder (Ø=0.5mm). Diffractograms for ZnZr(5)(blue curve), ZnZr(15) (red curve) and ZnZr(30) (yellow curve) are reported together with the corresponding refined curves (dark grey) and difference functions (light grey) between observed and calculated curves. t-ZrO_2 was used as the input structure for the refinement. t-ZrO_2 and h-ZnO Bragg reflections are indicated by red and blue vertical sticks, respectively. d) Unit cell volume (full symbols) and crystallite size (empty symbols) obtained from refined lattice parameters and peak shape, respectively, for ZnZr(5) (blue square), ZnZr(15) (red diamond) and ZnZr(30) (yellow triangles).

3.3.2 X-Ray Absorption Spectroscopy

Zr K-edge. XAS spectra of the three samples measured at RT in He atmosphere are reported in Figure 19, together with those of monoclinic and tetragonal ZrO_2 polymorphs, as references. Edge position, B/B' white-line peak split, and pre-edge shoulder "A" confirm the presence of ZrO_2 tetragonal polymorph. The latter one, more visible in the spectra first derivative, stems from a 1s→4d transition, characteristic of t-ZrO_2 where Zr coordinates 8 O atom in a non-centrosymmetric double tetrahedra configuration leaving open space for the presence of an oxygen

vacancy.[20] Moreover, Zr local geometry distortion increases with the Zn loading, as highlighted by the higher main edge FWHM (Figure 19)

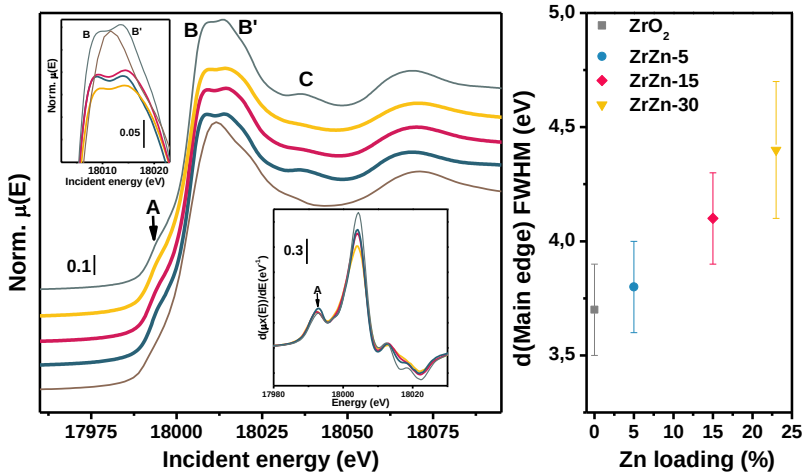

Figure 19 a) Stacked representation of Zr K-edge XANES measured at RT (He atmosphere) for the three ZnZr(X) samples. ZnZr(5) (blue), ZnZr(15) (yellow) and ZnZr(30) (red) are represented together with reference tetragonal (grey) and monoclinic (brown) ZrO_2 polymorphs. Top left inset: non-stacked detail of the white-line peak. Bottom right inset: XANES first derivative enhancing the pre-edge feature related to the 1s→4d transition. b) Main Edge FWHM for reference ZrO_2 and ZnZr(X) samples.

Phase-uncorrected Zr K-edge FT-EXAFS are reported in Figure 20a,b. The three spectra presented similar features: I) a first Zr-O shell located at 1.5 Å comparable between all the samples and substantially equivalent to that observed for the t-ZrO_2 model compound and II) a second shell at 3.2 Å associated to Zr-Zr scattering contribution which intensity is lower than reference ZrO_2 and is progressively abated as Zn concentration increases. Considering the presence of Zn as Zr Next Nearest Neighbour (NNN), Zr-Zr and Zr-Zn scattering contributions (Figure 20c) presented an imaginary component in complete antiphase, relating Zr second shell intensity loss with the increasing presence of Zn as NNN.

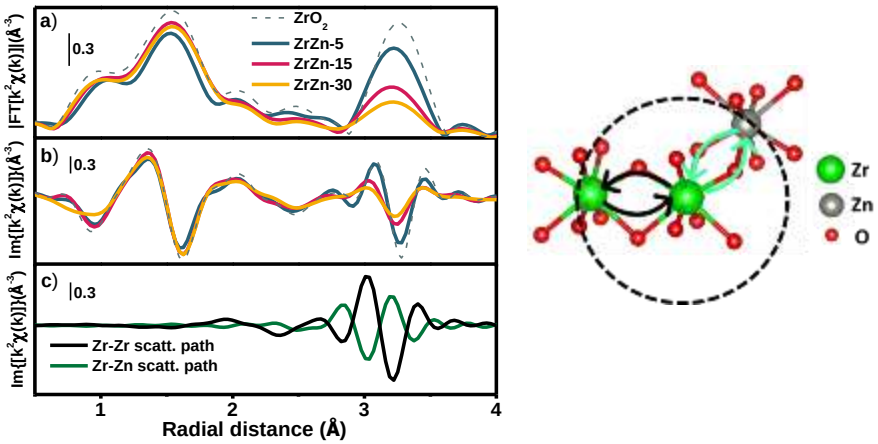

Figure 20 a) Magnitude and b) imaginary parts of k^2-weighted phase-uncorrected FT-EXAFS extracted in the k-range 2.5-12.0 $Å^{-1}$ for ZnZr(5) (blue), ZnZr(15) (red), ZnZr(30) (yellow) and reference t-ZrO_2 (dashed grey). c) Imaginary part of the individual Zr-Zr (black) and Zr-Zn (green) scattering paths generated by FEFF6 optimized after the fit of ZnZr(30). Left : sketched structural model describing Zr-Zr/Zn second coordination shell scattering paths.

To verify Zn role to the second shell dampening, EXAFS fits were conducted using tetragonal ZrO_2 model considering the presence of a Zr-Zn scattering path in second shell as sketched in the model in Figure 20. Even though the detailed fit procedure can be found in the published manuscript reported in the appendix,[24] the key parametrization of the fitting came from the description of Zn weight percentage. Since ARTHEMIS cannot handle non-integer occupancies, Zn was considered by replacing one of the 12 Zr atoms surrounding the absorber Zr by Zn and estimating Zr-Zr and Zr-Zn coordination number (CN) as 12-Zn and Zn, respectively, where Zn is a variable related to the number of Zn atoms as Zr NNN. To strengthen the fitting model, the same "Zn" variable was also considered in the Zr-O CN since every Zn^{2+} should introduce an V_O. The whole procedure, led to the best-fit curves reported Figure 21. A good agreement was observed for both magnitude and imaginary part of the FT-EXAFS spectra when comparing experimental and calculated curves.

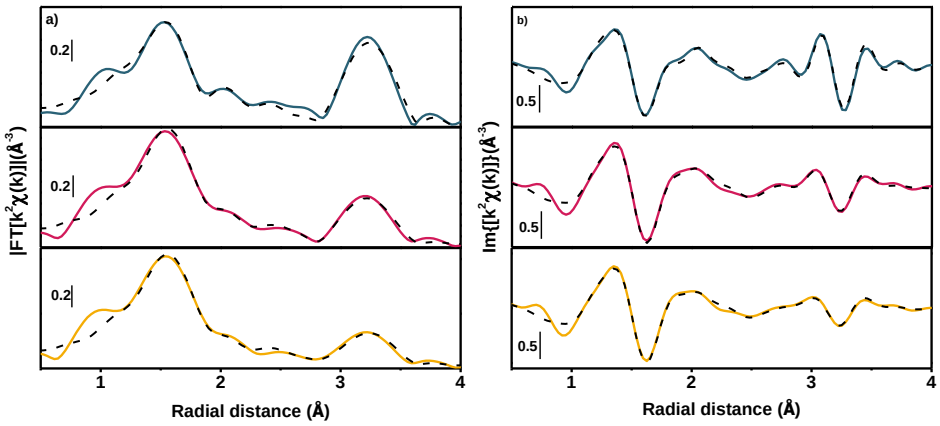

Figure 21 Experimental (coloured lines) and best fit (dashed grey lines) a) magnitude and b) imaginary parts of the k^2-weighted, phase-uncorrected FT-EXAFS spectra for ZnZr(5) (blue), ZnZr(15) (red) and ZnZr(30) (yellow).

Zn K-edge. The solid solution scenario, observed from Zr FT-EXAFS fitting, should be reproduced also from Zn K-edge viewpoint, measured quasi-simultaneously with the Zr K-edge ones. The spectra of the three ZnZr(X) samples are reported in Figure 22, together with Zn K-edge XANES spectra of h-ZnO and Zn metal foil references. Edge position reflected the presence of Zn^{2+} whilst white-line shape is no-longer comparable with h-ZnO one. Indeed, whilst the latter presents two clear spectral features indicated with letters A and B in Figure 22a related to 1s→4pπ and 1s→4pσ transitions, the former presented a single broader white-line which could be interpreted as deriving from a 1s→4pσ transition with reduced long range ordering. Noteworthy, A and B fingerprints are more evident in ZnZr(30) sample most probably due to the presence of segregated h-ZnO observed by PXRD. A fruitful information was derived from a straight comparison of Zr and Zn FT-EXAFS. Indeed, in the solid solution scenario, both should present a similar second shell related to the Zr-Zn and Zn-Zr scattering paths. Nevertheless, it was clearly observed as whilst the two edges presented comparable first coordination shell, Zn second shell was located at a (phase uncorrected) radial distance comparable to h-ZnO.

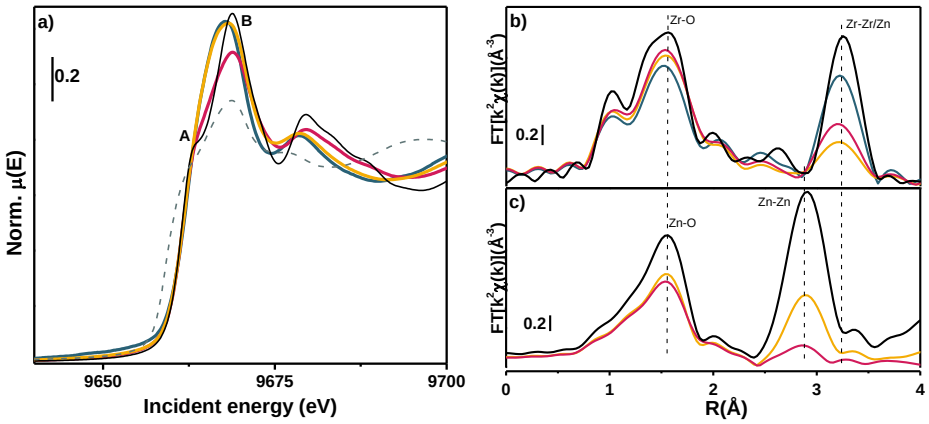

Figure 22 a) Zn K-edge XANES (main panel) and b) Zr and c) Zn K-edges phase-uncorrected k^2-weighted FT-EXAFS (inset) transformed in the 2-12 $Å^{-1}$ k-range measured at RT (He atmosphere), for the three ZnZr(X) samples. Spectra of ZnZr(5) (blue), ZnZr(15) (yellow) and ZnZr(30) (red) are shown together with those of reference h-ZnO (black) and Zn metal foil (dashed-grey). FT-EXAFS of ZnZr(5) is missing due to the low absorber concentration. FT-EXAFS spectra of reference ZrO_2 and h-ZnO are reported with black lines in parts b) and c), respectively.

Following this observation, the first Zn K-edge FT-EXAFS fit was conducted on ZnZr(15) by using hexagonal ZnO as input structure leading to a good data/fit agreement (

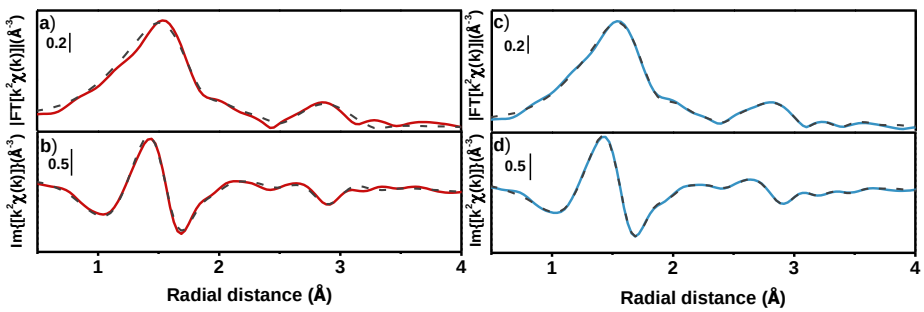

Figure 23a,b). Two details were observed: I) Zn-Zn shell intensity was lower than h-ZnO one, indicating a reduced Zn-Zn CN and II) a bump located at higher radial distances was not described. Even though this feature could be simply related to a

FT artifact, its radial position is qualitatively close to Zr second shell suggesting that it could be associated to a Zn-Zr scattering path.

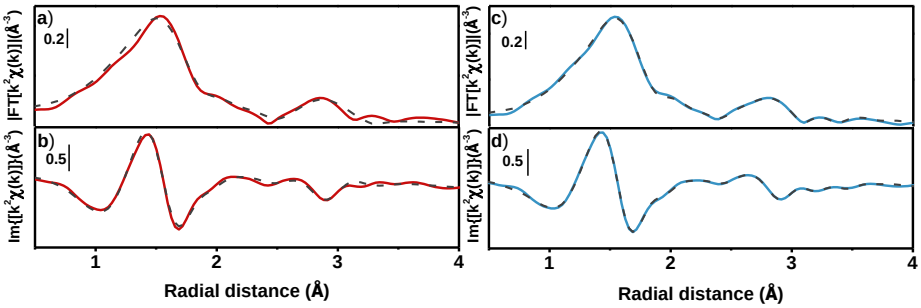

Figure 23 Experimental (solid coloured line) and best fit (dashed grey line) (a, c) magnitude and (b, d) imaginary parts for k^2-weighted FT-EXAFS of ZnZr(15) using (a, b) h-ZnO and (c, d) h-ZnO/ZrO_2 (Figure 20) as the input structure.

To discriminate the origin of this feature, XAFS spectra of ZnZr(15) at Zr and Zn K-edges were analysed under catalysts activation (Figure 24a,c).Whilst ZnZr(15) Zr and Zn K-edges of ZnZr(15) catalyst did not change upon the activation procedure described in the materials and methods, phase-uncorrected FT-EXAFS at Zn K-edge recorded during thermal activation in Figure 24a,c showed a constant decrease of the first and second shell intensity related to the increase in DW factors. However, the second shell presents a non-trivial dynamic involving the two components in the second shell. Indeed, the one at higher radial distances shifts to lower values until it convolutes with the Zn-Zn one at high temperature. After having discarded once more the simple h-ZnO model which did not describe the second shell dynamic (see Salusso et al.[24] for further details), we attempted to use the model sketched in Figure 25 for fitting the *in situ* data.

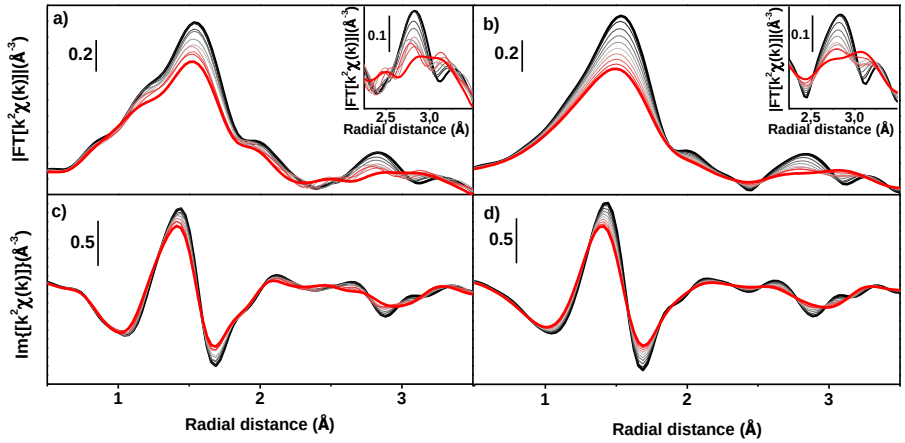

Figure 24 Zn K-edge a, c) Experimental and b, d) best fit of a, b) magnitude and c, d) imaginary parts of k^2-weighted FT-EXAFS of ZnZr(15) measured at increasing temperatures (black to red lines) in the RT-400 °C range under H_2 gas flow. A magnification of the second-shell region is reported in the insets. Fits are performed in the k-range 2-12 $Å^{-1}$ and R-range 1.0-4.0 Å.

Particularly, with this structural description we tried to integrate the results from both edges. Indeed, the average Zn atoms presents a non-trivial second shell composed by: I) a scattering contribution with Zn ($Zn\text{-}Zn_I$) located in ZnO bulk, II) scattering from a Zn atom bonded to Zr ($Zn\text{-}Zn_{II}$) and III) a direct scattering from Zr (Zn-Zr), previously observed from Zr K-edge. Using this structural description and by describing the thermal Debye Waller factor with the Einstein model we were able to well describe both first and second shell dynamics. This model was then used to fit also the data at RT under He, allowing a complete description of the component in second shell at higher radial distances.

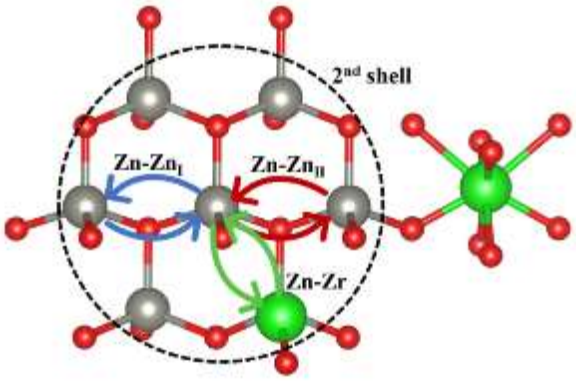

Figure 25 Pictorial representation of the scattering paths contributing in the second-shell region of Zn K-edge EXAFS, describing ZnO nanoclusters chemically bonded to the ZrO_2 matrix. Zn, Zr and O atoms are represented by grey, green and red spheres, respectively. 2nd shell is indicated by dashed circle while Zn-Zn_I, Zn-Zn_{II} and Zn-Zr scattering paths are represented by blue, red and green arrows, respectively. As this is only a representative illustration, Zr is represented in both tetrahedral and double-tetrahedral coordination.

3.3.3 ZnZr(X) : ZnO domain size

We then conclude as ZnZr(X) catalysts can be described with the solid solution scenario A (Figure 14 left) i.e., long-range ordered domain type, consisting of nanosized ZnO-like domains embedded and chemically bonded in a ZrO_2 matrix. This view, pictorially represented in Figure 25 and Figure 26, explains I) the presence of Zr-Zn scattering path observed from Zr K-edge and the observed Zn underestimation. In fact, from Zr K-edge we evaluate only the surface of the ZnO cluster, the bigger the cluster the higher the underestimation. II) Zn K-edge second shell predominantly resembling ZnO, III) ZnO cluster surface being affected by the bond with Zr and IV) at the ZnO/ZrO_2 the most of V_O will be generated, explaining the increase of Zr local disorder at higher Zn loading observed from Zr XANES main edge FWHM.

Interestingly, the dimension of ZnO cluster (under the hypothesis of a spherical shape) was evaluated using the Greegor and Lytle equation to be among 11 Å (Figure 26). Moreover, this type of description supported a qualitative interpretation of Zn K-edge recorded under reaction conditions. Indeed, after activation the catalyst was subjected to a high-pressure stream (15 bar) of CO_2 and H_2 at 300°C. However, even if almost any variations were observed at both edges, Zn K-edge FT-EXAFS presented some subtle (but not negligible) variations in the second shell, particularly in the region where scattering paths from ZnO and ZrO_2 interface have been observed, suggesting as the interface between the two oxides might be the catalyst part active for CO_2 hydrogenation.

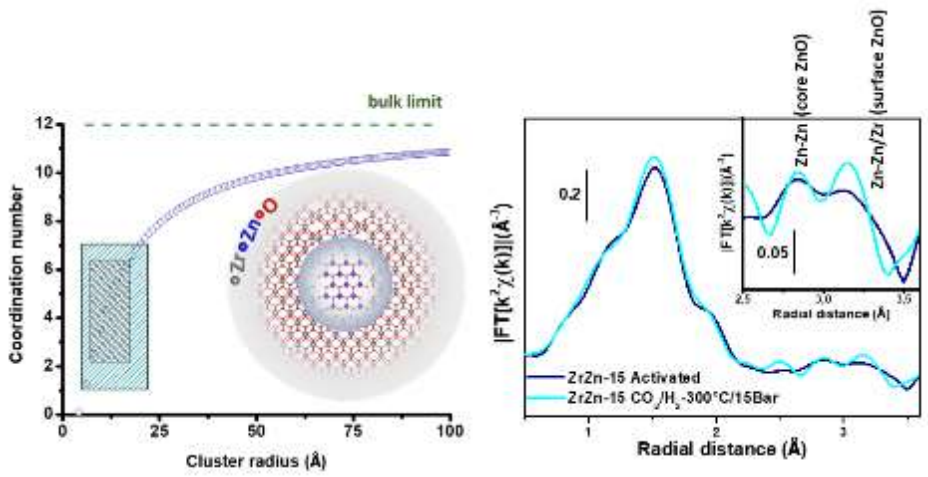

Figure 26 a) Relation between coordination number and cluster radius evaluated using the Greegor and Lytle equation within the spherical approximation. Zn-Zn distance found by EXAFS fit was used as shortest atomic distance. Outer and inner boxes indicate the area where CN extracted from fit of RT and under activation data are located, respectively. Dashed line indicates the coordination number bulk limit (12). b) Experimental magnitude part of k^2-weighted phase uncorrected FT-EXAFS of ZnZr(15) measured before (dark blue) and after (light blue) *in situ* reaction under CO_2/H_2 flux at 300°C, 15 bar. Insets showing detail of the R-space range where Zn-

Zn_I and Zn-Zn_{II}/Zr scattering contributions occur. In this R-space range, small modifications are observed upon exposure to the reaction feed for both the catalysts. Spectra were Fourier-transformed in the k-range 2-12 $Å^{-1}$.

3.4 ZnO clusters stability in ZnZr-X catalysts

After having described ZnZr(X) catalysts as consisting of ZnO nanoclusters in a ZrO_2 matrix, we decided to investigate how this structural configuration would affect the catalyst stability. Two new samples (ZnZr(10) and ZnZr(20)) were prepared and analysed by in -situ PXRD under H_2 activation to study the catalyst structural stability up to 600°C and by *ex situ* XAS after H_2 activation at different temperatures. Importantly, none of the two samples presented segregated h-ZnO reflections, therefore we could compare their Zn K-edge with the one of ZnZr(5)♣.

3.4.1 *Ex situ* XAS

Considering Zn present as ZnO nanoclusters, Zn K-edge XANES spectra in Figure 27a indicate that ZnO clusters are prevalently formed along the in-plane direction of the hexagonal lattice. As Zn concentration in the catalysts increases, a decrease of white-line intensity is observed, unveiling a lower unoccupied states density. Following Lee et al., ZnO particles of smaller diameters are expected to have larger surface-to-bulk atoms ratio which enhances near conduction band minimum surface states. Less unoccupied states are then associated to lower surface/bulk ratio, hence to larger ZnO clusters in ZnZr(X) catalysts. At energies slightly below the Zn K-edge, it can be observed the presence of Hf L_3-edge, a natural contaminant of ZrO_2. Even though it was showed that Hf has neither structural nor catalytic role,[7] it could actually be exploited as catalyst internal reference for direct quantification of Zn wt(%). In fact, while Hf abundance is the same in each catalyst since they share the same Zr precursor salt, Hf : Zn ratio changes with Zn loadings. By normalizing Zn

♣ZnZr(5) was measured as pellet during the same beamtime together with ZnZr(10/20). Unfortunately, ZnZr(15) was not available anymore to repeat the measurement in pellet.

K-edge spectra to the Hf L_3-edge we observe as Zn edge-jump becomes more pronounced as the Zn concentration increases. The values extracted after this normalization were used to build a Zn wt(%)/edge jump correlation line (Figure 27b).

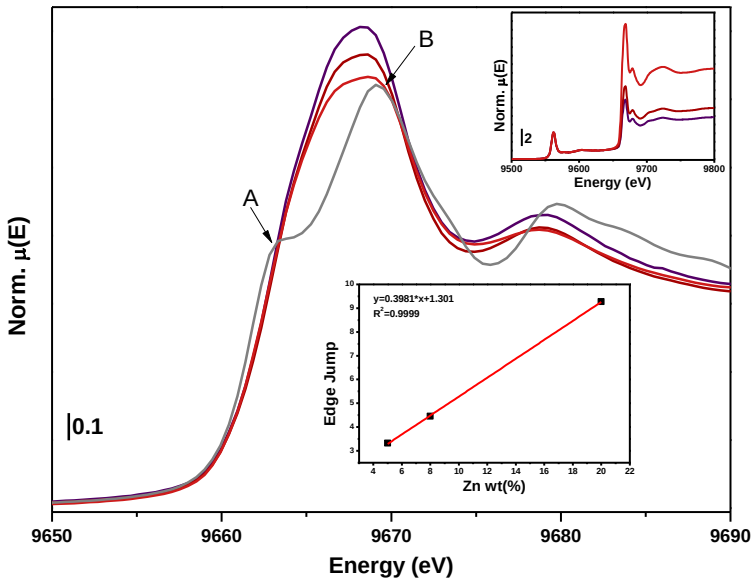

Figure 27 Zn K-edge (main panel) and Hf L_3-edge (top inset) normalized XANES spectra for ZnZr(5) (purple line), ZnZr(10) (dark red line), ZnZr(15) (red line) and ZnO (grey line). Zn wt(%) calibration curve is reported in the bottom inset.

This observation becomes useful when considering spectra with unknown Zn concentration i.e., ZnZr(20) (Figure 28) and ZnZr(10) after thermal treatments in H_2 at 550 and 700°C, namely ZnZr(20)_550, ZnZr(20)_700 and ZnZr(10)_700.♣ Hf : Zn ratio decreases as the reduction treatment temperature increases, suggesting a Zn concentration drop in the catalysts after reduction (Figure 28a). Indeed, by using

♣ For sake of brevity all the results for ZnZr(10) are not reported but they will be part of a manuscript in preparation.

these results we calculated that in ZnZr(20)_550 and _700 Zn wt(%) decreased to 13 and 3.7% whilst in ZnZr(10)_700 it dropped to 0.3%. Together with the decrease of Zn concentration, after H_2 treatment Zn K-edge 1s→$4p_{\sigma/\pi}$ transitions becomes more structured. In particular in ZnZr(20)_550 (Figure 28a) B component qualitatively increases whilst in ZnZr(20)_700 both A,B transitions are more defined and less intense, suggesting that ZnO cluster dimension first decreases with the loss of Zn concentration, while it subsequently increase at higher treatment temperatures. The same behaviour is observed for ZnZr(10) and for both catalysts it is more evident from Zn K-edge FT-EXAFS analysis. Indeed, whilst the first shell, related to Zn-O_{ZnO} ('ZnO': scattering paths from ZnO phase) does not change, the second shell intensity, previously defined as originating from a complex contribution of Zn-Zn_{ZnO}, Zn-Zn_{int} and Zn-Zr_{int} scattering paths ('int': ZnO/ZrO_2 interface), increases after treatment at 700°C/H_2 (Figure 28b).[24] Since the second shell intensity is directly dependent on the Zn-Zn_{ZnO} coordination number and it was previously used to estimate the ZnO cluster dimension, the rise of its intensity is direct evidence of ZnO cluster radius expansion.

Parallel to Zn, Zr K-edge (Figure 28c) gives a direct information on the matrix local structure and indirect hints on ZnO clusters. Zr XANES 1s→4p pre-edge and white-line B/B' splitting can be used to identify the tetragonal polymorph. Moreover, Zn-Zr scattering path was observed in Zr EXAFS second shell since the antiphase configuration between Zr-Zr_{ZrO2} and Zr-Zn_{int} paths caused a drop of its intensity. With the decrease of Zn abundance, Zr second shell is restored confirming a decrease of ZnO/ZrO_2 interface.

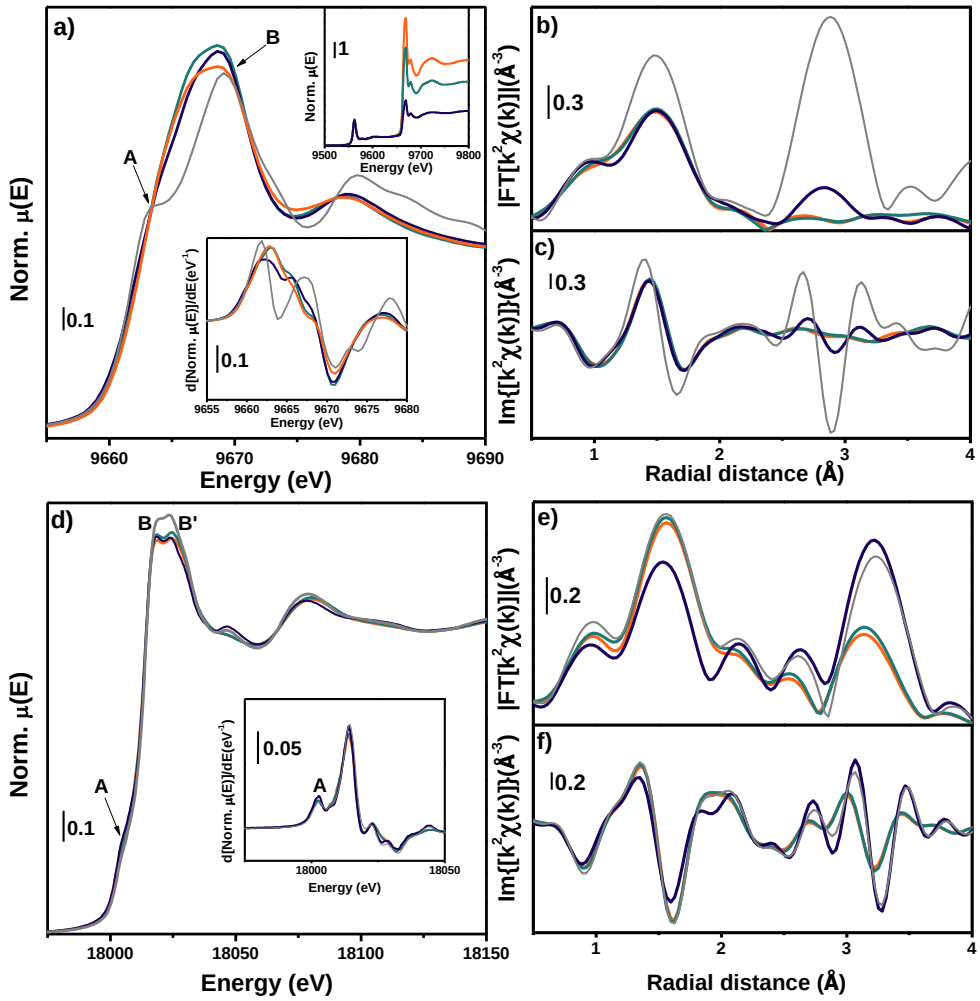

Figure 28 XANES (a, d) and k^2-weighted FT-EXAFS magnitude (b, e) and imaginary (c, f) parts for Zn (a, b, c) and Zr (d, e, f) K-edges of ZnZr(20) as prepared (orange line), ZnZr(20)_550 (green line) and ZnZr(20)_ 700 (blue line). FT-EXAFS have been extracted in the 2.3-10.4 $Å^{-1}$ k-space range. h-ZnO and t-ZrO_2 reference spectra are reported in grey. Hf L_3-edge are showed in the top inset in (a). XANES first derivative are reported in bottom insets in panels (a, d).

3.4.2 *Ex situ* and *In situ* PXRD

Ex situ PXRD data collected on the same samples (Figure 29a) showed the appearance of monoclinic reflections after H_2 treatment, suggesting a slight decrease

in the fraction of ZrO_2 tetragonal polymorph in favour of the monoclinic one. Moreover, H_2 reduction caused a shift to lower angles of t-ZrO_2 reflections unveiling an increase of the average unit cell volume. Indeed, the volume was showed to be inversely proportional to Zn concentration,[24] hence here confirming the Zn loss during H_2 reduction.

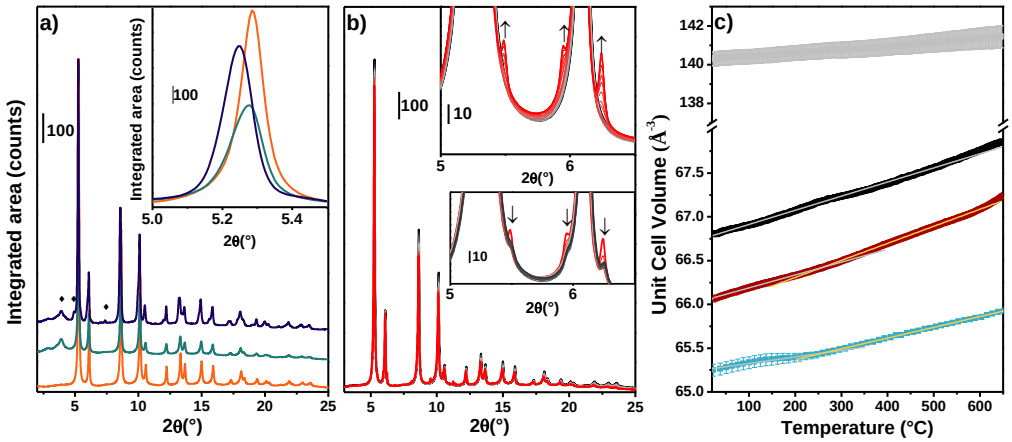

Figure 29 a) Stacked *ex situ* PXRD of ZnZn(20) (orange line), ZrZn(20)_550 (green line) and ZrZn(20)_700 (blue line). Main monoclinic Bragg reflections are indicated with diamonds. Detail of t-ZrO_2 (110) reflection is showed in the inset. b) ZnZr(20) PXRD pattern collected during H_2-TPR experiment. Temperature increases from RT (black line) to 650°C (red line). Detail of ZnO reflections during heating and cooling (temperature decreases from red to black line), indicated with arrows, are reported in the top and bottom insets, respectively. (c) Unit cell volume thermal evolution for reference t-ZrO_2 (black line) and m-ZrO_2 (grey line), ZnZr(10) (red line) and ZnZr(20) (light blue line). Linearity regions are showed with coloured lines.

To understand the Zn loss dynamic, *in situ* PXRD pattern for pure ZrO_2 and ZnZr(10)/20 catalysts have been then measured from RT to 650°C under H_2/He stream. RT-PXRD patterns indicate that the presence of Zn stabilized the tetragonal polymorph in ZnZr(20) catalysts (Figure 29b) decreasing its unit cell volume (Figure 29c). However, a clear difference was observed in the unit cell volume thermal

behaviour between pure ZrO_2 and ZnZr(10/20). In fact, as showed Figure 29c, whilst pure ZrO_2 behaves linearly until 500°C, ZnZr(10) and ZnZr(20) presented two regions of linear behaviour with distinct slopes. The first region (grey line Figure 29c) can be associated to unit cell thermal expansion while the steeper second one (yellow line Figure 29c) begins for both catalysts around 250 °C. The Zn loss highlighted by XAS could indeed be the reason for different unit cell expansion i.e., by decreasing Zn content the unit cell volume grows more rapidly since $R(Zn^{2+}) < R(Zr^{4+})$.[18] Moreover, at T > 600°C h-ZnO reflections started to be observed for ZnZr(20) catalyst (Figure 29b, inset), confirming as showed by XAS, that the Zn loss is accompanied by an increase in the average dimension of ZnO clusters, in which the residual Zn is organized. Our data suggest that such aggregation phenomenon gradually proceeds as temperature increases, until the characteristic h-ZnO reflections become visible by PXRD. Interestingly, h-ZnO reflections were not observed in RT *ex situ* diffractograms (Figure 29a). In the ZrZn-20 case we observe as during cooling under H_2 h-ZnO reflections intensity decreases (Figure 29b) suggesting that at lower temperatures ZnO dimension decreases to a certain extent, with a partial recover of ZnO cluster nanosizing.

Considering the results reported above we can conclude that the thermal stability of ZnZr(X) catalysts is strongly affected by ZnO domain-ordering. Indeed, as sketched in Figure 30, at high temperature ZnO cluster dimensions increase, facilitating Zn sublimation, and thus leading to the observed decrease in Zn concentration. Globally, this affects catalyst activity by i) reducing ZrO_2 tetragonal polymorph stability, which is more active than the monoclinic one and ii) lowering ZnO/ZrO_2 interface, the catalyst site active towards CO_2 hydrogenation. With the decreasing of the temperature, nanosized ZnO clusters are partially recovered however, with a substantial reduction in the total Zn concentration and larger cluster size with respect to the as-prepared catalysts.

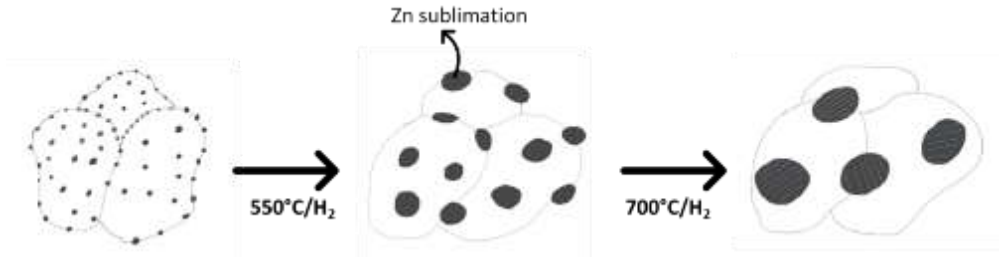

Figure 30 Proposed scheme for Zn loss dynamics in ZnZr(X) catalysts during H_2 activation.

3.5 Zn-doped ZrO_2 : catalyst deactivation after catalytic tests

3.5.1 *Ex situ* XAS

After having observed as Zn stability in ZnZr(X) catalysts is related to the formation of ZnO clusters which increases Zn volatility under H_2 at high temperatures, we measured *ex situ* Zn K-edge spectra of ZnZr(10) catalysts before (F-ZnZr(10)) and after (S-ZnZr(10)) catalytic test with (ZnZr(10)/S18) and without SAPO-18. Zn K-edge XANES spectra shows that Zn overall maintains the nanostructured ZnO-profile typically observed in these catalysts. In addition, a slight decrease of white-line intensity is observed in the spent catalysts (Figure 31a), associated to an increase of ZnO clusters dimensions. Even though ZnO clusters size increase is associated to a reduction of the total Zn concentration, as observed from Hf L_3-edge (Figure 31b,c), the lost Zn does not appear to diffuse in SAPO-18, as indicated by the absence of any additional spectral feature, possibly associated to Zn ions exchanged into the zeotype.

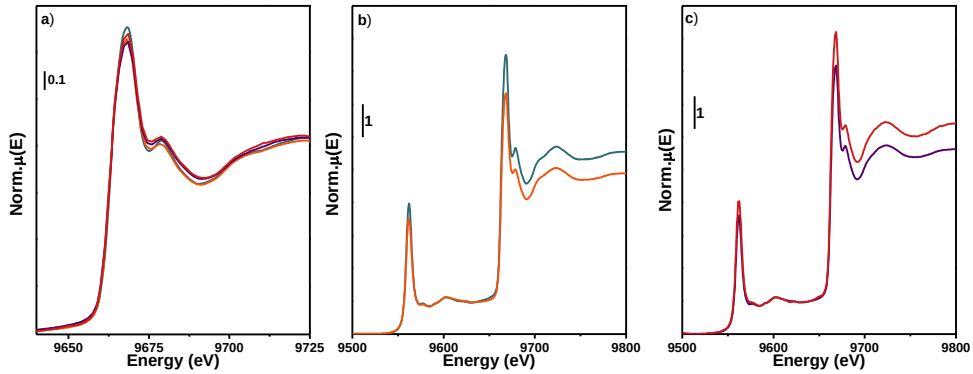

Figure 31 Zn K-edge XANES spectra for a) samples F-ZnZr(10) (blue line), F-ZnZr(10)/S18 (red line), S- ZnZr(10)/S18 (purple line), S-ZnZr(10) (orange line) and b) reference ZnO (grey line) and Zn(10%)Al_2O_3 (brown line). Hf L_3-edge XANES spectra for a) F-ZnZr(10) (blue line) and S-ZnZr(10) (orange line) and b) F-ZnZr(10)/S18 (red line) and S-ZnZr(10)/S18 (purple line).

3.6 $GaZrO_x$: from oxides clusters to the solid solution scenario

3.6.1 Catalyst average structure and electronic properties: PXRD and UV-Vis spectroscopy

Considering the solid solution scenario reported in Figure *14*, ZnZr(X) catalysts can described with the scenario A, which explains the parallel presence of ZnO nanoclusters in contact with a ZrO_2 matrix. This analysis was then applied to Ga-doped ZrO_2 catalyst which presented improved catalytic properties for CO_2 hydrogenation respect to ZnZr(X).[12] After reviewing literature results on different Ga concentrations (see Fend et al.[25]), GaZr(21) (21 wt% Ga loading) was chosen as case study sample. Considering PXRD pattern (Figure 32c) the same results reported for ZnZr(X) catalysts can be observed : I) tetragonal polymorph is stabilized respect to the monoclinic one, present in pure ZrO_2 prepared with the same synthesis strategy (Figure 32a) and II) the unit cell volume decreases as observed from the Bragg peak shift to lower angles. The t-ZrO_2 (102) reflection, quite visible in ZnZr(10) (Figure 32b), is not detected in GaZr(21) probably due to peak broadening induced by

crystallite size. Indeed, the tetragonal polymorph is confirmed from the Zr K-edge 1s→4p pre-edge peak.

To further investigate electronic properties of these catalysts, UV-Vis spectra in Figure 32d,e were measured and compared with those of the respective reference oxides i.e., ZnO, ZrO_2 and Ga_2O_3. ZnZr(X) spectra reflect the mixed oxides scenario. Indeed, ZnZr(5/10/15) spectra can be qualitatively described as a combination of reference ZrO_2 and ZnO. At higher Zn loadings, the series presented a band gap redshift towards ZnO one, likely be related to the quantum confinement reduction,[26] i.e., the smaller the ZnO cluster, the more blueshifted is the band gap, in agreement with larger ZnO cluster observed by XAS at higher Zn concentration (see Section 3.4.1). On the contrary GaZr(21) spectra reflects electronic properties not-identifiable by single ZrO_2 and Ga_2O_3, as observed for $CeZrO_4$ (Figure *15*b) suggesting an improved Ga dispersion in ZrO_2 lattice.

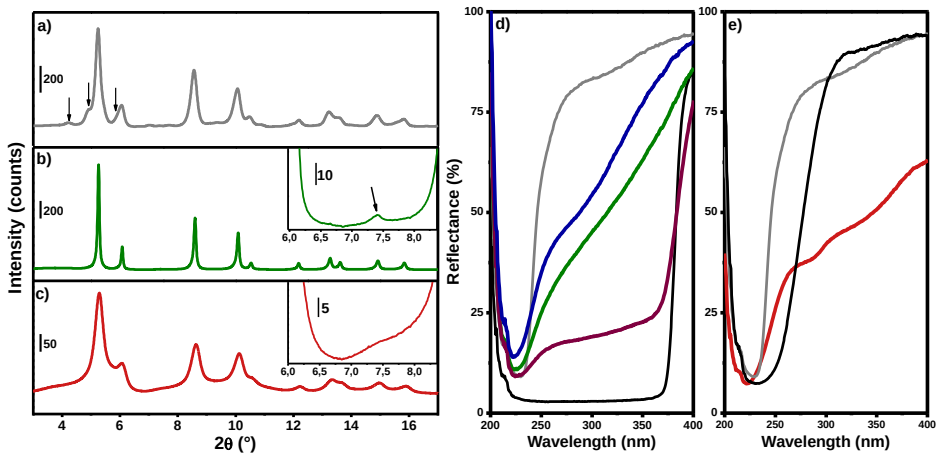

Figure 32 PXRD pattern (λ ≈ 0.27Å) for a) ZrO_2 (arrows indicate monoclinic reflections), b) ZnZr(10) and c) GaZr(21). t(102) Bragg peak is showed in the insets and indicated by an arrow. UV-Vis spectra for d) ZrO_2 (grey line), ZnZr(5) (blue line), ZnZr(10) (green line), ZnZr(15) (purple line) and ZnO (black line) and e) ZrO_2 (grey line), GaZr(21) (red line) and Ga_2O_3 (black line).

3.6.2 *In situ* XAFS: Ga local coordination

As discussed in the previous sections, ZnZr(10) Zn K-edge XANES spectra can be described considering a broadening of ZnO $1s \rightarrow 4p_{\pi}$ and $1s \rightarrow 4p_{\sigma}$ transitions. Using the same type of qualitative description, Ga K-edge XANES from reference beta-Ga_2O_3 (Sigma Aldrich >99%) (Figure 33a) is described with two components, associated to Ga with tetrahedral (T_d) and octahedral (O_h) coordination, respectively, showed in Figure 33d. GaZr(21) XANES spectra collected at RT (Figure 33a) consists of a single broad white-line which position suggests an higher abundance of T_d fraction. Moreover, after H_2 activation we observed an important decrease in the white-line intensity parallel to a slight shift of the edge position to lower energies. T_d/O_h ratio, evaluated with the fit procedure described in Chapter 2.2.6, showed as the as prepared sample contained already ≈74% of Ga(T_d) which increased to ≈78% after H_2 activation, relating the white-line intensity loss and the energy shift to a variation of T_d/O_h ratio (Figure 33a,b). If we consider Ga replacing Zr in ZrO_2 unit cell, Ga(T_d) might adapt easily to ZrO_8 double tetrahedral geometry respect to Ga(O_h), by introducing oxygen vacancies around Zr hence stabilizing the tetragonal polymorph. Indeed, only ≈26% of Ga has octahedral coordination, which could convert to the tetrahedral one by losing a pair of oxygen atoms during H_2 activation.

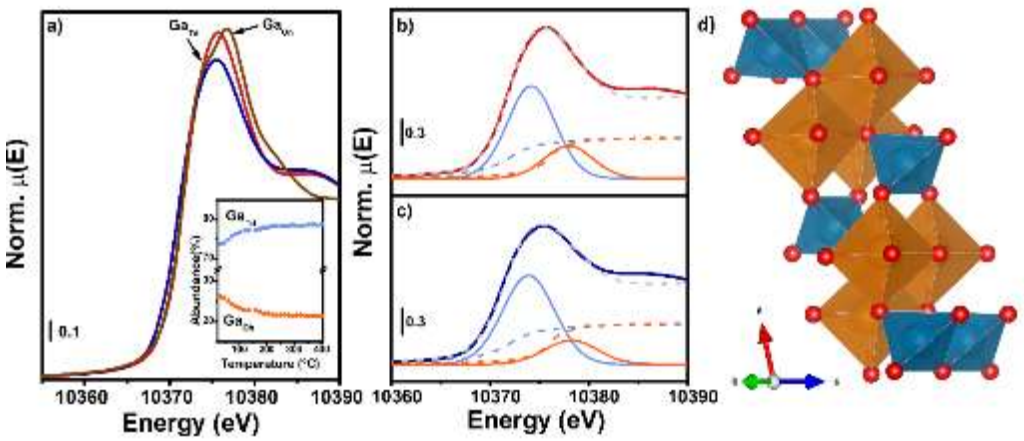

Figure 33 a) Ga K-edge XANES spectra at RT (red line) and 400°C (blue line) under H_2. Reference Ga_2O_3 is shown with brown line. Ga T_d (light blue squares) and O_h (orange squares) concentration evolution during H_2 thermal reduction is reported in the inset. Experimental (solid red line) and best fit (dashed grey line) Ga K-edge XANES measured at b) RT and c) 400°C with employed Pseudo Voigt (solid line) and Arctangent (dashed lines) functions to describe Ga T_d (light blue lines) and O_h (orange lines) components. d) Beta-Ga_2O_3 structure is reported on the right side with T_d and O_h polyhedral showed in blue and orange, respectively.

GaZr(21) Ga/Zr K-edges FT-EXAFS reported in Figure 34a,b gives an important information on Ga local geometry. Similarly, to ZnZr(10) sample, reported in Figure 34a,c for clarity, Zr K-edge second shell is abated due to Zr-Ga scattering paths having an imaginary component in antiphase respect to Zr-Zr. Differently from ZnZr(10), Zn FT-EXAFS first and second shell was likely ascribed to ZnO-like coordination, Ga K-edge presented a different scenario. Indeed, Ga K-edge first and second shell are not comparable to those of Ga_2O_3 suggesting the potential absence of Ga_2O_3 clustering.

The so observed Ga geometry improved the catalyst stability. Indeed, *ex situ* Ga K-edge XANES spectra collected on a spent catalyst after 14h of catalytic tests (Figure 34d) showed as ratio between Ga K- and Hf L_2-edges XANES spectra were almost

not modified after exposure to reaction conditions for long-time, highlighting as loss of Ga does not occur as instead observed for ZnZr(X) catalysts, reinforcing the hypothesis that Ga might be chemically inserted in ZrO_2 lattice.

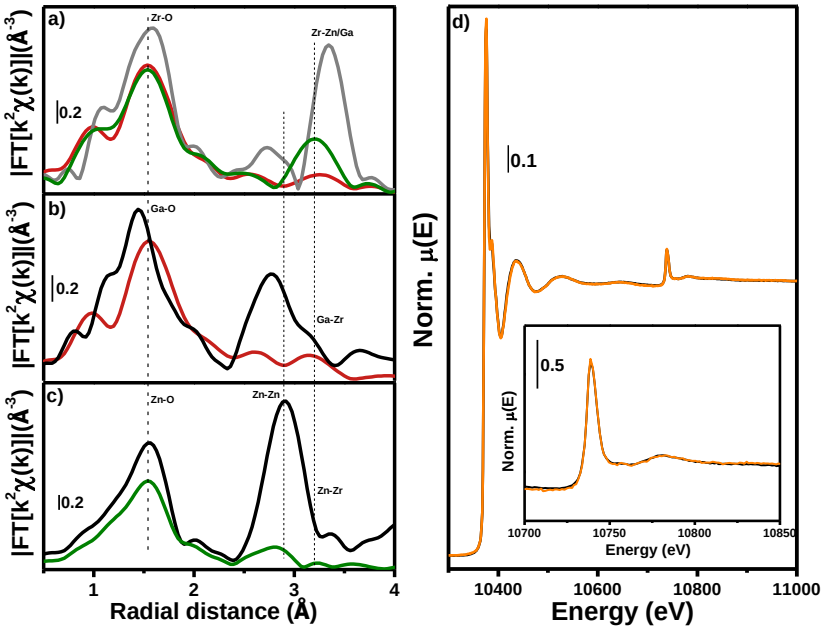

Figure 34 a,b,c) Magnitude of k^2-weighted phase-uncorrected FT-EXAFS for ZnZr(10) (green line) and GaZr(21) (red line) catalysts and ZrO_2 (grey line), Ga_2O_3 (black line) and ZnO (black line) extracted at a) Zr K-edge, b) Ga K-edge and c) Zn K-edge. d) Ga K-edge (main panel) and detail of Hf L_2 (inset) XANES spectra for F-GaZr(21) (black line) and S-GaZr(21) (orange line).

To further investigate Ga/Zr local environment, a double edge fit of the two edges FT-EXAFSs was conducted considering tetragonal ZrO_2 as input structure. Ga and Zr first coordination shell showed the presence of two cation-oxygen scattering paths from both edges viewpoint. Zr-$O_{I/II}$ scattering paths are associated to the double tetrahedra coordination, and their CN was related to the Ga content through a stoichiometric relation implying the formation of an V_O every 2 Ga atoms. The Ga content was constrained to 6 according to the total Ga evaluated by ICP analysis. As

sketched in Figure 35, Ga-O SS paths was described with 4 closer oxygens in tetrahedral (T_d) coordination (Ga-O_{Td}) and 6 farther oxygens in octahedral (O_h) coordination (Ga-O_{Oh}). The two scattering paths coordination number was weighted to the tetrahedral/octahedral above evaluated from XANES fit (≈74%) (Figure 33).

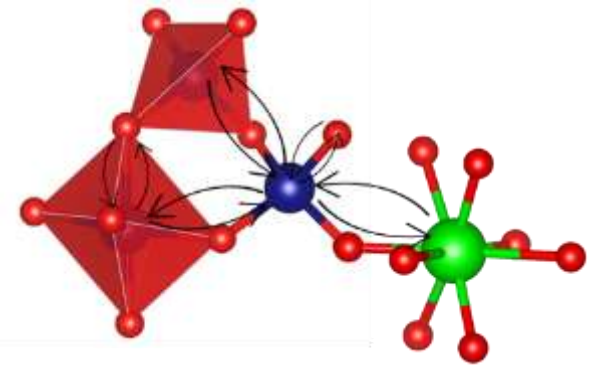

Figure 35 Proposed structural model for Ga local coordination. Scattering paths are indicated with arrows.

Unit cell parameters evaluated by PXRD Rietveld Refinement led to estimate the average the Zr/Ga-$O_{I/II}$ distances reported in Table *3*. Whilst PXRD gave an information on average distances, first shell FT-EXAFS fit provided a local information. By comparing Ga-O-Zr average radial distance with PXRD results (see equations below) we noticed as Ga-O_{Td}/Zr-O_I and Ga-O_{Oh}/Zr-O_{II} can be averaged to describe Ga_{Td}-O-Zr(O_{II}) ($\bar{R}_{\text{FT-EXAFS}}$: 1.98 Å vs R_{PXRD} : 2.05Å) and Ga_{Oh}-O-Zr(O_{II}) ($\bar{R}_{\text{FT-EXAFS}}$: 2.35 Å vs R_{PXRD} : 2.36Å) chemical bonds, respectively.

$$\frac{1.86(Ga - O_{Td}) + 2.09(Zr - O_I)}{2} = 1.98 \pm 0.04\text{Å} \approx 2.05\text{Å}(PXRD)$$

$$\frac{2.45(Ga - O_{Oh}) + 2.25(Zr - O_{II})}{2} = 2.35 \pm 0.11\text{Å} \approx 2.36\text{Å}(PXRD)$$

Zr second shell was described considering Zr-Ga and Zr-Zr SS paths with CN constrained to the Ga content, independent radial distances and Debye Waller

factors. Parallelly, Ga second shell presented a complex scenario: first of all, we considered a Ga-Zr scattering path with radial distance and Debye Waller factor constrained to the Zr-Ga one. Second, the structural model considered so far implied the presence of two Ga-Ga SS paths to describe both Ga in Td and Oh coordination, as done for the first coordination shell fit. The paths CN was weighted to the Ga content and to the Td/Oh ratio evaluated from Ga XANES fit (Table 3), independent radial distances were considered whilst since the same path is considered, the Debye Waller factor was fit to the same variable. The obtained results reported in Table 3 showed as the Zr-Ga/Ga-Zr SS paths presented comparable radial distance in line with PXRD result. At the same time Zr-Zr and Ga-Ga path resulted in longer and shorter distances respectively, in line with their ionic radii. Considering the latter path, it is noteworthy to notice that shorter and longer radial distances were evaluated for Ga-Ga_{Oh} and Ga-Ga_{Td} paths, in line with their difference in Ga_2O_3 (Ga-Ga_{Oh} ≈3.10Å vs Ga-Ga_{Td} ≈ 3.6Å). However, the evaluated Debye Waller factor presented a suspiciously large value (0.03$Å^2$) suggesting an high degree of structural disorder for these two paths. Moreover, the same comparison between radial distances evaluated by PXRD and FT-EXAFS done for first coordination shell can be applied to the second coordination shell. It is noteworthy to observe as the average distance evaluated by FT-EXAFS (see equation below) is closely comparable with PXRD results.

$$(3.49(Ga - Ga_{Td}) + 3.62(Ga - Ga_{Oh}) + 3.60(Ga - Zr) + 3.63(Zr - Zr))/4$$
$$= 3.59 \pm 0.12Å \approx 3.59Å(PXRD)$$

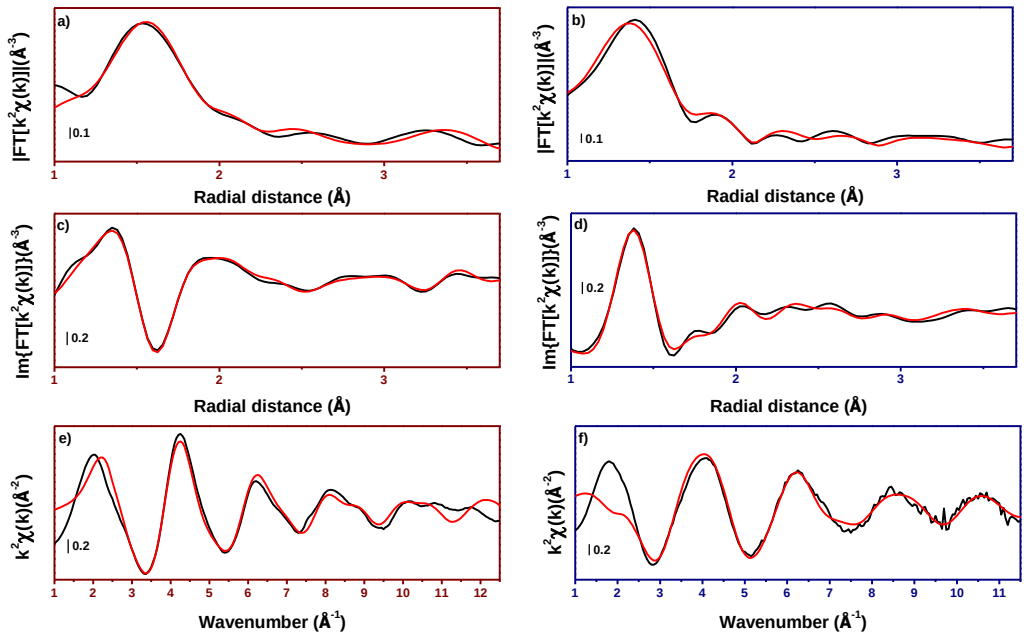

Figure 36 Zr K-edge (red panels) and Ga K-edge (blue panel) experimental (black lines) and best fit (red lines) of e,f) EXAFS and FT-EXAFS a,b) magnitude and c,d)imaginary components. Zr and Ga K-edges FT-EXAFS was extracted in the 2.3-11.4 $Å^{-1}$ k-range. EXAFS fit was conducted in the 1-3.7 Å R-range at both edges.

Table 3 GaZr(21) PXRD Rietveld refinement and FT-EXAFS fit results. R-factor = 0.011, employed 18 variables over 29 independent parameters. Ga K-edge: E_0 = -8± 5, Td=0.74, Ga=6. Zr K-edge : E_0 = -1.4±0.7 ,. [a] Determined from PXRD refinement. [b] Determined from FT-EXAFS fit.

Sample		**R(Å)[a]**	**R(Å)[b]**	**CN**	**σ^2 ($Å^2$)**
GaZr(21)	Ga-O_{Td}		1.86±0.04	4xT_d	0.004±0.003
	Ga-O_{Oh}		2.44±0.11	6x(1-Td)	0.004±0.003

	Ga-Ga_{Td}		3.5±0.3	GaxTd	**0.03±0.06**
	Ga-Ga_{Oh}		3.28±0.16	Gax(1-Td)	**0.03±0.06**
	Ga-Zr	3.5984	3.62±0.04	12-Ga	0.003±0.008
	Zr-O_I	2.0557	2.097±0.008	4-Ga/4	0.0074±0.0008
	Zr-O_{II}	2.3656	2.254±0.011	4-Ga/4	0.0031±0.0013
	Zr-Zr	3.5984	3.630±0.019	12-Ga	0.015±0.002
	Zr-Ga		3.60±0.04	Ga	0.023±0.008

3.6.3 Short range disorder: the price for solid solution formation

GaZr(21) was the last studied catalyst showing local ordering scenario completely different from $ZnZrO_x$ catalyst. The PXRD pattern presented tetragonal reflection however with abated intensities and broader FWHM respect to the other catalysts, indicating a smaller crystallite size hence a reduced long-range ordering. Moreover, the PXRD background presented an interesting modulation which will be object of future Total Scattering measurements for Pair Distribution Function extraction. Ga K-edge XANES indicates a high concentration of Ga T_d coordinated (≈74%). Ga content evaluated by ICP and its Td:Oh ratio were used as input parameters to conduct a double-edge fit of Zr and Ga FT-EXAFS spectra. The employed model considering Ga replacing Zr in its tetragonal unit cell, with Ga with either Td or Oh coordination well fit the experimental spectra. A high degree of disorder in the Ga-Ga coordination shell was observed, suggesting as this structural model could be only a preliminary description of this complex catalyst structure.

3.7 $ZnZrO_x$ stabilisation through Ce-doping: $ZnCeZrO_x$

To stabilize ZnZr(X) catalysts, ICC partner tried to include Zn in a Ce-doped ZrO_2 lattice.[27] The presence of Cerium should induce a volume expansion improving Zn

accommodation in ZrO_2 lattice. The obtained catalysts presented a single phase diffractogram ascribable to tetragonal ZrO_2 polymorph. The catalyst presented a stoichiometry of $Zn_{0.5}Ce_{0.2}Zr_{1.8}O_4$ evaluated by ICP-AES analysis and a surface area of 79.4 m^2/g. The catalyst catalytic properties were tested in combination with several zeolites (H-RUB-13, H-SAPO-34, H-ZSM-11 and H-ZSM-5) showing the highest CO_2 conversion (10.7%) and $C_2^=$-$C_4^=$ selectivity (83.4%) with H-RUB-13 at 350°C and 1MPa, which is an improvement respect to ZnZr(X) but lower then $GaZrO_x$.

To analyse the domain short range ordering stability of the catalyst, in-situ PXRD and XAS experiments were performed under activation and reaction conditions.

3.7.1 *In situ* experiment description

Quasi-simultaneous in-situ PXRD/XAS data were collected during the protocol described in Figure 37 at the BM31 beamline of the ESRF Synchrotron. The beamline set-up allows to switch between PXRD (λ=0.270Å) and the XAS monochromators with a total PXRD/XAS collection time of ≈5 minutes. Data were collected from a powder pressed in a capillary with diameter optimized depending on the measured K-edge (i.e. Zn, Zr and Ce). Due to capillary thickness, PXRD data were collected in parallel to XAS measurements at Zn K-edge, presenting the thinner capillary (Ø=0.5 mm) whilst Zr and Ce K-edge were collected by repeating the same experimental conditions without measuring the PXRD data on Ø=0.7 mm capillaries.

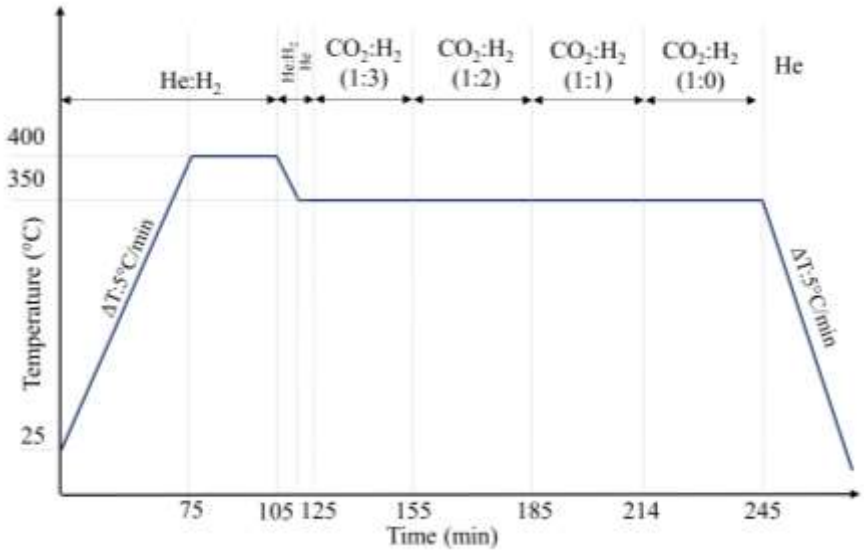

Figure 37 Activation/Reaction protocol employed for measuring quasi simultaneous in-situ PXRD/XAS data.

3.7.2 In-situ PXRD/XAS: catalyst activation

As for ZnZr(X) catalyst, the most relevant details on $ZnCeZrO_x$ (named ZCZ) structure were obtained during its activation under $He:H_2$ stream. The initial PXRD pattern collected at RT (Figure 38 a black line) presented t-ZrO_2 Bragg reflections, likely stabilized by Zn and Ce presence, with additional h-ZnO reflections (Figure 38 a arrows), highlighting the potential presence of long range ordered/segregated ZnO domains already in the as prepared catalyst. During thermal activation the catalyst structure is maintained i.e., no extra reflections were formed. However, important variations were observed in the t-ZrO_2 average unit cell volume and ZrO_2/ZnO relative concentration, reported in Figure 38b and c. Until 300°C the unit cell volume increases in line with reference ZrO_2 thermal expansion. However, at T>300°C the volume began to rise very rapidly until 400°C where it presented a decrease during the 30' holding, which will be rationalised hereafter. Parallelly, we noticed as the ZnO relative abundance increased respect to t-ZrO_2, in line with an increase of ZnO domains ordering observed for ZnZr(X) catalysts and explaining the

slope variation of unit cell expansion. It is noteworthy as the increase of ZnO content explains the peculiar evolution of the observed Bragg reflection some of which presented an intensity rise during heating (Figure 38a inset), in contradiction with the higher thermal Debye Waller contribution.

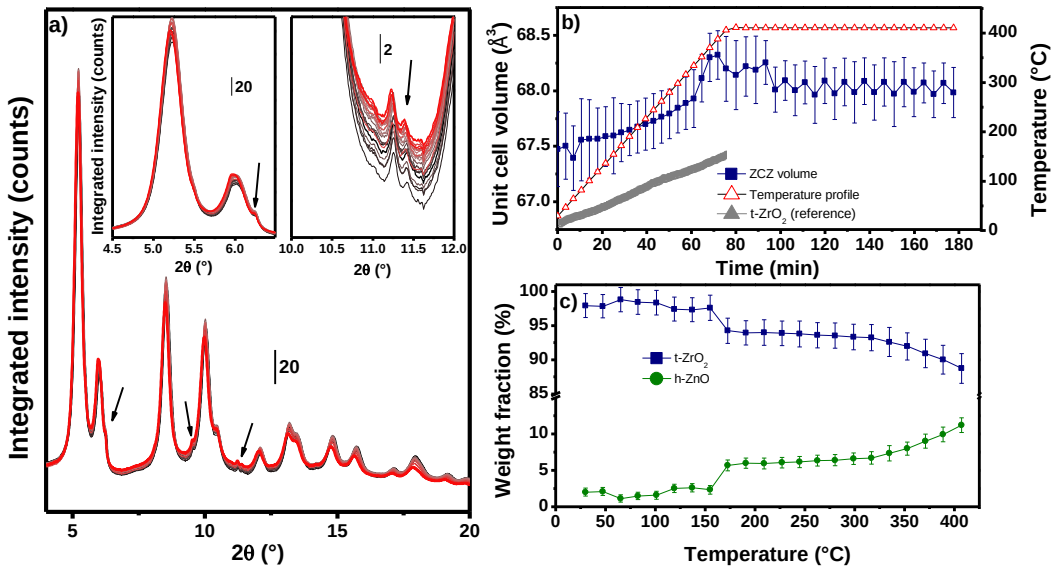

Figure 38 a) In-situ PXRD pattern ($\lambda \approx 0.27$Å) collected during catalyst activation under He:H_2 from RT (black line) to 400°C (red line). h-ZnO reflections are indicated with arrows. b) Unit cell volume and c) ZrO_2/ZnO relative abundances evaluated with Sequential Rietveld Refinement of the experimental diffractograms. Reference t-ZrO_2 unit cell volume expansion is reported with grey symbols for clarity.

Quasi-simultaneously to PXRD patterns we collected Zn K-edge spectra due to the employment of the thinner capillary (Ø=0.5 mm) whilst Zr and Ce k-edges were collected by following the same protocol reported in Figure 37, however, with thicker capillaries not allowing to collect also PXRD patterns.

The as prepared catalyst presented Zn, Zr and Ce K-edge XANES spectra (Figure 39 black lines) well ascribable to those previously observed for ZnZr(X) and $CeZrO_4$

catalysts (see Chapter 3.2). Zn K-edge (Figure 39 a) indicates a ZnO-like environment whilst Zr K-edge (Figure 39 b) highlighted the presence of the tetragonal polymorph from the 1s→4p pre-edge fingerprint of the ZrO_8 double tetrahedra coordination, both in line with the previous findings on ZnZr(5/10/15) catalysts. Differently from $CeZrO_4$ where some Ce^{3+} was already observed in the as-prepared catalyst, ZCZ Ce K-edge (Figure 39 c) presented a white-line shape and energy position indicating the presence of Ce^{4+} in a cubic CeO_2-like environment with Ce^{3+} concentration lower than the detection limit (<5%).

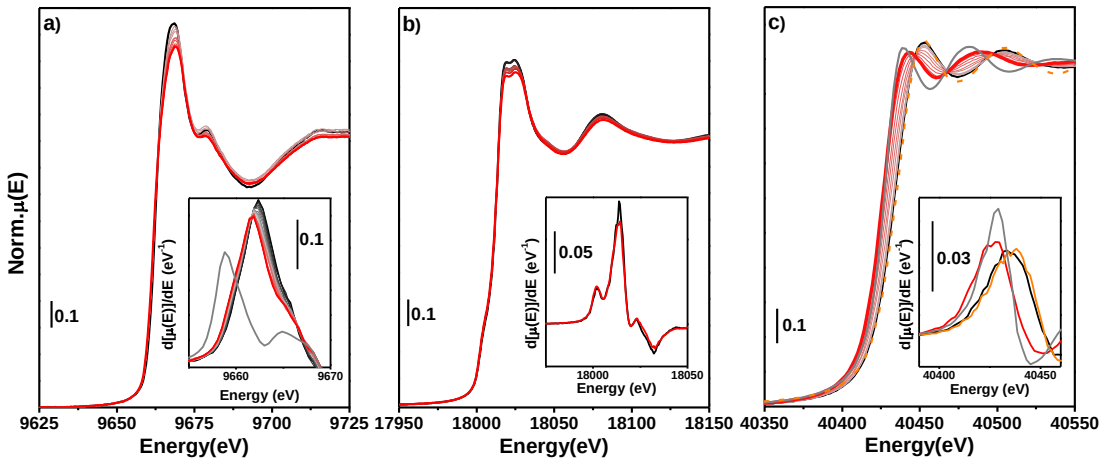

Figure 39 In-situ XANES spectra collected at a) Zn, b) Zr and c) Ce K-edges. Temperature increases from black to red line. Respective XANES first derivative is reported in the insets in every panel. Zn foil, $Ce(NO_3)_3$ and CeO_2 reference spectra are reported with grey and orange line, respectively.

As for ZnZr(X) catalysts, during activation no net variations were observed at Zr K-edge XANES spectra (Figure 39 b). Contrarily, at Zn K-edge we observed an important decrease of the white line intensity and a slight energy shift to lower energies of the rising edge, clearly visible in the spectra first derivative (Figure 39 a inset). The former spectral change, too large to be associated only to DW factor effect, could be related to an increase of ZnO domain size, as observed for ZnZr(X)

catalysts, in line with the rise of h-ZnO relative concentration extracted by PXRD Rietveld Refinement discussed in the previous paragraph (Figure 39 c). Furthermore, the spectra first derivative presented slight shift to lower energies with an additional weak contribution at energy position comparable with metallic Zn, indicating a potential $Zn^{2+} \rightarrow Zn^{\delta}$ ($2<\delta<0$) partial reduction. Parallelly, under the same conditions Ce K-edge (Figure 39 c) showed an important white-line and absorption edge shift to lower energies. Indeed, by comparing the collected spectra with CeO_2 and $Ce(NO_3)_3$ references (Figure 39 c) we noticed as ZCZ spectra collected at 400°C presented a shoulder in the rising edge at energies lower than Ce^{3+}. This is more visible in the XANES first derivative (Figure 39 c inset), suggesting the presence of Ce with oxidation state lower than Ce^{3+}.

To further investigate the electronic evolution of Ce states during the activation protocol, MCR-ALS routine was employed to extract the spectral component related to the final Cerium oxidation state. An unbiased MCR-ALS routine (not reported for brevity) led to two spectral components consisting in the two spectra collected at RT and 400°C respectively. Since we know that Ce has to go through the Ce^{3+} oxidation state before reaching the unknown final oxidation state, $Ce(NO_3)_3$ spectra was employed as reference component to extract the Ce^{3+} component i.e., 20 replicas of the spectra were reported after the experimental dataset. With this approach, the PCA allowed to extract the three components reported in Figure 40a. Considering the white-line/absorption edge energy position and post edge oscillation shape the spectra in red and green can be associated to those of Ce^{4+} and Ce^{3+} from CeO_2 and $Ce(NO_3)_3$ references, respectively. Contrarily the last spectrum (blue line) is not ascribable to any of the references and presented an energy position lower (>5eV) than Ce^{3+}. Ce metal foil XANES spectra could not be measured due to Ce(0) instability and reference Ce K-edge spectra for this oxidation state are rarely available in literature. Hence, we could not identify the oxidation state of the extracted component and from now on we will refer to it as $Ce^{\delta+}$. Nevertheless, the

obtained concentration profiles, reported in Figure 40b, unveiled an almost complete reduction of Ce^{4+} starting at 320°C with the formation of Ce^{3+} and $Ce^{\delta+}$, the latter becoming the most abundant component (≈60%) in the activated catalyst.

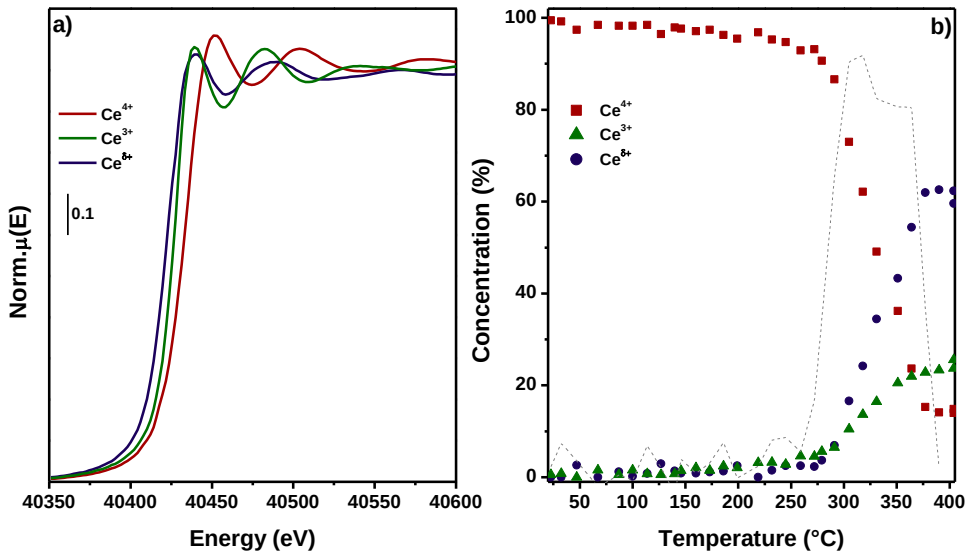

Figure 40 Ce K-edge XANES a) Spectra components and their respective b) concentration profile evolutions extracted from MCR-ALS routine. Ce^{4+} first derivative is reported with dashed grey line.

It is noteworthy as Ce and Zn reductions occurs parallelly, indicating a potential concerted reduction likely related to the formation of a Ce_xZn_y alloy further discussed with the FT-EXAFS analysis. Unfortunately, due to the low content of metallic Zn, an attempted MCR-ALS routine to Zn K-edge spectra (not reported for sake of brevity) did not allow to extract two meaningful components i.e., Zn^{2+} and Zn^0.

3.7.3 Ce surface reduction: *in-situ* near ambient pressure NEXAFS

Even though Ce K-edge spectra clearly showed the formation of strongly reduced $Ce^{\delta+}$ species on ZCZ catalyst, hard X-Ray measured in transmission mode are probing both bulk and surface of the catalysts, leaving uncertain Ce surface (i.e.,

reactive) oxidation state. For this reason, we decided to measure Ce M_5-edge NEXAFS spectra in Total Electron Yield (TEY) detection mode which reduced the X-Ray penetration depth to few nm enhancing the technique surface sensitivity. The measurement set-up available at APE-HE beamline allowed an almost complete reproduction of the hard X-Ray measurements however, limiting the maximum temperature to 375°C. Spectra collected during sample activation (RT-375°C/H_2:He 50 mL/min) are reported in Figure 41a. The results indicates a clear evolution from an initial spectrum at RT with shape and energy position, ascribable to Ce^{4+} (see CeO_2 reference in Figure 41b inset), to a final spectra at lower energy characterized by a double-edge fingerprint, comparable to Ce^{3+} reference spectra (see CeF_3 reference in Figure 41b inset).

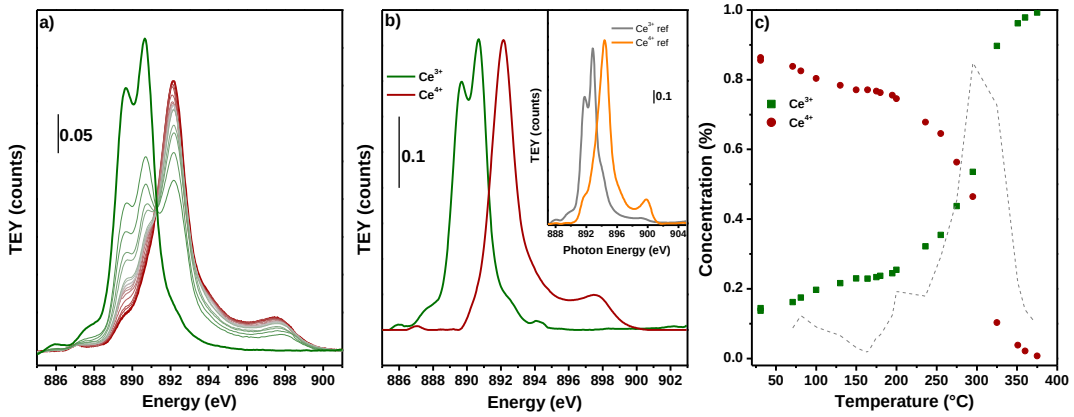

Figure 41 a) Experimental Ce M_5-edge collected under H_2:He (1:1 50 mL/min) stream from RT to 375°C. Temperature increases from red to green line. b) Concentration profile and c) spectra component extracted from MCR-ALS routine. Ce^{4+} first derivative is reported with dashed grey line. Reference CeO_2 (orange line) and CeF_3 (grey line) experimental spectra are reported in the inset in panel b).

Since Ce local environment affects the M_5-edge bands shape, particularly the feature at 898 eV, a linear combination fit using CeO_2/CeF_3 as references spectra was not possible. Contrarily, by applying an unbiased MCR-ALS routine i.e., without the use

of any reference spectra, we successfully extracted two spectra component reported in Figure 41b well comparable with $Ce^{4+/3+}$ references oxidation states (see Figure 41b inset). The components concentration profiles indicate a complete Ce^{4+}-to-Ce^{3+} reduction starting at 200°C and with a maximum variation at 300°C, both temperatures lower than what observed at Ce K-edge. It is noteworthy as Ce^{3+} and Ce^{0} have similar M_5-edge NEXAFS spectra, hence making their distinction almost impossible.[28] We should then consider as in the evaluated Ce^{3+} content, part of Ce might have oxidation state δ where $3<\delta<0$.

3.7.4 Ce_xZn_y alloy evolution under reaction-like conditions

To understand the behaviour of the ZCZ catalysts and particularly of the Ce_xZn_y alloy, Ce K-edge XANES and Ce M_5-edge NEXAFS spectra were collected under reaction-like conditions (350°C, CO_2:H_2:He 50 mL/min, 1 bar) varying the CO_2:H_2 ratio. From the spectra evolution reported in Figure 42 we immediately noticed a variation of their position and shape at both edges towards the reference Ce^{4+}. The collected spectra were analysed by MCR-ALS routine together with those measured during catalyst activation to completely describe the Ce species kinetic evolution with the extracted components discussed in the previous sections. The obtained Ce K-edge concentration profiles (Figure 42c) indicated as the presence of CO_2 causes a complete oxidation of Ce^{3+} to Ce^{4+} whilst $Ce^{\delta+}$ presented a higher stability, with a final Ce^{4+}/$Ce^{\delta+}$ concentration of ≈60/40%, respectively. Interestingly, the same behaviour was observed also at Ce M_5-edge (Figure 42d). We observed a Ce^{3+} oxidation to Ce^{4+} with the increase of CO_2 concentration, finishing with a final ratio under pure CO_2 comparable with the results obtained with hard X-ray.

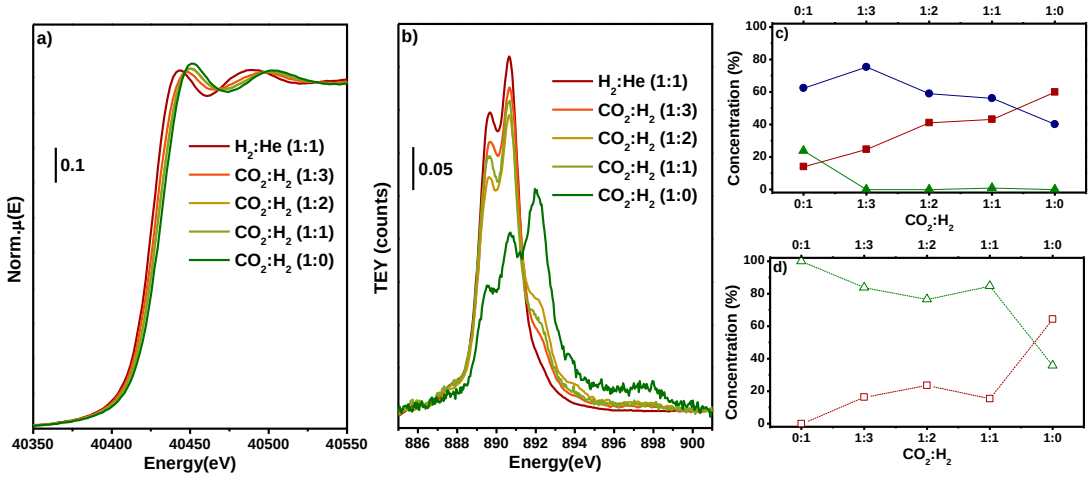

Figure 42 a) Ce K-edge XANES and b) M_5-edge NEXAFS spectra collected under 1 bar of different CO_2:H_2 ratio at 350°C. c,d) Ce^{4+} (squares), Ce^{3+}(triangles) and $Ce^{\delta+}$(circles) concentration profile extracted from MCR-ALS protocol applied to c) XANES (filled symbols) and d) NEXAFS (empty symbols) experimental spectra.

Since from hard X-Ray Ce^{3+} was observed to disappear completely with CO_2 presence in the feed, we can assume as the Ce^{3+} component observed by soft X-ray might be actually related to Ce(0), presenting a surface stability comparable with $Ce^{\delta+}$ observed in the catalyst bulk.

3.7.5 $ZnCeZrO_x$: simple rationalization of a complex system

The obtained results indicated as ZCZ catalyst presented a high degree of local structural complexity. The as prepared catalyst structure, sketched in Figure 43, consisted in a $CeZrO_x$ type 2 matrix with embedded ZnO domains larger than those previously observed for ZnZr(X) catalyst. Under reducing conditions (H_2, 400°C): I) ZnO domain size increases, influencing $CeZrO_x$ expansion linearity and II) Ce atoms are easily reduced first on the surface then in the bulk. The presence of a type 2 solid solution likely facilitates Ce migration at the highest temperatures (≈400°C) towards ZnO domains to form a Ce_xZn_y alloy on the domain surface, causing a drop of the unit cell volume and the Zr-Zr/Ce local radial distance. The formed Ce_xZn_y

presented a stability higher than Ce^{3+} under reaction like conditions i.e., in presence of CO_2, suggesting as this component might be the catalyst actual active part for CO_2 hydrogenation.

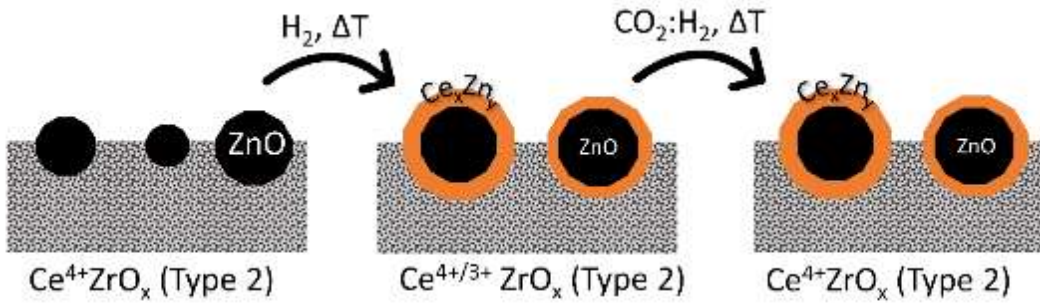

Figure 43 $ZnCeZrO_x$ structural evolution under activation and reaction conditions.

3.8 Conclusions

$ZnZrO_x$, $CeZrO_x$ and $GaZrO_x$ average structure was determined through Rietveld Refinement whilst guest atom/host matrix local structures were investigated by analysis of XANES and FT-EXAFS spectra collected at Zn K-, Ga K-, Zr K-, Ce K- and Hf $L_{3,2}$-edges. Even though the PXRD pattern (average structural probe) presented a single phase in all the three samples, it was observed particularly in the ZnZr(X) case where more data were available, as the unit cell volume did not change linearly with the guest atom concentration, hence not respecting the Vegard's law.[23] This is indeed a first indicator of the potential local order complexity respect to average structure reflected from PXRD patterns. Another indicator came from the UV-Vis (average electronic probe) spectra of the catalysts. Even if this technique is rarely employed for heterogenous catalysts characterization whilst more spread in photocatalysis, we here showed as it can be a powerful tool to verify if the sample presents new electronic properties (i.e., intimate guest atom/host matrix mixing) or it can be described with two different oxides (i.e., local domain ordering). Finally, analysis of XANES and FT-EXAFS spectra (i.e., local probes) unveiled as $ZnZrO_x$,

$CeZrO_x$ and $GaZrO_x$ can be referred to the three solid solution scenarios reported in Figure *14*. The conducted study showed as measuring both matrix and guest atom K-edges was fundamental to determine the local structure of the catalyst. It was observed as the average structure determined by PXRD was related to the long-range ordering of the matrix whilst the guest atom atom always presented a certain degree of local disorder. The guest atom dispersion respect to its clustering (domain ordering) is showed to drastically influence the catalyst properties. In term of activity, the guest atom dispersion increases the oxygen vacancies concentration hence improving the CO_2 conversion. On the contrary, it was observed as the guest atom clustering reduces the catalyst stability. Indeed, $GaZrO_x$ showed as Ga concentration did not change after reaction whilst $ZnZrO_x$ reported as the ZnO cluster dimension increased with a parallel decrease of the total Zn content. The detailed analysis on $Zn/CeZrO_x$ was used to understanding the peculiar behaviour of Zn-doped $CeZrO_x$. ZnO clustering was observed to occur also in this chase. However, during H_2 activation the presence of ZnO cluster to Ce atoms increased the reducibility of the latter at both bulk and surface scales. The Ce reducibility enhancement is ascribed to the formation of an intermetallic Ce_xZn_y compound presenting a high stability under reaction-like conditions. More detailed properties of this intermetallic and its role for CO_2 hydrogenation reaction will be object of future studies.

References

(1) Huang, J.; Li, W.; Wang, K.; Huang, J.; Liu, X.; Fu, D.; Li, Q.; Zhan, G. M XO Y-ZrO2 (M = Zn, Co, Cu) Solid Solutions Derived from Schiff Base-Bridged UiO-66 Composites as High-Performance Catalysts for CO2 Hydrogenation. *ACS Appl. Mater. Interfaces* **2019**, *11* (36), 33263–33272. https://doi.org/10.1021/acsami.9b11547.

(2) Dang, S.; Gao, P.; Liu, Z.; Chen, X.; Yang, C.; Wang, H.; Zhong, L.; Li, S.; Sun, Y. Role of Zirconium in Direct CO2 Hydrogenation to Lower Olefins on Oxide/Zeolite Bifunctional Catalysts. *J. Catal.* **2018**, *364*, 382–393. https://doi.org/10.1016/j.jcat.2018.06.010.

(3) Ramirez, A.; Ticali, P.; Salusso, D.; Cordero-Lanzac, T.; Ould-Chikh, S.; Ahoba-Sam, C.; Bugaev, A. L.; Borfecchia, E.; Morandi, S.; Signorile, M.; Bordiga, S.; Gascon, J.; Olsbye, U. Multifunctional Catalyst Combination for the Direct Conversion of CO 2 to Propane. *JACS Au* **2021**, *1* (10), 1719–1732. https://doi.org/10.1021/jacsau.1c00302.

(4) Ruzzi, P.; Salusso, D.; Baravaglio, M.; Szeto, K. C.; De Mallmann, A.; Jiménez, L. G.; Godard, C.; Benayad, A.; Morandi, S.; Bordiga, S.; Taoufik, M. Supported PdZn Nanoparticles for Selective CO2 Conversion, through the Grafting of a Heterobimetallic Complex on CeZrOx. *Appl. Catal. A Gen.* **2022**, *635* (November 2021). https://doi.org/10.1016/j.apcata.2022.118568.

(5) Ojelade, O. A.; Zaman, S. F. A Review on CO_2 Hydrogenation to Lower Olefins: Understanding the Structure-Property Relationships in Heterogeneous Catalytic Systems. *J. CO2 Util.* **2021**, *47* (January), 101506. https://doi.org/10.1016/j.jcou.2021.101506.

(6) Li, Z.; Qu, Y.; Wang, J.; Liu, H.; Li, M.; Miao, S.; Li, C. Highly Selective Conversion of Carbon Dioxide to Aromatics over Tandem Catalysts. *Joule*

2019, *3* (2), 570–583. https://doi.org/10.1016/j.joule.2018.10.027.

(7) Ticali, P.; Salusso, D.; Ahmad, R.; Ahoba-Sam, C.; Ramirez, A.; Shterk, G.; Lomachenko, K. A.; Borfecchia, E.; Morandi, S.; Cavallo, L.; Gascon, J.; Bordiga, S.; Olsbye, U. CO 2 Hydrogenation to Methanol and Hydrocarbons over Bifunctional Zn-Doped ZrO 2 /Zeolite Catalysts. *Catal. Sci. Technol.* **2021**. https://doi.org/10.1039/D0CY01550D.

(8) Liu, X.; Wang, M.; Yin, H.; Hu, J.; Cheng, K.; Kang, J.; Zhang, Q.; Wang, Y. Tandem Catalysis for Hydrogenation of CO and CO2 to Lower Ole Fi Ns with Bifunctional Catalysts Composed of Spinel Oxide and SAPO-34. **2020**. https://doi.org/10.1021/acscatal.0c01579.

(9) Kirilin, A. V.; Dewilde, J. F.; Santos, V.; Chojecki, A.; Scieranka, K.; Malek, A. Conversion of Synthesis Gas to Light Olefins: Impact of Hydrogenation Activity of Methanol Synthesis Catalyst on the Hybrid Process Selectivity over Cr-Zn and Cu-Zn with SAPO-34. *Ind. Eng. Chem. Res.* **2017**, *56* (45), 13392–13401. https://doi.org/10.1021/acs.iecr.7b02401.

(10) Li, Z.; Wang, J.; Qu, Y.; Liu, H.; Tang, C.; Miao, S.; Feng, Z.; An, H.; Li, C. Highly Selective Conversion of Carbon Dioxide to Lower Olefins. *ACS Catal.* **2017**, *7* (12), 8544–8548. https://doi.org/10.1021/acscatal.7b03251.

(11) Zhang, W.; Wang, S.; Guo, S.; Qin, Z.; Dong, M.; Wang, J.; Fan, W. Effective Conversion of CO 2 into Light Olefins along with Generation of Low Amounts of CO. *J. Catal.* **2022**, *413*, 923–933. https://doi.org/10.1016/j.jcat.2022.07.041.

(12) Sen, W.; Li, Z.; Pengfei, W.; Weiyong, Z.; Zhangfeng, Q.; Mei, D.; Jianguo, W.; Unni, O.; Weibin, F. Highly Selective Hydrogenation of CO2 to Propane. *NATCATAL-2*.

(13) Montini, T.; Melchionna, M.; Monai, M.; Fornasiero, P. Fundamentals and

Catalytic Applications of CeO2-Based Materials. *Chem. Rev.* **2016**, *116* (10), 5987–6041. https://doi.org/10.1021/acs.chemrev.5b00603.

(14) Nagai, Y.; Yamamoto, T.; Tanaka, T.; Yoshida, S.; Nonaka, T.; Okamoto, T.; Suda, A.; Sugiura, M. XAFS and XRD Analysis of Ceria-Zirconia Oxygen Storage Promoters for Automotive Catalysts. *Top. Catal.* **2008**, *47* (3–4), 137–147. https://doi.org/10.1007/s11244-007-9018-3.

(15) Nagai, Y.; Yamamoto, T.; Tanaka, T.; Nonaka, T.; Suda, A. Study on the Thermal Degradation of CeO2-ZrO2 Solid Solution by XAFS and XRD. *Phys. Scr. T* **2005**, *T115*, 664–666. https://doi.org/10.1238/Physica.Topical.115a00664.

(16) Vlaic, G.; Fornasiero, P.; Geremia, S.; Kašpar, J.; Graziani, M. Relationship between the Zirconia-Promoted Reduction in the Rh-Loaded Ce0.5Zr0.5O2 Mixed Oxide and the Zr-O Local Structure. *J. Catal.* **1997**, *168* (2), 386–392. https://doi.org/10.1006/jcat.1997.1644.

(17) Miyazawa, K.; Suzuki, K.; Sakuma, T. HREM Observation of Domain Boundaries in Tetragonal Zirconia. *Philos. Mag. B Phys. Condens. Matter; Stat. Mech. Electron. Opt. Magn. Prop.* **1993**, *67* (4), 595–599. https://doi.org/10.1080/13642819308207695.

(18) Shannon, B. Y. R. D.; H, M.; Baur, N. H.; Gibbs, O. H.; Eu, M.; Cu, V. Revised Effective Ionic Radii and Systematic Studies of Interatomie Distances in Halides and Chaleogenides. *Acta Crystallogr. Sect. A Found. Crystallogr.* **1976**, *32*, 751–767. https://doi.org/https://doi.org/10.1107/S0567739476001551.

(19) Schilling, C.; Hess, C. Real-Time Observation of the Defect Dynamics in Working Au/CeO2 Catalysts by Combined Operando Raman/UV-Vis Spectroscopy. *J. Phys. Chem. C* **2018**, *122* (5), 2909–2917.

https://doi.org/10.1021/acs.jpcc.8b00027.

(20) Li, P.; Chen, I. W.; Penner-Hahn, J. E. X-Ray-Absorption Studies of Zirconia Polymorphs. I. Characteristic Local Structures. *Phys. Rev. B* **1993**, *48* (14), 10063–10073. https://doi.org/10.1103/PhysRevB.48.10063.

(21) Lomachenko, K. A.; Jacobsen, J.; Bugaev, A. L.; Atzori, C.; Bonino, F.; Bordiga, S.; Stock, N.; Lamberti, C. Exact Stoichiometry of Ce x Zr 6-x Cornerstones in Mixed-Metal UiO-66 Metal-Organic Frameworks Revealed by Extended X-Ray Absorption Fine Structure Spectroscopy. *J. Am. Chem. Soc.* **2018**, *140* (50), 17379–17383. https://doi.org/10.1021/jacs.8b10343.

(22) Abrahams, S. C. and Bernstein, J. L. Remeasurement of the Structure of Hexagonal ZnO. *Acta Crystallogr. Sect. B Struct. Sci.* **1969**, *25*, 1233--1236. https://doi.org/10.1107/S0567740869003876.

(23) Kempter, C. P. Vegard's "Law." *Phys. Status Solidi* **1966**, *18* (2), K117–K118. https://doi.org/10.1002/pssb.19660180251.

(24) Salusso, D.; Borfecchia, E.; Bordiga, S. Combining X-Ray Diffraction and X-Ray Absorption Spectroscopy to Unveil Zn Local Environment in Zn-Doped ZrO2Catalysts. *J. Phys. Chem. C* **2021**, *125* (40), 22249–22261. https://doi.org/10.1021/acs.jpcc.1c06202.

(25) Feng, W. H.; Yu, M. M.; Wang, L. J.; Miao, Y. T.; Shakouri, M.; Ran, J.; Hu, Y.; Li, Z.; Huang, R.; Lu, Y. L.; Gao, D.; Wu, J. F. Insights into Bimetallic Oxide Synergy during Carbon Dioxide Hydrogenation to Methanol and Dimethyl Ether over GaZrOxOxide Catalysts. *ACS Catal.* **2021**, *11* (8), 4704–4711. https://doi.org/10.1021/acscatal.0c05410.

(26) Caetano, B. L.; Santilli, C. V.; Meneau, F.; Briois, V.; Pulcinelli, S. H. *In Situ* and Simultaneous UV-Vis/SAXS and UV-Vis/XAFS Time-Resolved Monitoring of ZnO Quantum Dots Formation and Growth. *J. Phys. Chem. C*

2011, *115* (11), 4404–4412. https://doi.org/10.1021/jp109585t.

(27) Wang, S.; Zhang, L.; Zhang, W.; Wang, P.; Qin, Z.; Yan, W.; Dong, M.; Li, J.; Wang, J.; He, L.; Olsbye, U.; Fan, W. Selective Conversion of CO_2 into Propene and Butene. *Chem* **2020**, *6* (12), 3344–3363. https://doi.org/10.1016/j.chempr.2020.09.025.

(28) Yağci, O. The M4, 5 Photo-Absorption Spectra of Cerium in Ce02 and Oxidation of Metallic Cerium. *J. Phys. C Solid State Phys.* **1986**, *19* (18), 3487–3495. https://doi.org/10.1088/0022-3719/19/18/020.

(29) Zelinska, O.; Conrad, M.; Harbrecht, B. Refinement of the Crystal Structure of Cerium Zinc (1:11), CeZn11. *Zeitschrift fur Krist. - New Cryst. Struct.* **2004**, *219* (1–4), 389–390. https://doi.org/10.1524/ncrs.2004.219.14.389.

4 CO_2-to-Dimethilcarbonate reaction over ZrO_2: liquid vs gas phase mechanism

4.1 Liquid phase reaction

In situ liquid phase IR experiments were conducted in multiple reflections ATR mode. All the experimental details are reported in materials and methods and in the Appendix F. Briefly, ZrO_2 catalyst was deposited over the crystal element (ZnSe) and pre-treated under cyclohexane at 70°C/60'. Background was collected after activation prior each measurement. As summarized in Figure 44, a methanol in cyclohexane solution (0.2 M) was mixed in a 1:1 ratio with CO_2-saturated cyclohexane and sent to the ZrO_2 catalyst at different temperatures (10,30,50 and 70°C).

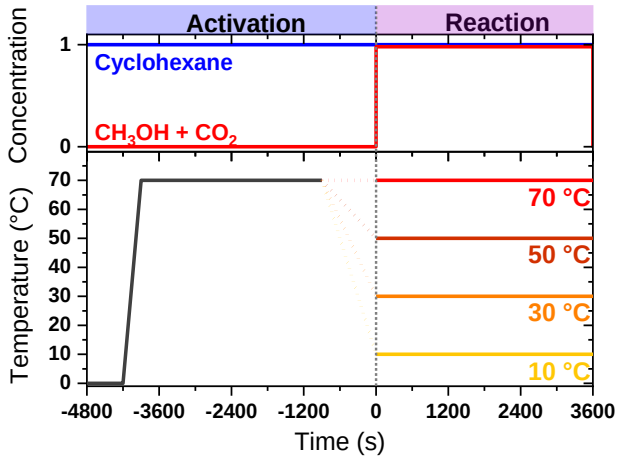

Figure 44 Schematic of the temperature/concentration profiles adopted in the in-situ ATR-IR experiments.

4.1.1 Adsorption of pure reagents/products

The *in situ* ATR-IR spectra related to the adsorption/desorption of methanol over ZrO_2 at 30 °C are presented in Figure 45a,b.

Three components were identified by Principal Component Analysis (PCA), leading to the spectral and concentration profiles in Figure 45c,d after MCR-ALS routine.

After a careful analysis of the spectra fingerprints and their time evolution we could identify component 1 as the spectrum of methanol solution, component 2 as weak physisorption of methanol with some surface sites of ZrO_2 and component 3 as linear and bridged methoxy groups coordinated to exposed Zr^{4+}.[1–3]

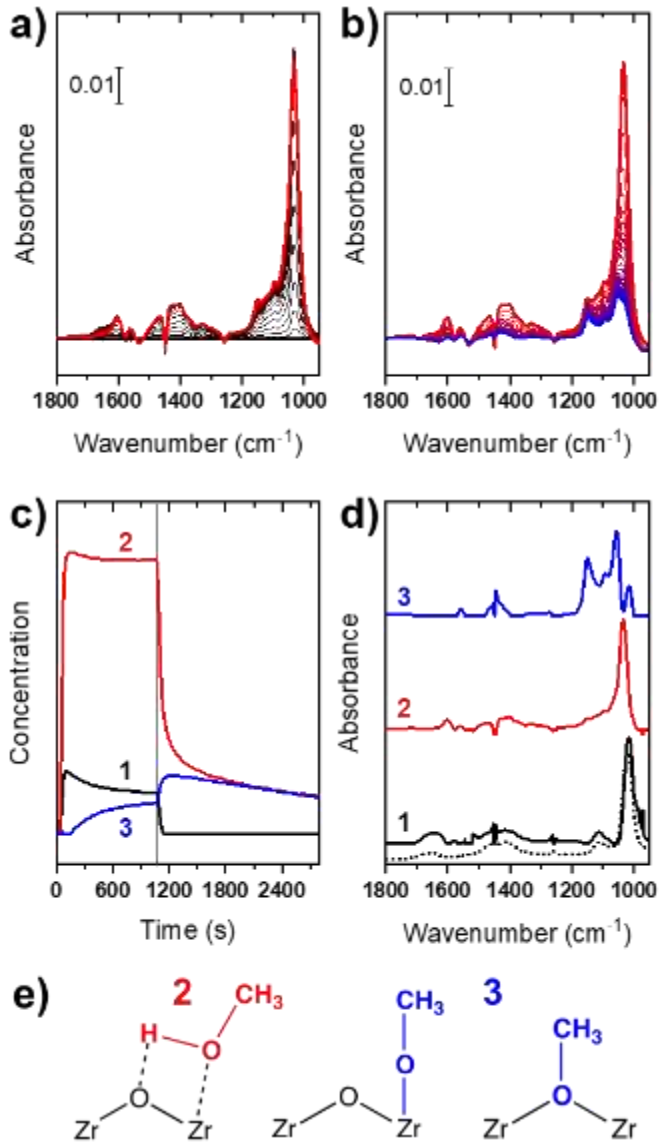

Figure 45 *In situ* ATR-IR spectra collected during a) adsorption of methanol on ZrO_2 (from a 0.2 M solution of methanol in cyclohexane, time evolution from black to red) at 30 °C and b) its desorption (by exposure to cyclohexane, time evolution from red to blue). c) Pure component spectra obtained by MCR-ALS (the ATR-IR spectrum of the bare 0.2 M solution of methanol in cyclohexane is shown as a dotted line). d) Corresponding concentration profiles as a function of time (the vertical grey

line represents the switch from the methanol solution to cyclohexane). e) Molecular structures of species associated to components 2 (weakly physisorbed methanol) and 3 (surface methoxide species); component 1 (liquid phase methanol) structure is omitted.

Considering adsorption of CO_2-saturated cyclohexane (Figure 46) we observed the formation of several signals in the carbonates vibration region. At maximum coverage (e.g. stable signal increase) four bands were distinguished at 1610, 1420, 1315 and 1040 cm^{-1} with an uncertainty on the second one being close to solvent phase poorly compensated signal. The same behavior is confirmed during desorption (Figure 46b), where the band at 1420 cm-1 showed a complete reversibility: this signal, typical of the bicarbonates-like ν(CO)sym mode. Conversely, the bands at 1610, 1315 and 1040 cm^{-1}, together with an additional component at 1530 cm -1 becoming evident at the lower CO_2 coverage, decreased during desorption and stabilized towards at the end of the experiment, finally yielding the pink spectrum labelled as 4 in Figure 46. These signals can be assigned to various families of carbonate-like species, most probably adsorbed mono- and bi-dentate carbonates. [4–7] A precise assignment of each band to a precise specific family of carbonates is not trivial due to the liquid phase environment, indeed as a much very heterogenous population of surfaces sites is expected as compared to gas-phase activated samples. Interestingly, bicarbonates fingerprint at 1225 cm^{-1} stemming from isolated δ(OH) was not observed, probably due to the liquid working conditions. However, we cannot exclude that the bicarbonates vibration might actually be related to another carbonate species different from gas phase adsorption.

MCR-ALS was attempted trying to isolate two spectral components. However, contrarily respect to gas-phase experiments, the procedure did not converge to meaningful spectra. In the following reactivity analysis we then considered the spectrum labelled 4 in Figure 46 as single component for surface carbonate.

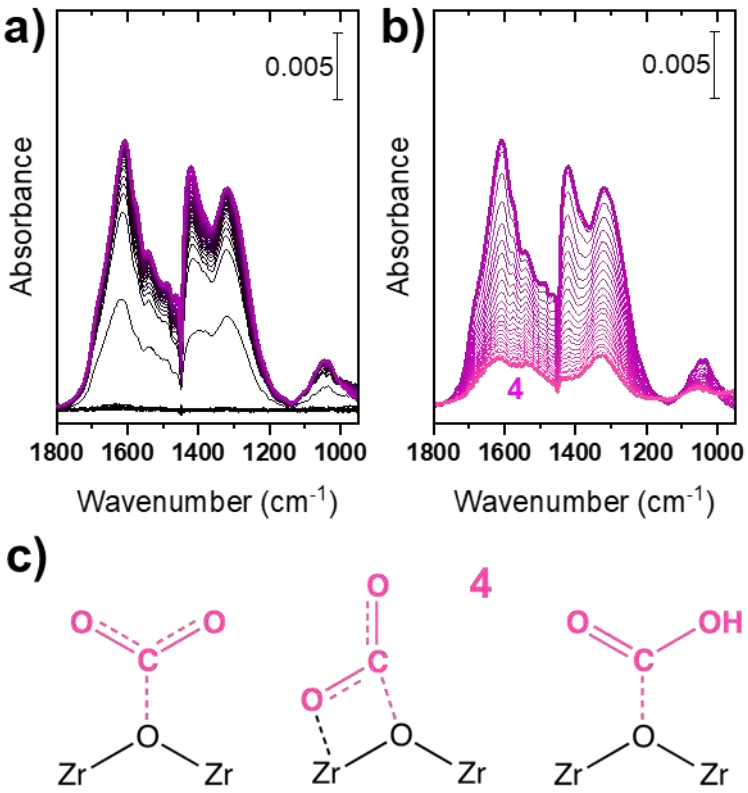

Figure 46 *In situ* ATR-IR spectra collected during a) adsorption of CO_2 on ZrO_2 (from CO_2-saturated cyclohexane, time evolution from black to violet) and b) desorption (cyclohexane, time evolution from violet to magenta) at 30 °C. c) Molecular structures of species associated to component 3 (from left to right: surface monodentate carbonate-like, bidentate carbonate-like and bicarbonate-like species).

Finally, the interaction of the reaction product (DMC) with ZrO_2 was studied, to evaluate the stability of the final product on the catalyst surface (Figure 47) We observed a reversible adsorption/desorption of DMC without presenting any decomposition to MMC. This could be related to either solvent-stabilization of DMC or to the non-completely active ZrO_2 surface due to the limited activation

temperature. Nevertheless, considering the reactivity experiments (see next session) showing some DMC production, we can discard the latter option.

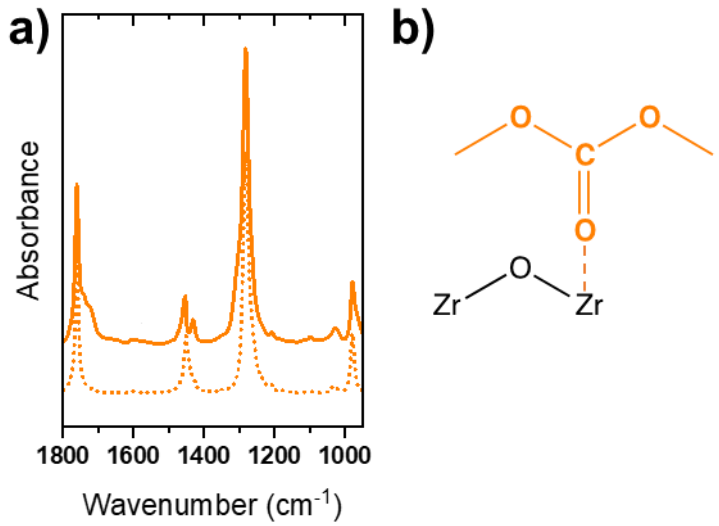

Figure 47 *In situ* ATR-IR spectrum of DMC adsorbed on ZrO_2 (from a 0.1 M solution of DMC in cyclohexane, after 30 min of contact, solid curve) at 30 °C. The spectrum of the bare 0.1 M solution of DMC in cyclohexane is reported for the sake of comparison (dotted line).

4.1.2 Reactivity of mixed methanol-CO_2

Figure 48 shows the *in situ* ATR-IR spectra collected during the simultaneous interaction of methanol and CO_2 on ZrO_2 at different temperatures.

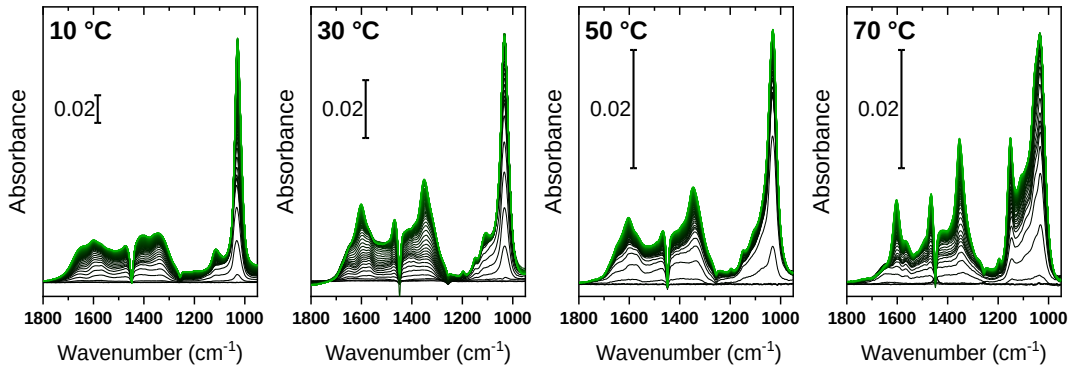

Figure 48 *In situ* ATR-IR spectra collected during the co-feeding of methanol and CO_2 (from a CO_2 saturated 0.1 M solution of methanol in cyclohexane) on ZrO_2 at different temperatures. Spectra were recorded for 1 h (time evolution from black to green).

A first qualitative analysis of the spectra shows as they are characterized by similar spectroscopic component but with lower intensity at higher temperature, in line with higher species desorption. Methanol and carbonates were well evident at each temperature whilst methoxides become more evident at higher temperatures, in line with lower methanol stability. The presence of triplet of bands at 1350, 1465 and 1600 cm^{-1} highlighted the formation of MMC as observed in the gas phase reaction. The dataset in Figure 48 were then analysed by MCR-ALS using methanol and carbonates as reference pure components. Since the same spectroscopic features were observed regardless of the reaction temperature, all data were merged in a single dataset and analyzed simultaneously, leading to the (re)optimized spectra of the pure components and their concentration profiles at each temperature are shown in Figure 49. An attempt to introduce the reaction product (DMC) as a sixth component was performed also in this case including 50 replicas of the spectrum of adsorbed DMC as shown in Figure 47. Nonetheless, inconsistent results were obtained on a chemical basis (not reported for sake of brevity).

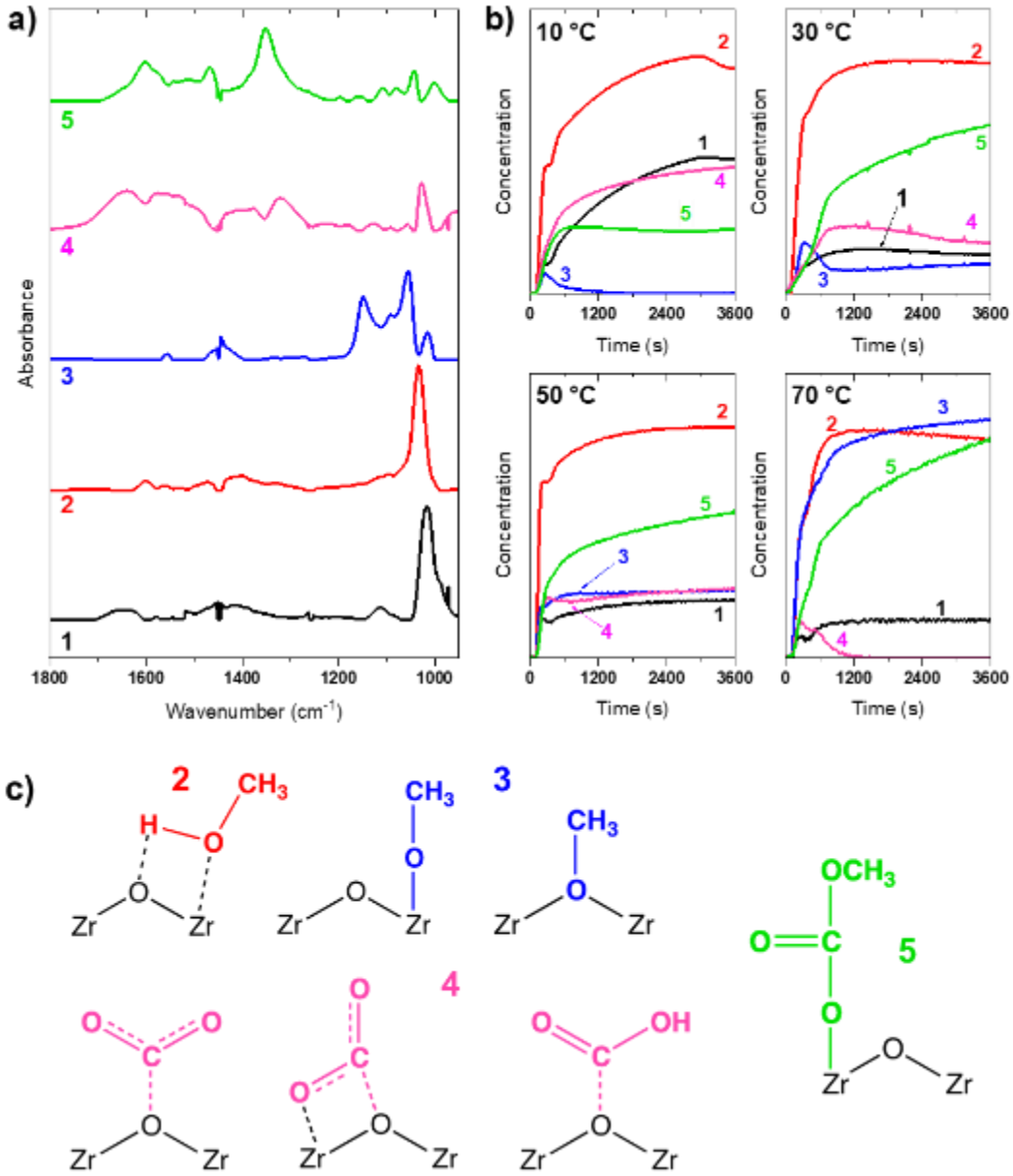

Figure 49 a) Spectra of pure components and b) their concentration profiles obtained from MCR-ALS for reactivity experiments conducted at different temperatures. c) Molecular structures of species associated to all components, including component **5** (i.e. surface MMC intermediate); component 1 (liquid phase methanol) structure is omitted.

Four of the five obtained spectra can be associated to those observed from the previous pure experiments: **1**, liquid phase methanol; **2**, molecular methanol adducts at ZrO_2 surface; **3**, surface methoxy groups and **4**, surface carbonates. Conversely, component **5** presents three main bands 1600, 1470 and 1350 cm^{-1}, ascribable to monomethyl carbonate (MMC) main vibrations.[7] Interestingly MMC is the CO_2-to-DMC reaction intermediate and its spectral component was completely extracted by the MCR-ALS routine.

The obtained results, summarized with the reaction mechanism in Figure 50, unveiled as ZrO_2 surface (**I**) is contacted with methanol and CO_2 solubilized in the working solvent, both surface carbonates and methoxide species are formed (**II**), and their respective ratio is strongly temperature dependent. At temperature $\leq$ 50°C, carbonates and methoxide species react together to form MMC (**III**), whilst at 70°C the reaction takes place between chemisorbed methoxide and gas-phase CO_2 (**III'**). The formation of MMC affects the equilibria determining the population of surface species (**IV**): in detail, the higher the temperature, the higher the concentration of MMC, at expenses of surface carbonates, that turns from the dominating surface specie at 10 °C to a closely nil concentration at 70 °C. Eventually, though not detected under the experimental conditions adopted in this study, the reaction of MMC with a second methanol molecule leads to the synthesis of DMC, that is desorbed from the surface as the final reaction product.

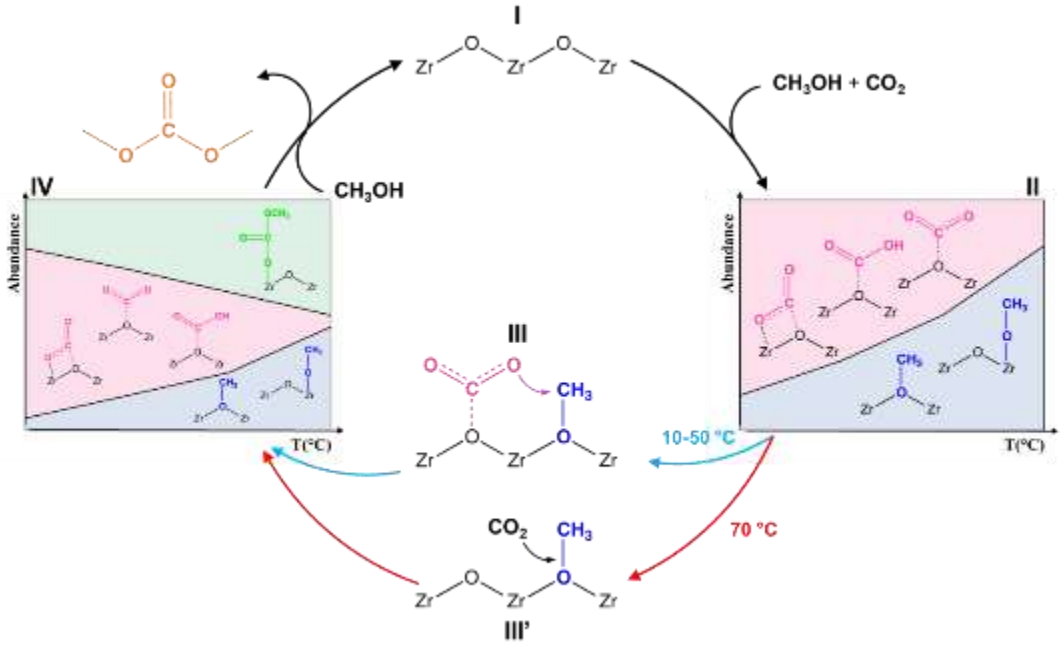

Figure 50 DMC formation reaction mechanism proposed for CO_2 and CH_3OH adsorbed over ZrO_2 at different temperatures. Abundance/Temperature diagrams (steps **II** and **IV**) are referred to the concentrations reported in Figure 49.

4.1.3 Liquid phase reaction: mechanism dependence with reaction temperature

The obtained results indicated as CO_2/CH_3OH activation strongly depend on temperature. Low temperatures (<30 °C), favoured the formation of stable carbonates by limiting methanol activation to its molecular physisorption, hence reducing monomethyl carbonate and preventing dimethyl carbonate (DMC) formation. On the contrary high temperatures (>50 °C), improved methanol dissociation thus forming reactive methoxide species at the expenses of the stability of carbonates, leading to an increase of MMC formation. Moreover, whilst the coexistence of carbonates and methoxide species at 10-50°C induces us to hypothesize the already known reaction mechanism involving an interaction between the two species, the abundance of methoxides at higher temperature together with the low levels of carbonates and the pronounced MMC formation suggested that the

interaction between methoxide and CO_2 could occur prior to carbonates formation. This observation may imply that DMC is produced through an alternative new reaction pathway involving a direct interaction between CO_2 and methoxide species preventing formation of stable carbonates and thus catalyst deactivation. It is noteworthy that for closing the catalytic cycle, DMC decomposition over ZrO_2 must be prevented prior to its desorption. This seems to be promoted by the liquid phase. Indeed, because, the liquid phase ATR-IR experiments demonstrated an increased stability of the DMC product at 50 and 70°C, allowing its further desorption at already 70°C. Conversely, gas phase experiments showed the rapid decomposition of DMC over ZrO2.

4.2 Gas phase reaction

4.2.1 ZrO_2 in-situ activation

All the measurements reported in the following sections were forerun by the activation procedure reported in Figure 51a aimed to prepare a clean catalyst surface. The activation consisted in the following four-step protocol : I) heating RT-150°C (5°C/min) under He (50 mL/min) (green line), II) heating 150-400°C under an He/O_2 mixture (50 mL/min 3:2 He:O_2) (red line), III) holding at 400°C for 60' under the same mixture (blue line) and IV) cooling to RT under He/O_2 and changing to pure He at 150°C. As reported in the spectra in Figure 51b, the employed protocol allowed to completely remove adsorbed water and organic pollutants however, without removing all the carbonates which would have required higher activation temperatures causing a potential (counterproductive) loss of surface area. More relevant is to observe as isolated hydroxyl groups are formed above 3500 cm^{-1} with the removal adsorbed water, indicated by the broad absorption band at ≈3300 cm^{-1}. After activation (blue line) two sharp hydroxyl bands are observed at 3677 and 3770 cm^{-1}, associated to tri-bridged and terminal Zr-OH groups. The bi-bridged hydroxyl groups are not observed, in line with the more abundant ZrO_2 monoclinic polymorph.[6] In the following results, the activated spectra has been subtracted from

the measured spectra in order to magnify the variations observed on the catalyst surface.

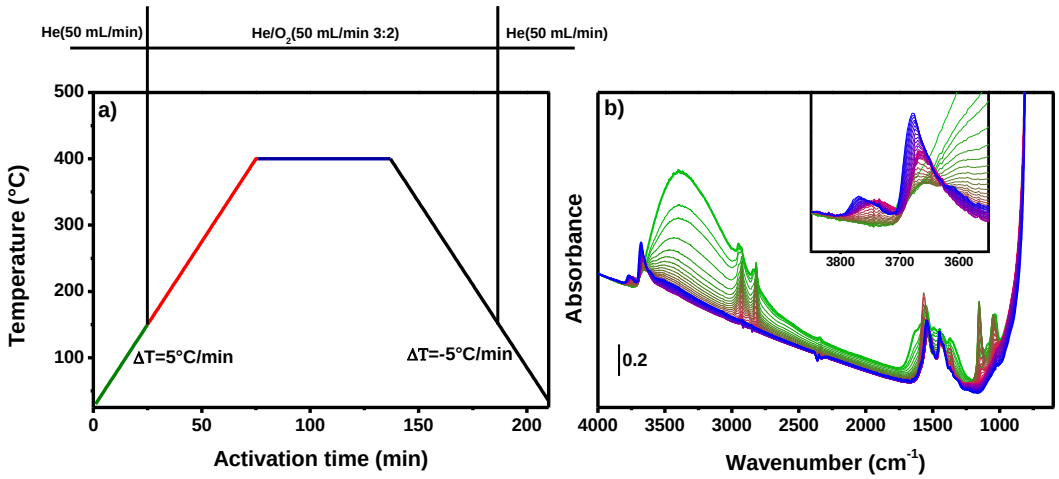

Figure 51 Activation procedure a) thermal/chemical ramp and b) spectra obtained during the activation. Colours in panel b) refers to the respective activation steps in panel a).

4.2.2 Methanol adsorption over ZrO_2 at 30°C

In-situ FT-IR spectra in Figure 52a shows a rapid adsorption of methanol over ZrO_2, forming physisorbed methanol, distinguishable from the P,Q and R branches in the 1100-1000 cm^{-1} range, followed by chemisorbed terminal methoxide at 1160 cm^{-1}. The spectra collected during desorption (Figure 52b) highlights as physisorbed methanol hides a methoxide component in the 1050-1100 cm^{-1} range (e.g. bi- or tri-bridged) which is stable during desorption. MCR-ALS analysis of the dataset showed the presence of the two spectral components reported in Figure 52c. The first component (Figure 52c black line) is comparable to methanol gas phase tabulated IR spectra (Met1). The second component (Figure 52c) presents two separated bands at 1161 and 1058 cm^{-1} identified as terminal and tri-bridged methoxide species, respectively (Met2). Even though the presence of these two components is well described in literature, the MCR-ALS analysis disclosed a clear view on their

adsorption kinetic behaviour. Indeed, the extracted concentration profiles reported in Figure 52d shows as the methanol physisorbed state rapidly covers ZrO_2 surface limiting the formation of reactive methoxide species. Contrarily, during desorption the methoxide species concentration increases parallel to a decrease of physisorbed component, suggesting as methanol concentration might play an important role in the methoxide accessibility.

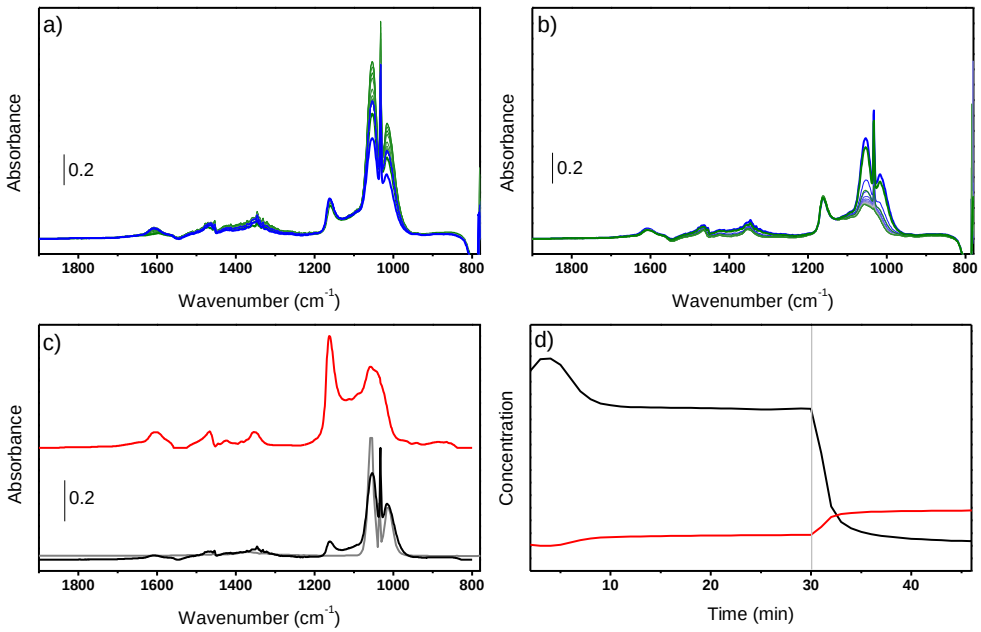

Figure 52 *In situ* FT-IR spectra collected during a) adsorption of methanol on ZrO_2 (15 mL/min He with 4% mol CH_3OH, time evolution from green to blue) at 30 °C and b) its desorption (by exposure to 15 mL/min of pure He, time evolution from blue to green). c) Pure component spectra obtained by MCR-ALS (FT-IR spectrum of pure CH_3OH taken from NIST webbook is shown with gray line). d) Corresponding concentration profiles as a function of time (the vertical gray line represents the switch from He/CH_3OH to He).

4.2.3 Carbon dioxide adsorption over ZrO_2 at 30°C and 150°C

FT-IR spectra in Figure 53a shows as CO_2 adsorption over ZrO_2 induces the formation of several bands between 1800 and 800 cm^{-1} which can all be associated to carbonates (CO_3) and bicarbonates (h-CO_3) species following the available literature. Nevertheless, since these species present convoluted broad bands, the CO_2 adsorption kinetic studies were often conducted following the evolution of a single isolated band. The MCR-ALS allowed to separate the two spectral components of carbonates and hydrogen-carbonates (h-CO_3) reported with pink and blue lines in Figure 53c. The assignment of h-CO_3 was relatively simple due to the presence of the characteristic δ(OH), $\nu(C{=}O)_{sym}$ and $\nu(C{=}O)_{asym}$ at 1221, 1425 and 1627 cm^{-1}, respectively, together with the consumption of Zr-OH groups parallel to the formation of h-CO_3 ν(OH) at 3617 cm^{-1} (Figure 53a inset). Contrarily the carbonates identification is less trivial. By considering the presence of two isolated bands at 1608 and 1330 cm^{-1}, we can assign them to a carbonate $\nu(OCO)_{asym}$ and $\nu(OCO)_{sym}$ vibrations. Moreover, their separation ($\Delta\nu \approx 280$ cm^{-1}) indicate the presence of either a bridged or tridentate carbonate. Since the specific identification of this carbonate will not be important for the further reaction analysis, we name this species t-CO_3 without referring to a specific carbonate but indicating a family of carbonates with coordination degree >2. Following the components concentration profiles in Figure 53d we observed as h-CO_3 species are rapidly adsorbed over ZrO_2 whilst t-CO_3 are not observed util the former species reached a plateau. When h-CO_3 reach its maximum concentration, their abundance started to decrease parallel to the increase of t-CO_3. This concentration kinetics shows as h-CO_3 formation is kinetically faster than t-CO_3 which on the contrary are thermodynamically more stable, in agreement with previous literature results. Indeed, during desorption, the t-CO_3 concentration continued to increase to the detriment of h-CO_3 decrease.

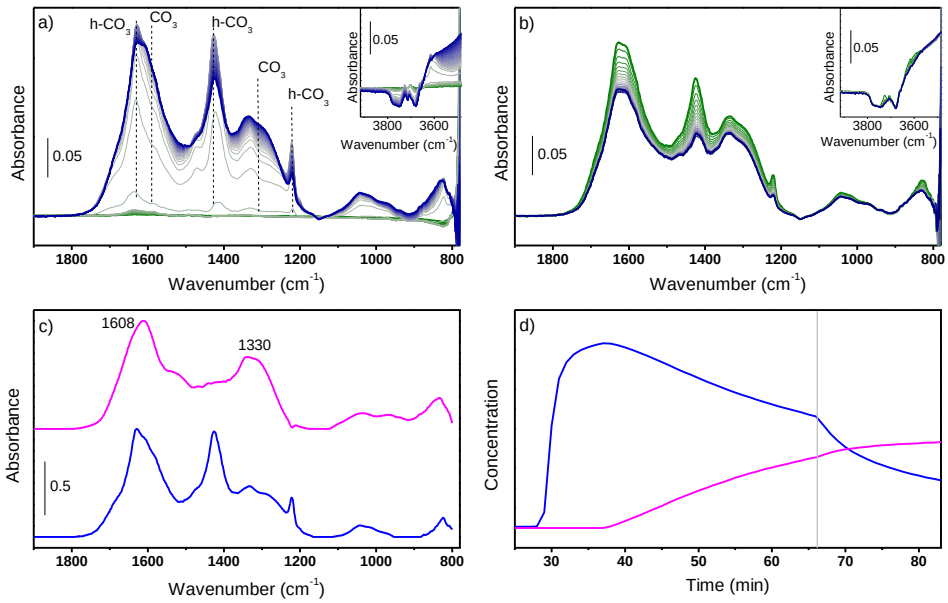

Figure 53 *In situ* FT-IR spectra collected during a) adsorption of CO_2 on ZrO_2 (50 mL/min He:CO_2 4:1, time evolution from green to blue) and b) desorption (50 mL/min He, time evolution from blue to green) at 30 °C. c) pure component spectra obtained by MCR-ALS. d) Corresponding concentration profiles as a function of time (the vertical gray line represents the switch from He/CO_2 to He).

This result suggests as CO_2 adsorption, hence its activation, might be promoted by hydroxyl groups through formation of h-CO_3 species which are then decomposed to more stable t-CO_3.

To improve the comprehension of CO_2 adsorption kinetic, the spectra in Figure 54a,b were collected at 150°C i.e., reaction-like temperature. The spectra measured during CO_2 adsorption in Figure 54a reported a higher degree of evolution and convolution complexity respect to those collected at 30°C (Figure 53a). h-CO_3 presence were identified from the fingerprint δ(OH) and $\nu(C{=}O)_{sym}$ vibrations at 1225 cm^{-1} and 1425 cm^{-1}, respectively. However, $\nu(C{=}O)_{asym}$ and ν(OH) were not identified, the former being too convoluted with other carbonates and the latter completely broadened from the high temperatures and covered by CO_2 overtones. 20 replicas of

the spectral components obtained at 30°C (Figure 53c) were then inserted at the end of the dataset for driving the SVD towards the probable components and parallelly optimizing the already found spectra. This approach led to find the three independent components reported in Figure 54c. Whilst the first component (Figure 54c blue line) is related to h-CO_3 species already found at 30°C, the other two components are associated to different carbonates. Among the two spectra we can recognize the already found t-CO_3 (pink line) whilst the second spectra (purple line) presented two components at 1536 and 1331 cm^{-1}. Considering the two bands as associated to $\nu(OCO)_{asym/sym}$ vibrations, their separation ($\Delta\nu \approx 205$ cm^{-1}) can be ascribed to a bidentate carbonate (b-CO_3). The high-temperature concentration profile unveiled as under reaction conditions h-CO_3 follows the same kinetic observed at 30°C whilst on the contrary b-CO_3 are formed more rapidly and are more stable than the former species. Moreover, t-CO_3 previously observed at 30°C are not observed during the whole adsorption/desorption cycle suggesting the higher stability of b-CO_3 at higher temperatures.

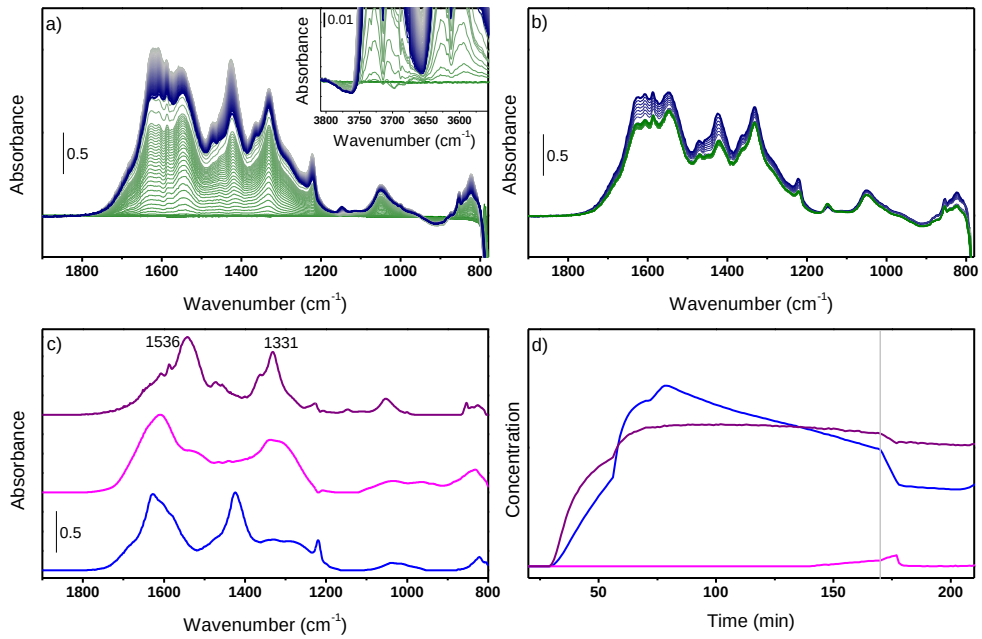

Figure 54 *In situ* FT-IR spectra collected during a) adsorption of CO_2 on ZrO_2 (50 mL/min He:CO_2 4:1, time evolution from green to blue) and b) desorption (50 mL/min He, time evolution from blue to green) at 150°C. c) pure component spectra obtained by MCR-ALS. d) Corresponding concentration profiles as a function of time (the vertical gray line represents the switch from He/CO_2 to He).

It seems unlikely that t-CO_3 component is formed only at high temperature whilst it is more probable that this species might be already formed at 30°C but being less intense and convoluted with b-CO_3. For this reason, the dataset collected at 30°C was re-analysed considering the three components optimized at 150°C as starting references, leading to the spectral components and concentration profiles in Figure 55b,c. No net variations were observed in the CO_3/h-CO_3 kinetics and spectral profile. Indeed, the concentration profiles (Figure 55c) show as t-CO_3 and b-CO_3 have similar kinetic highlighting, explaining why their spectra have never been deconvoluted. Through this deconvolution, the three t-CO_3, b-CO_3 and h-CO_3 components will be used in the further analysis.

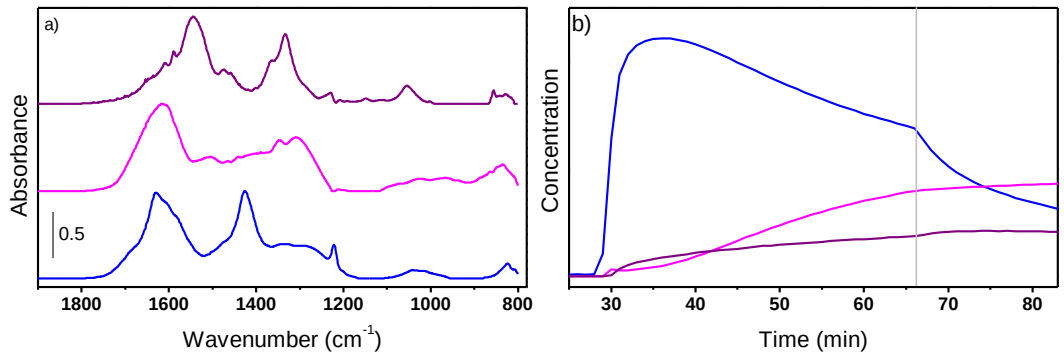

Figure 55 a) t-CO_3 spectra component extracted at 30°C (gray line) and weighted t-CO_3 (violet) and b-CO_3 (pink) extracted at 150°C. b) Pure component spectra obtained by MCR-ALS applied to the dataset in Figure 53a,b. d) Corresponding concentration profiles as a function of time (the vertical gray line represents the switch from He/CO_2 to He).

4.2.4 Dimethilcarbonate adsorption/desorption at room temperature

Due to its low vapor pressure, dimethilcarbonate (DMC) adsorption was investigated in static conditions following the same procedure described for RT-CO adsorption measurements i.e., a partial pressure of DMC was sent over a previously activated ZrO_2 pellet and spectra were collected during desorption of DMC partial pressure. Withing the formed wealth of bands in the spectra reported in Figure 56a we can distinguish DMC characteristic ν(C=O), $\delta(CH_3)_{asym}$ and $\nu(OCO)_{asym}$ vibrations at 1760, 1456 and 1291 cm^{-1}, respectively[8] and monomethylcarbonate $\nu(OCO)_{asym}$, $\delta(CH_3)_{asym}$ and $\nu(OCO)_{sym}$, vibrations at 1602, 1472 and 1361 cm^{-1}, respectively.[9] As already reported by Bell et al.[3] we observed a rapid DMC-to-MMC decomposition as soon as the former was adsorbed over ZrO_2 surface. Moreover, the formed MMC was stable over ZrO_2 since the main bands between 1300 and 1600 cm^{-1} were observed even after complete desorption of residual gas-phase components from the sample environment. Even if the obtained dataset contained a limited number of spectra (≈20), it presented a sufficient variance to apply MCR-ALS routine. Two

spectra components were extracted and to DMC and MMC, with a surprisingly clear deconvolution of their $\delta(CH_3)_{asym}$ vibration located at 1456 and 1472 cm^{-1}, respectively, which is usually not deconvoluted. On the contrary, MMC spectra presented extra features in the 1000-1200 cm^{-1} region, ascribable to methoxide vibrations. Indeed, DMC to MMC decomposition implies the formation of a methyl group which likely forms methoxide species. The use of methoxide spectra as references did not improve the deconvolution of those components (not reported for brevity). Nevertheless, as it will be discussed in the next session, the obtained MMC component was used as an initial guess further on optimized during the analysis of data collected under reaction conditions. The concentration profile reported in Figure 56c shows an increase of MMC concentration during DMC desorption, indicating a DMC-to-MMC decomposition. Nevertheless, the DMC desorption kinetic gave us access to clean reference spectra of DMC and MMC adsorbed on ZrO_2. More importantly, whilst DMC can be obtained as a stable specieMMC is unavailable as stable molecule according to its intermediate nature.

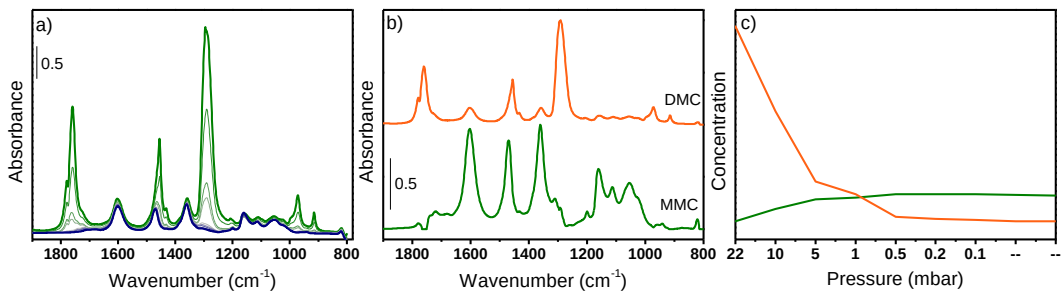

Figure 56 *Ex situ* FT-IR spectra collected during a) desorption of DMC on ZrO_2 (22 mbar, pressure evolution from green to blue) at RT. b) pure component spectra obtained by MCR-ALS. c) Corresponding concentration profiles as a function of pressure evolution.

4.2.5 Reactivity of CO_2/CH_3OH over ZrO_2

The spectra collected during adsorption of CO_2 carrying different CH_3OH over ZrO_2 are reported in Figure 57. Spectra were collected also during reactants desorption, but bare data are not reported for sake of brevity. This part of the datasets is however included in data analysis and discussed therein.

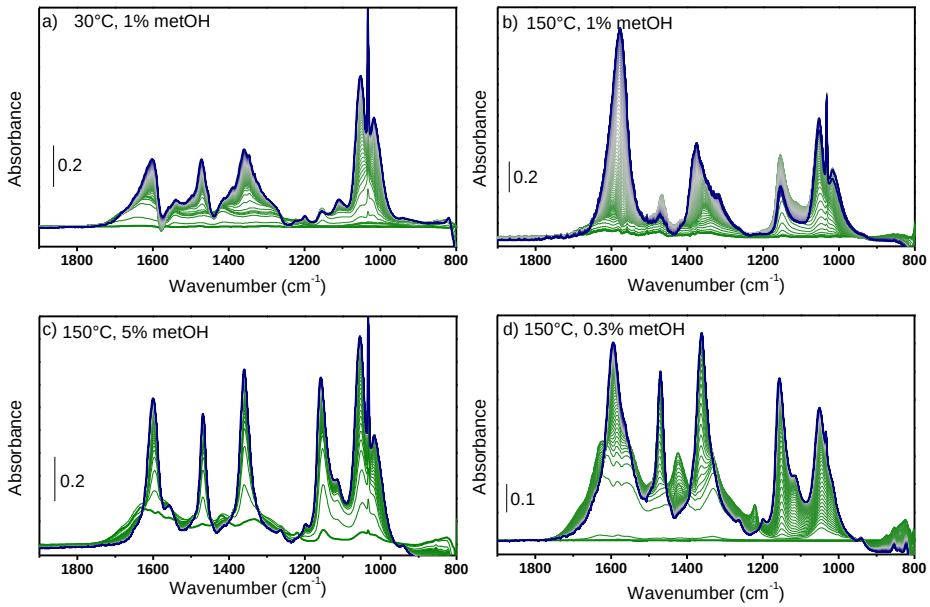

Figure 57 *In situ* FT-IR spectra collected during adsorption of CO_2/CH_3OH on ZrO_2 at a) 30°C and b,c,d) 150°C.

Since we observed as two different carbonates are observed at 30°C and 150°C, we first investigated their role in the reaction by investigating MMC and DMC formation at 30 and 150°C (Figure 57a,b). Afterwards, since liquid-phase experiments showed an important role of methoxide groups for CO_2 activation at higher temperatures, we have exploited the reaction with higher/lower methanol concentration in the reaction feed (Figure 57c,d). A first inspection of the recorded spectra unveiled the major presence of methanol and MMC fingerprints in the 1000-1100 cm^{-1} and 1300-1650 cm^{-1} ranges, reporting important differences when temperature and methanol concentrations are modified. For instance, by increasing

the temperature from 30°C to 150°C alters both MMC and methoxide groups behaviors. By fixing methanol concentration (1%), at higher temperatures methoxide formation is improved whilst MMC triplet presented a variation in relative intensity. Moreover, we noticed that varying methanol concentration led to: I) sharper MMC bands with higher methanol content (Figure 57c) or II) presence of extra bands parallel to almost absent gas phase methanol vibrations with lower methanol content (Figure 57d). Since the spectra presented similar components, the adsorption/desorption data were analyzed simultaneously by merging them one after another in a single dataset. From the recorded spectra, components from methanol, methoxide, bicarbonates, bi-/tri-bridged carbonates, methyl carbonate and dimethylcarbonate should be considered. For this reason, seven pure components were selected from the SVD analysis. However, since this high value of pure components might not lead to MCR-ALS converge, the seven spectral profiles reported in Figure 55b were repeated 50 times after the dataset. This approach allows to drive the SVD towards the reference components whilst parallelly also optimizes the pure component.

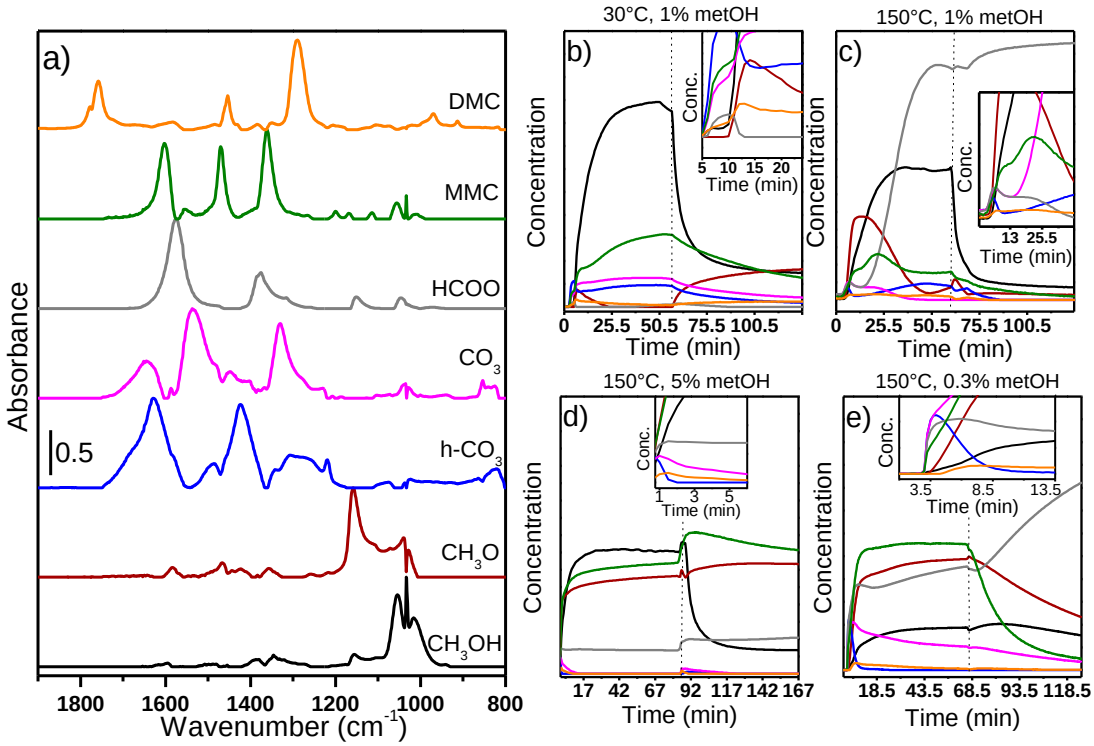

Figure 58 a) Spectra of pure components and b,c,d,e) their concentration profiles obtained from MCR-ALS for reactivity experiments conducted at a,b) different temperatures and c,d,e) methanol concentration.

Most of the (re)optimized spectral components reported in Figure 58a can be associated to those already observed during the pure experiments. Nevertheless, we observed the presence of a spectral component which resemble that derived from pure reagents adsorption (b-CO_3), however showing different bands position. Indeed, the spectra presented two sharp bands at 1375 and 1575 cm^{-1} which according to literature can be associate to formate (HCOO) $\nu(OCO)_{sym}$ and $\nu(OCO)_{asym}$.[10] Indeed, the presence of formate species was further confirmed from analysis of ν(CH) spectral region discussed in the next session. Contrarily the pink spectra, previously associated to carbonates, presented several bands which likely originated from the convolution of the t-CO_3 component with the pristine b-CO_3 one. Indeed, we can

identify two sharp bands at 1329 and 1534 cm^{-1} which for bands position and separation can be ascribed to $\nu(CO)_{sym/asym}$ of a bidentate carbonate. Two weaker central bands were also observed at 1401 and 1445 cm^{-1} and associated to the same vibration of a monodentate carbonate. Moreover, a broader band was observed at 1650 cm^{-1} which is likely related another bidentate carbonate ν(CO) vibration.[6] For sake of simplicity then identified this species as generic carbonates. The concentration profiles obtained in Figure 58 showed an important dependence of the formed species to the reaction temperature and even more to methanol concentration. Considering temperature as a variable, the first instants of reaction at 30°(Figure 58b inset) showed as h-CO_3 and CO_3 formation occurs before methoxide and remains constant through the whole adsorption. The concentration profile of the two components is very similar suggesting an important correlation of the two species during the reaction. Contrarily, at 150°C we clearly observed as whilst initially only CO_3 are formed and, after few minutes, they are decomposed to h-CO_3. At lower temperature methanol (black line) presence prevents methoxides (red line) formation, which are on the contrary quickly formed at higher temperatures. However, even at 150°C after few minutes methanol prevents methoxides production. Parallel to methoxide/methanol equilibrium, there is a clear competition between carbonates and methoxides as observed under liquid phase conditions (Figure 50), the former more stable at 30°C whilst the latter becoming more abundant at 150°C. Interestingly we observed a higher concentration of the reaction intermediate monomethyl carbonate (MMC, green line) at 30°C, where it presented an initial rapid growth followed by a slower growth after the first minutes of reaction, suggesting two different kinetic leading to MMC. Noteworthy, parallel to MMC initial rapid formation, a minor concentration increase was observed in DMC signal (orange line). At higher temperature the initial formation of MMC and (little) DMC, is followed by their concentration loss. Particularly, MMC decrease is accompanied with the rapid rise of formate component (not observed at 30°C) with parallel h-CO_3

formation and CH_3O concentration decrease. These results highlights as whilst at higher temperatures methanol desorption is favored improving methoxide formation, methoxide-loss and formats-rise have the same slope, suggesting a potential decomposition of the former to the latter, as already reported in literature to occur at 170°C.[11] Moreover, by comparing MMC and h-CO_3 slopes in the last reaction part, we observed as the presence of formates favors CO_3-to- h-CO_3 conversion causing a drop in MMC concentration. This is further confirmed by reactants desorption. At 30°C the lower methanol concentration allows the formation of extra methoxide species causing a slight increase of DMC concentration. On the contrary at 150°C formates showed high stability under desorption conditions, preventing an additional formation of all the other species.

By changing methanol concentration there is a particular relation between methanol and methoxide concentrations. With a CO_2:CH_3OH 5:1 ratio in the reaction feed we observed as the high accumulation of methanol does not completely prevent methoxides formation. A low concentration of formate species is observed, whilst MMC formation after a quick increase maintained a constant slight increase. Contrarily, as already discussed, by lowering the ratio to 25:1 (Figure 58d), CH_3O-species are formed before CH_3OH accumulation but are then decomposed to formate, which concentration rised preventing MMC formation. At minor methanol contents (83:1)(Figure 58e) its concentration grows less than the other components. The little surface accumulation of liquid methanol allows a rapid growth of methoxide. However, contrarily to the 25:1 experiment (Figure 58c), an methoxide concentration higher than methanol induces and equilibrium with the formed formate, preventing methoxide decomposition and maintaining MMC concentration. It is well observable as CO_3 formed at the beginning of adsorption are constantly consumed parallelly to formate growth, confirming the latter higher stability respect to the former. Interestingly during desorption, we can notice as at low methanol content methoxide are decomposed to formate, which concentration increases. By increasing methanol

concentrate during desorption the formate are stabilized (25:1 case) and eventually in minor concentration (5:1 case), allowing further methoxide formation and MMC increase.

To confirm formate presence, we qualitative analysed the ν(CH) spectral region of the collected spectra reported in Figure 59. Even though the spectra showed the presence of several convoluted bands, we could distinguish five bands ascribable to $\nu(CH)_{sym}$ and $\nu(CH)_{asym}$ of methoxide (2818 and 2923 cm^{-1}), methanol (2843 and 2949 cm^{-1}) and formate (2865 cm^{-1}), where the former component is more intense at 150°C/1% CH_3OH conditions and its intensity grows parallelly to methoxide vibration decrease. Both the observation are in line with the previous findings indicating formate production caused by methoxide decomposition.

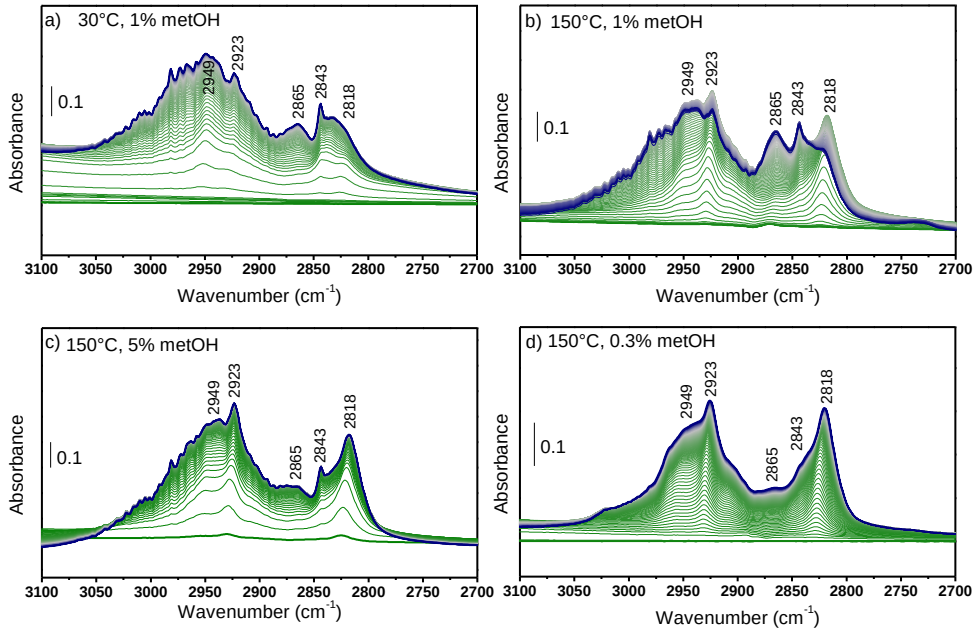

Figure 59 Detail of *in situ* FT-IR ν(CH) region spectra collected during adsorption of CO_2/CH_3OH on ZrO_2 at a) 30°C and b,c,d) 150°C. Reaction feed was set to 30 mL/min He with 25% CO_2 and X% CH_3OH, where X was a,b)1%, c)5% and d)0.3%. Time evolution goes from green to blue line.

4.2.6 Gas phase reaction: the role of methanol concentration

The study conducted in gas phase allowed us to work under temperature conditions closure to the reaction one (150°C). The results measured at 30°C and 150°C with the same methanol concentration (1%) indicated the same reaction mechanism already reported in literature and describe for the liquid phase reaction at T<50°C where carbonates and methoxide species react together to form MMC (step III Figure 60). Nevertheless, at high temperature in gas phase we observed a drop in MMC formation after ≈20 minutes caused by methoxide decomposition to formate. A complex interplay is observed between methoxide formation/decomposition and methanol concentration. Lower methanol concentrations improved an initial methoxide formation however, causing their decomposition to formate after few minutes. The decomposition process will be object of a future study however, we can hypothesize as it is caused by the abundant methoxide and water species, both products of methanol dissociation over Zr-OH, reacting together as reported below.

$$CH_3O\text{-}Zr + H_2O \rightarrow HCOO\text{-}Zr + H_2$$

Formate production reaches is maximum with 1% of methanol parallel to a complete detriment of MMC formation, confirming as the former species is not reactive towards the latter. By increasing methanol concentration to 5% we noticed an important improvement towards methoxide stabilization inducing a direct increase of MMC formation. It is noteworthy as under liquid phase reaction formate were not observed indicating as the liquid state (i.e., maximum methanol concentration) completely prevents methanol decomposition. At highest methanol contents, MMC formation was observed even though carbonates were not present, highlighting as MMC might be formed through a direct interaction between methoxide and gas phase CO_2 (step III' Figure 60), as hypothesized to occur for liquid phase reaction at 70°C.

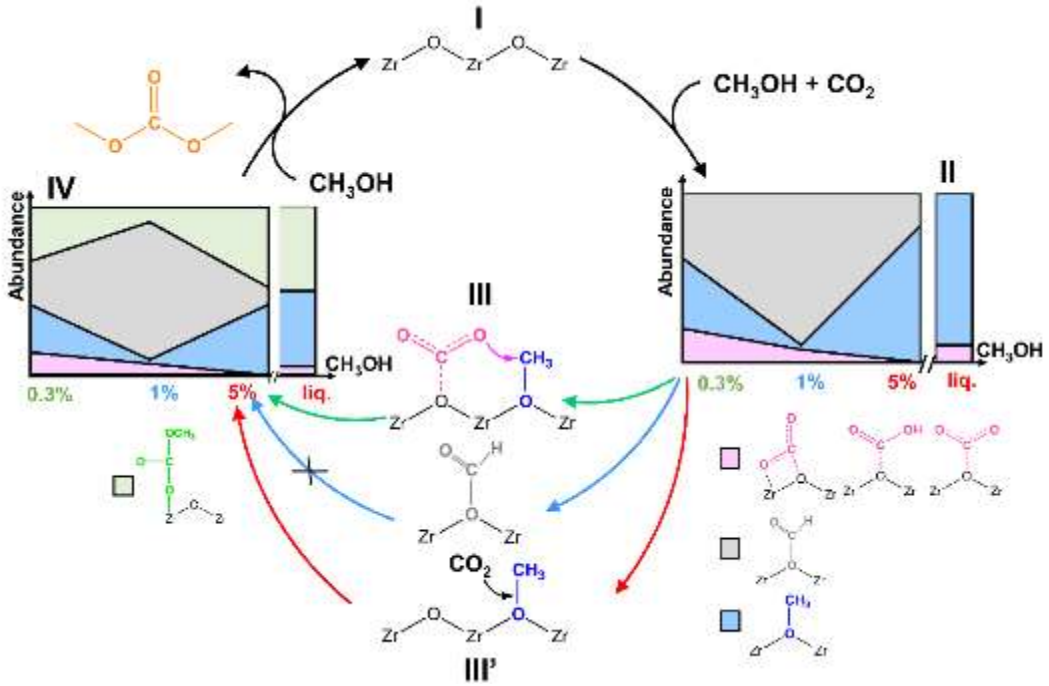

Figure 60 Proposed reaction mechanism for DMC formation at different methanol concentrations. Abundance/CH_3OH diagrams (steps **II** and **IV**) are referred to the concentrations (150°C) reported in Figure 58. Liquid (liq.) concentration are referred to the data collected at 70°C reported in Figure 49.

4.3 Conclusions

Within this study we successfully showed as MCR-ALS can be applied to deconvolute several spectra component formed under reaction conditions. Even though this approach cannot be considered as quantitative since absorption coefficients are not considered, the concentration profiles gave a valuable information of the involved species behaviour. Performing adsorption/desorption experiment of pure species prior the full reaction was employed to extract reference spectra, allowing to extract spectra component of reaction intermediate (i.e., MMC), otherwise inaccessible. Two mechanisms were identified indicating either a reaction between carbonates and methoxide species or a direct interaction between methoxide and gas phase CO_2. Higher temperatures shift the reaction towards the latter

mechanism. However, the total methanol concentration in the feed is observed a fundamental parameter to prevent methoxide decomposition to non-reactive formate.

4.4 CeO_2 Frustrated Lewis Pair improving CO_2 and CH_3OH conversion to Monomethylcarbonate

4.4.1 CeO_2 preparation and basic characterization

Frustrated Lewis Pair (FLP) formation over CeO_2 depends on the Ce^{3+} and oxygen vacancies surface concentration. Microwave assisted sol-gel synthesis was employed to prepare a crystalline CeO_2 sample with rough surface. The as prepared sample was further calcined at 100°C and named MW(100). To verify the role of microwave-induced defectivity, the same sample was calcined at 650°C (MW(650)) and at the same time a last sample was prepared by conventional sol-gel synthesis and calcined at 650°C (conv(650)). Powder X-Ray Diffraction (PXRD) pattern of the three samples presented Bragg peaks associated with the FCC CeO_2 phase. MW(650) presented an higher crystallite size and SSA respect to MW(100), indicating as the higher calcination temperature caused crystallites sintering whilst parallelly improving N_2 surface adsorption properties. Contrarily conv(650) presented bigger crystallites with lower surface area. Since FLP formation implies the Ce^{3+}/V_O clustering, surface-to-bulk oxygen mobility, a well-known phenomenon occurring in CeO_2 at mid-high temperatures, should be avoided. For this reason, for all the spectroscopic characterization MW(100) was further reduced at 150°C under H_2, to induce Ce^{3+} and V_O without inducing oxygen mobility.

Samples bulk defectivity was characterized with Raman spectroscopy exploiting the availability of two exiting lasers sources (514 and 325 nm). In particular, 514 nm source allows a more precise F_{2g} mode identification (position and FWHM) while the latter, being in resonance conditions, enhances defects signals. Conv(650) presented a single sharp band at 464 cm^{-1} associated to the Ce-O F_{2g} mode, confirming a pure/not-defective CeO_2 catalyst (Figure 61a). The band Full Width Half Maximum (FMHM) increased and its position redshifted in order MW(650) < MW(100) < MW(100)-red, in line with smaller and more defective particles with higher Ce^{3+}/V_O concentration. Moreover, I_{590}/I_{F2g} ratio, often reported as a defect-

meter and more clearly observed with UV-Raman spectra (Figure 61b), qualitatively showed as MW(100) the highest surface defectivity i.e., defectivity is reduced from calcination whilst conventional synthesis did not form any defects on the catalyst surface. Moreover, resonant-Raman (Figure 61b) clearly distinguished a band at 489 cm^{-1}, previously associated to Ce^{3+} in the second coordination sphere of an oxygen vacancy.[12] A quantitative evaluation of I_{590}/I_{F2g} and I_{489}/I_{F2g} is not possible due to the convoluted presence of quartz signals from the Raman cell, confirmed from the band at 808 cm^{-1}.

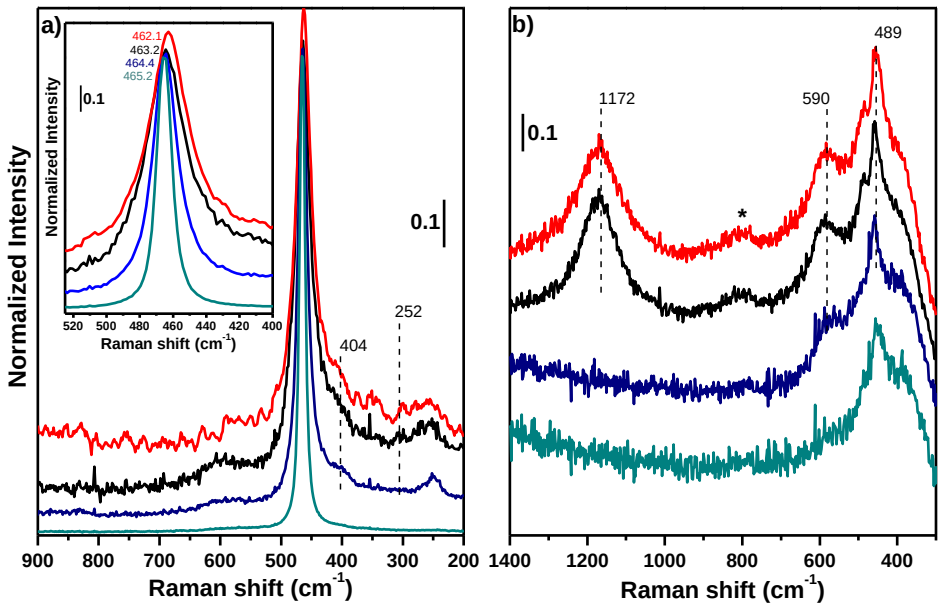

Figure 61 Stacked Raman spectra of conv(650) (dark cyan line), MW(650) (blue line), MW(100) (black line) and MW(100)-red (red line) measured with a) 514 nm and b) 325 nm laser. Detail of CeO_2. F_{2g} bands for the four catalysts and their Raman Shift position are reported in the inset in panel a. Quartz signal is showed with *.

To selectively quantify Ce^{3+} formed at the catalyst surface, XPS spectra were collected after CeO_2 oxidation and reduction at the same temperatures exploited in the previous measurements. After a careful evaluation of Ce^{3+} induced by beam

damage (see Materials and methods), we observed as 14% of Ce^{3+} was already present on MW(100) (Figure 62a) whilst Ce^{3+} increased to 35% after H_2 treatment (Figure 62c). Even if Ce^{3+}/Ce^{4+} ratio has been often evaluated also from O 1s spectra, other surface species observed by IR spectroscopy might contribute to this spectral region. We then described O 1s region considering two contributions: a first one at 529.7 eV related to lattice CeO_2 oxygen (O_L) and a second one at higher energy (≈531 eV), namely O^{β}, potentially originated by a complex convolution of all the other species i.e., $OH(Ce^{4+})$, $OH(Ce^{3+})$, $CO_3^{=}$ and O close to V_O (O_{Vo}).[13–15] Since *ex situ* IR spectra collected under the same activation conditions did not show an important variation in carbonates and hydroxyl species, we can associate the increase of O^{β} in MW(100)-red O1s spectra (Figure 62b) to a variation of oxygen electronic configuration i.e., an increase of surroundings V_O.

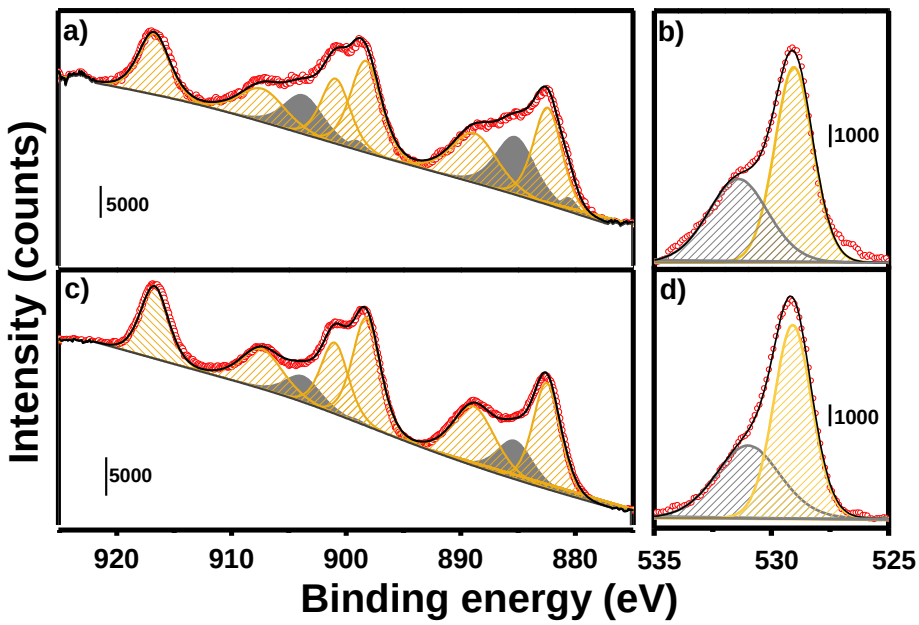

Figure 62 *Ex situ* a,c) Ce (3d) and b,d) O (1S) XPS experimental spectra (red circles) and best fit (black line) of c,d) MW(100) and a,b)MW(100)-red. Ce^{4+}/O_L and Ce^{3+}/O^{β} components are reported with yellow and grey bands.

Surface CO chemisorption at nominal 100 K was to qualitatively evaluate surface Ce^{3+} abundance. Briefly, bands at $\nu > 2147$ cm^{-1} are related to Ce^{4+} sites following the rule of thumb "the higher the wavenumber the more uncoordinated the site is". This simple principle, well verified in literature, confirmed as the surface defectivity decreases in order MW(100)<MW(650)<conv(650). Moreover, in the first catalysts bands at $\nu < 2147$ cm^{-1} becomes visible. Whilst the one around 2101 cm^{-1} observed in all the sample and associated to ^{13}CO, the band at 2131cm^{-1} is associated to CO-Ce^{3+} interaction.[16] Notably, in MW(100)-red, the Ce^{4+} bands is shifted to lower energies whilst the Ce^{3+} bands intensity increases, highlighting as the most defective Ce^{4+} sites are reduced to Ce^{3+}.

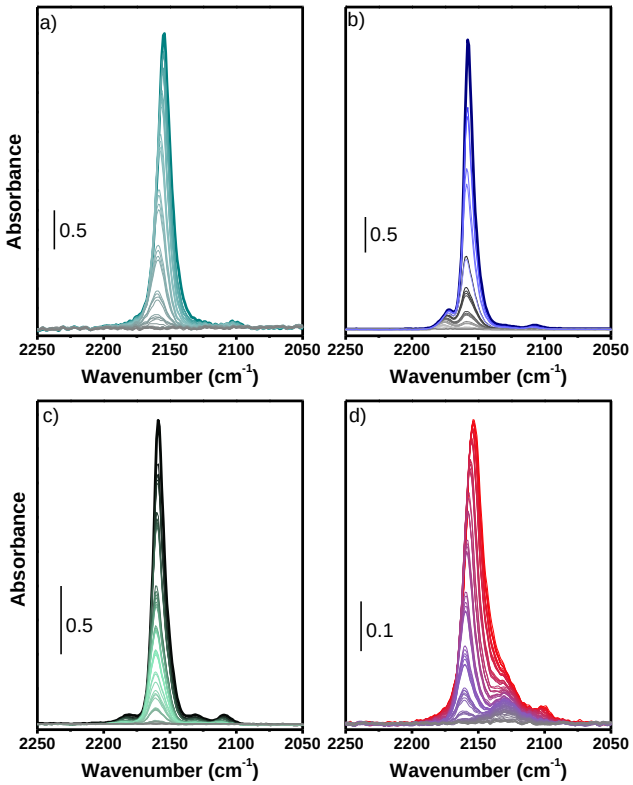

Figure 63 Difference FTIR spectra of CO increasing partial pressure (from gray to coloured line) at LNT over a) conv(650), b) MW(650), c) MW(100) and d) MW(100)-red.

4.4.2 CH_3OH and CO_2 activation over Ce^{3+}/V_O and FLP

Methanol and carbon dioxide absorption were employed to probe surface oxygen vacancies and to identify formed carbonates. After methanol adsorption (Figure 66a) over the CeO_2 samples, besides the formation of usual methoxide species (terminal, bi-bridged and tri-bridged), we observed a band at 1073 cm^{-1} over MW(100)-red sample (Figure 66a red line), associated to a methoxide group bridging two Ce^{3+} atom without interacting with the V_O (b'-OCH_3).[17] Indeed, CeO_2 reduction process is well known to cause a blueshift of b-OCH_3 ν(CO) due to different charge delocalization over the methoxide oxygen atom i.e., Ce^{3+} polarizes and delocalizes less than Ce^{4+}, causing an increase of C-O bond order and shifting ν(CO) to higher energies.[18] Moreover, MW(100)-red presented m-OCH_3/b-OCH_3 intensity ratio lower than the ideal one (2:1), contrarily respected from the other catalysts, unveiling a preferential reduction of (100) and (110) faces where b-OCH_3 are more stable, giving then access to FLP formation.[17] II) Ce^{3+} electronic transition at 2127 cm^{-1} was not modified by methanol adsorption suggesting (Figure 64a), as confirmed by XPS (vide infra), that b'-OCH_3 did not modify cerium oxidation state.

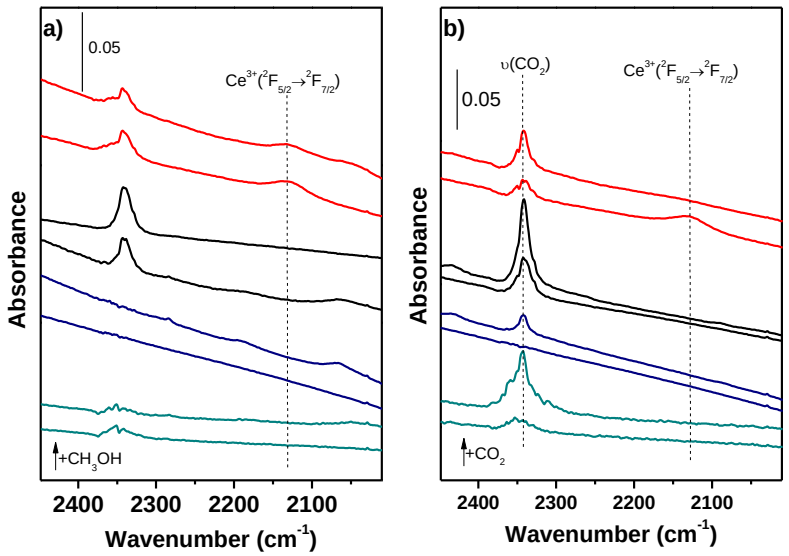

Figure 64 FT-IR spectra prior (lower) and after (higher) adsorption of a) CH_3OH (3 mbar) and b) CO_2 (100 mbar) at RT over conv(650) (dark cyan line), MW(650) (blue line), MW(100) (black line) and MW(100)-red (red line) catalysts.

To finely assign mono/bidentate/bridged carbonates/bicarbonates vibrations, we performed $^{13}CO_2$ adsorption (Figure 65) and compared the relative frequency shift ($\Delta^{13}C$) with recent literature.[19] Following Vaysillov and coworkers.[19] carbonates nomenclature, based on the number of cerium ions bounding each carbonates oxygen atom,$^{13}CO_2$ results (Figure 65) indicated as the formed carbonates can be restricted to four bidentate species sketched in Figure 66 for clarity.

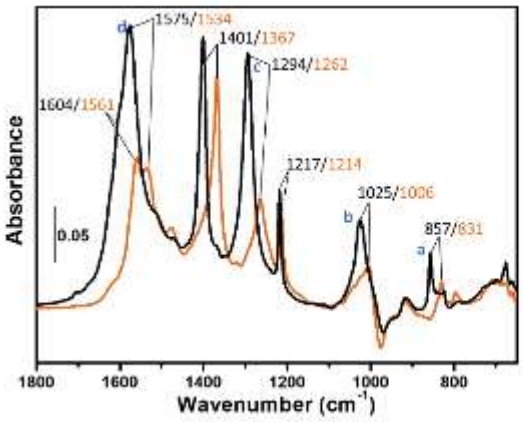

Band	0.13	1.21	1.21'	1.2.1	1.2.1'
a	26	26	24	24	24
b	19	5	1	5	7
c	32	29	34	29	32
d	41	41	42	43	42

Figure 65 FTIR spectra of MW(100) after absorption of CO_2 (black line) and $^{13}CO_2$ (orange line). Main identified vibrations are indicated. Spectra are reported as difference by substracting the activated spectra. $\Delta^{13}C$ shifts of carbonates vibrations are reported in the table together with the relative shift of simulated carbonates from Vaysillov and coworkers.[19]

Noteworthy, we observed as on MW(100)-red catalysts CO_2 caused a I) consumption of Ce^{3+} electronic transition at 2127 cm^{-1} suggesting a Ce^{3+}/CO_2 electronic interaction (Figure 64b) and II) a higher carbonates-to-bicarbonates ratio respect to the other catalysts (Figure 66b) indicating, as rationalised hereafter, an increase of 1.21' carbonate associated to the higher Ce^{3+}/V_O content.

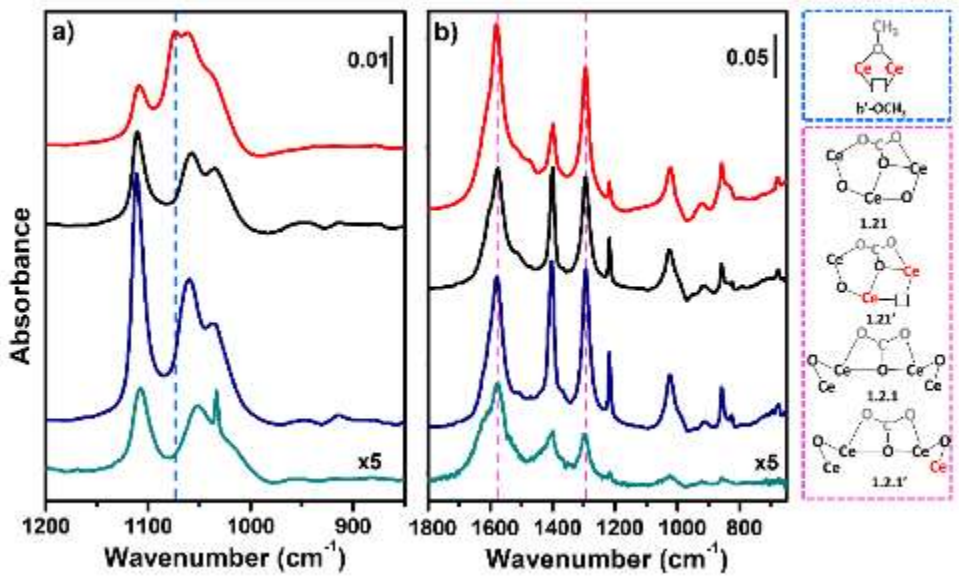

Figure 66 Difference FTIR spectra of a) 3 mbar methanol and b) 100 mbar CO_2 RT adsorption over conv(650) (dark cyan line), MW(650) (blue line), MW(100) (black line) and MW(100)-red (red line) catalysts. Sketched methoxide and carbonates species formed over CeO_2 are showed in blue and purple panels, respectively. CH_3OH and CO_2 atoms are showed in grey, Ce^{3+} in red and oxygen vacancy with black square. Carbonates nomenclature based on the number of cerium ions bounding each carbonates oxygen atom was taken from Vayssilov et al.[19] while apostrophe is here used to indicate carbonates considering Ce^{+3} presence. The spectrum of the material prior interaction with CH_3OH/CO_2 has been subtracted.

The hypothesized bidentate carbonate formed over a FLP should imply a sort of Ce^{3+}-to-CO_2 charge transfer. UV-Vis (Figure 67a) and XPS spectra of MW(100)-red (Figure 69) were measured before and after interaction with CO_2. We observed a decrease of: I) Ce^{3+}/Ce^{4+} CT (Figure 67a) and II) Ce^{3+}(3d) peaks (Figure 69b,e) after CO_2 adsorption at RT and 30°C/150°C, respectively. In addition, O1s XPS peaks (

Figure 67 b,c) showed as O_L and O^{β} signals did not undergo a considerable variation after CO_2 adsorption, suggesting as the latter did not modify O electronic

reconfiguration occurred after reduction (vide supra), signifying as the formed carbonate did not fill the V_O, as instead previously hypothesized.[20]

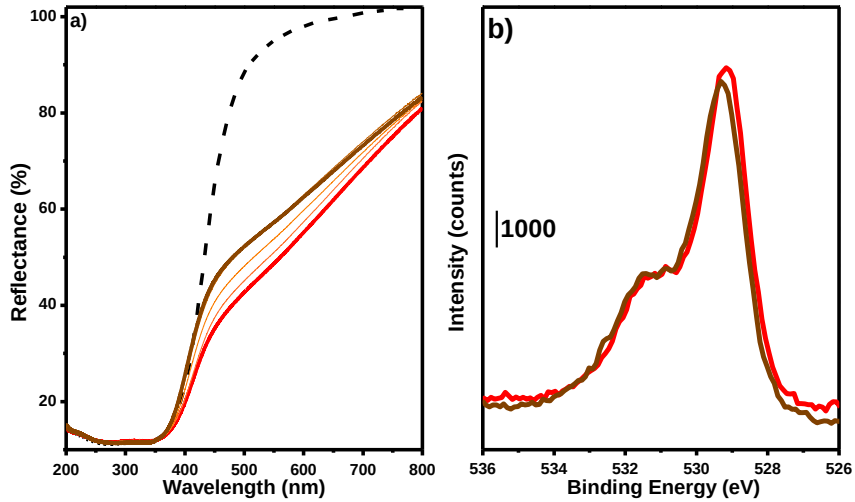

Figure 67 a) *Ex situ* UV-Vis spectra of MW(100)-red prior (red line) and after interaction with CO_2 atmosphere. The effect of increasing CO_2 partial pressure from 25 to 100 mbar is illustrated by the spectra from red to brown line. MW(100) is showed with dashed black line. b, c) XPS O 1S experimental spectra (red line), best fit curve (dashed black line), O_L (yellow curve), O^{β} (grey curve) and linear background (grey line) of MW(100)-red b) before and c) after interaction with 100 mbar of CO_2.

To verify the effective CO_2 and CH_3OH activation over FLP we exploited their reactivity to form monomethylcarbonate (MMC), the fundamental intermediate of dimethilcarbonate (DMC), by studying CO_2/CH_3OH chemical interaction with CeO_2 surface previously saturated with methoxide (CH_3O-CeO_2) or carbonates (CO_3-CeO_2) species, respectively. The presence of Ce^{3+} alone should indeed reduce MMC formation [21,22] whilst clustered Ce^{3+}/V_O forming a FLP should improve CO_2 reactivity. FTIR spectra in Figure 68a showed as CH_3OH adsorption over CO_3-CeO_2 caused a consumption of b-CO_3 and hCO_3 species in all the samples forming methoxide and

MMC species however without a considerable difference between the formed MMC bands intensity indicated with dashed lines in Figure 68a. Moreover, b'-OCH_3 have not been observed in MW(100)-red, suggesting that Ce^{3+} was already involved in the 1.21' carbonate formation.

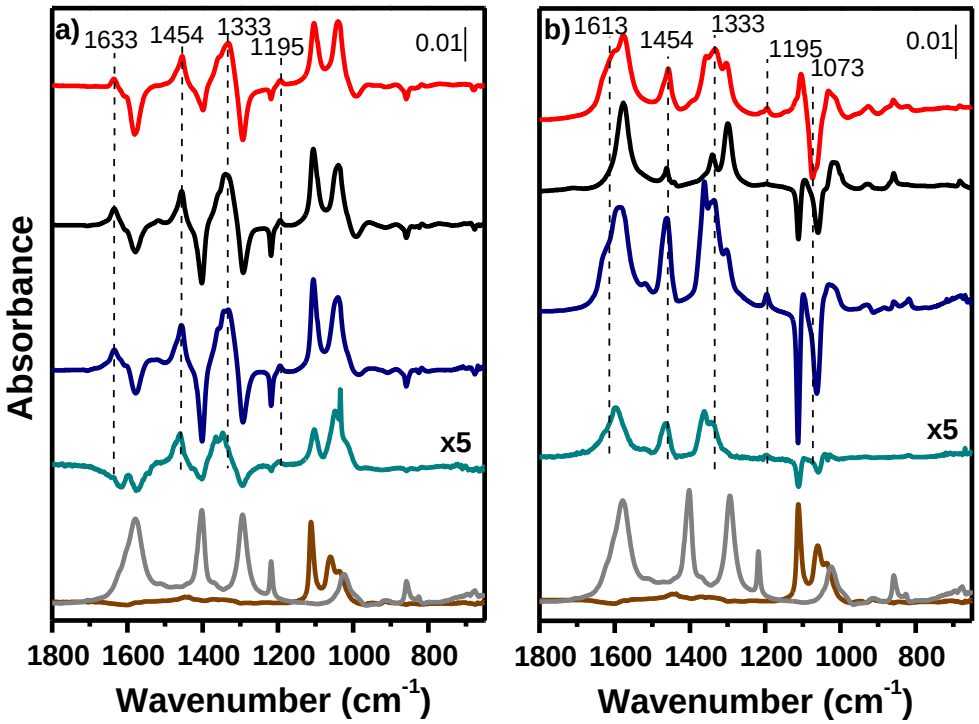

Figure 68 Difference FTIR spectra of conv(650) (light blue line), MW(650) (blue line), MW(100) (dark line) and MW(100)-red (red line) after a) CH_3OH (3 mbar) adsorption at RT over CeO_2 samples, previously reacted with CO_2 (100 mbar) at RT. Spectra of each CO_3-CeO_2 component have been substracted. b) CO_2 adsorption (100 mbar) at RT over catalysts previously reacted with 3 mbar of CH_3OH (CH_3O-CeO_2) at RT. Spectra of each CH_3O-CeO_2 component have been substracted. CH_3O-MW(650) (grey line) and CO_3-MW(650) (brown line) component are showed for clarity.

XPS spectra of CH_3OH adsorption over CO_3-MW(100)-red exploited at 30°C and 150°C (reaction temperature) in Figure 69°, showed a first decrease of Ce^{3+} bands after CO_2 adsorption followed by an increase upon interaction with CH_3OH. Whilst the former was described above and associated to Ce^{3+} partial reoxidation due to 1.21' carbonates formation, the latter can be associated either to methanol-induced Ce^{4+} reduction or MW(100) beam damage.[23–25]

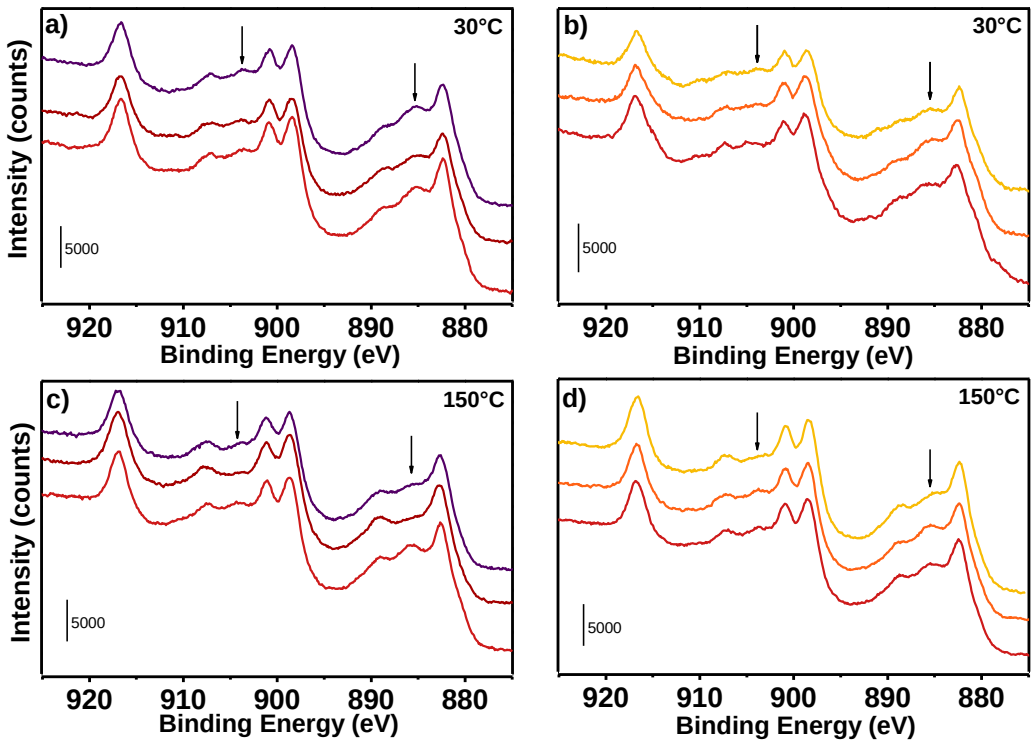

Figure 69 *Ex situ* Ce 3d XPS experimental spectra measured at 30°C and 150°C of MW(100)-red catalyst (red line) after : a,c) a first interaction with CO_2 (dark red line) followed by CH_3OH (purple line) or c,d) a first interaction with CH_3OH (orange line) followed by CO_2 (yellow line). Ce^{3+} most intense peaks are indicated with arrows.

Whilst the formed carbonates did not show particular differences in the reactivity with methanol, the reverse interaction i.e., CO_2 interacting with a surface with methoxide species, showed a different behaviour. Upon CO_2 adsorption over CH_3O-

CeO_2 samples (Figure 68b) we observed as methoxide species were consumed to form b-CO_3 and MMC. MMC was well formed over Ce^{3+}-free catalysts i.e., conv(650) and MW(650) whilst it was barely observed on MW(100) confirming as low Ce^{3+} content (≈14%) poisoned the reaction.[21–25] Following these results MW(100)-red with Ce^{3+}>30% should present an even lower MMC formation. Conversely we observed a qualitative higher concentration of MMC formed respect to MW(100) (Figure 68b) together with consumption of Ce^{+3} $^2F_{5/2}\rightarrow{}^2F_{7/2}$ electronic transition (not shown for brevity) and b'-OCH_3 species, both indirectly suggesting Ce^{3+} oxidation upon CO_2 adsorption at CH_3O-MW(100)-red. At the same time, Ce(3d) XPS spectra (Figure 69b,d) collected after CH_3OH and then CO_2 adsorption at 30°C and 150°C showed: I) a partial increase of Ce^{3+} bands after CH_3OH adsorption, again difficult to distinguish from beam damage effect and II) a Ce^{3+} partial consumption after subsequent CO_2 adsorption, confirming as Ce^{3+}/CO_2 interaction occurred even on a methoxide-reach CeO_2 surface at 30 and 150°C i.e., reaction-like temperature, since formation of b'-OCH_3 did not oxidise Ce^{3+} species

4.4.3 Conclusions

Microwave-induced defectivity in CeO_2 was characterized by FTIR, UV-VIS, Raman and XP spectroscopies. MW(100) reducibility was observed at 150°C under H_2 and confirmed by CH_3OH adsorption to be selectively limited to the (101) and (100) planes . Together with CO adsorption and Ce^{3+} quantification exploited by XPS, these results confirmed formation of Frustrated Lewis Pairs sketched in Figure 70. Ce^{3+} $^2F_{5/2}\rightarrow{}^2F_{7/2}$ electronic transition, together with Ce^{3+}/Ce^{4+} CT and Ce^{3+}(3d) XPS spectra were employed as fingerprints to observe as: I) Ce^{3+} was not oxidised upon CH_3OH adsorption through formation of a bridged-methoxide group (b'-OCH_3) which preserved Ce^{3+}/V_O (Figure 70) i.e., keeping the FLP site intact and II) CO_2 reoxidised Ce^{3+} without either filling the V_O or producing CO. Ce^{3+}/CO_2 electronic interaction must then occur through formation of a negatively charged carbonate allowing Ce^{3+}-to-CO_2 charge redistribution preventing V_O occupation (Figure 70). Even if by IR

measurements it was not possible to isolate a single carbonate between the four reported in Figure 67, coupling IR with UV-Vis and XPS results we observed as b-CO_3^{2-}/h-CO_3^{-} ratio increased parallel to Ce^{3+} content in the order MW(100)-red > MW(100) > MW(650) > conv (650). Considering then that I) only one of the four carbonates identified in Figure 67 implied $CO_3^{=}$ formed over Ce^{3+}/V_O, II) bidentate carbonates abundance increased with Ce^{3+} content, III) Ce^{3+} fingerprints i.e., IR 2127 cm^{-1} band, Ce^{3+}/Ce^{4+} UV-Vis CT and Ce^{3+}(3d) peaks have been consumed after CO_2 adsorption and IV) V_O/CO_2 interaction was not observed by O 1S spectra, we can hypothesize as the carbonate 1.21' concentration increased with Ce^{3+} content reaching the highest concentration over MW(100)-red. Indeed, this bidentate carbonate would allow Ce^{3+}-to-CO_2 charge redistribution without filling the oxygen vacancy and corresponds to the one predicted in case of CO_2 adsorbed over FLP sites (Figure 70). We here then showed as the high Ce^{3+} concentration (>30%), usually considered as detrimental for CO_2 conversion to DMC, allows CO_2 and CH_3OH activation over Frustrated Lewis Pair to 1.21' b-CO_3 and b'-OCH_3 species, respectively, making CO_2 C atom more electrophilic, hence more prone to react with methoxide O atom to form MMC (Figure 70).

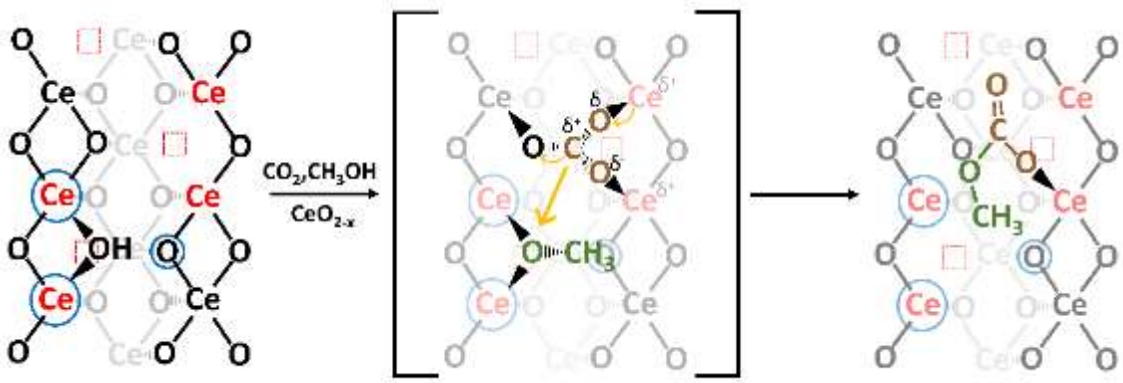

Figure 70 Sketched CO_2 (brown) and CH_3OH (green) reaction over CeO_2 surface with Ce^{4+} (black), Ce^{3+} (red), V_O (red squares) and FLP (blue circle) to form MMC.

References

(1) Daturi, M.; Binet, C.; Lavalley, J.; Sporken, R. Surface Investigation on CeZrO Compounds x -1-X2. *Phys. Chem. Chem. Phys.* **1999**, *1*, 5717–5724.

(2) Binet, C.; Daturi, M. Methanol as an IR Probe to Study the Reduction Process in Ceria-Zirconia Mixed Compounds. *Catal. Today* **2001**, *70* (1–3), 155–167. https://doi.org/10.1016/S0920-5861(01)00415-1.

(3) Jung, K. T.; Bell, A. T. An in Situ Infrared Study of Dimethyl Carbonate Synthesis from Carbon Dioxide and Methanol over Zirconia. *J. Catal.* **2001**, *347*, 339–347. https://doi.org/10.1006/jcat.2001.3411.

(4) Morterra, C.; Orio, L. Surface Characterization of Zirconium Oxide. II. The Interaction with Carbon Dioxide at Ambient Temperature. *Mater. Chem. Phys.* **1990**, *24* (3), 247–268. https://doi.org/10.1016/0254-0584(90)90089-S.

(5) Hertl, W. Surface Chemistry of Zirconia Polymorphs. *Langmuir* **1989**, *5* (1), 96–100. https://doi.org/10.1021/la00085a018.

(6) Pokrovski, K.; Jung, K. T.; Bell, A. T. Investigation of CO and CO2 Adsorption on Tetragonal and Monoclinic Zirconia. *Langmuir* **2001**, *17* (14), 4297–4303. https://doi.org/10.1021/la001723z.

(7) Taek Jung, K.; Bell, A. T. An *in Situ* Infrared Study of Dimethyl Carbonate Synthesis from Carbon Dioxide and Methanol over Zirconia. *J. Catal.* **2001**, *204* (2), 339–347. https://doi.org/10.1006/jcat.2001.3411.

(8) Katon, J. E.; Cohen, M. D. The Vibrational Spectra and Structure of Dimethyl Carbonate and Its Conformational Behavior. *Can. J. Chem.* **1975**, *53* (9), 1378–1386. https://doi.org/10.1139/v75-191.

(9) Behrendt, W.; Gattow, G.; Dräger, M. Über Chalkogenolate. LXI. Untersuchungen Über Halbester Der Kohlensäure. 1. Darstellung Und

Eigenschaften von Monomethyl- Und Monoäthylcarbonaten. *ZAAC - J. Inorg. Gen. Chem.* **1973**, *397* (3), 237–246. https://doi.org/10.1002/zaac.19733970303.

(10) Busca, G.; Lamotte, J.; Lavalley, J. ciaude; Lorenzelli, V. FT-IR Study of the Adsorption and Transformation of Formaldehyde on Oxide Surfaces. *J. Am. Chem. Soc.* **1987**, *109* (17), 5197–5202. https://doi.org/10.1021/ja00251a025.

(11) Ferrizz, R. M.; Wong, G. S.; Egami, T.; Vohs, J. M. Structure Sensitivity of the Reaction of Methanol on Ceria. *Langmuir* **2001**, *17* (8), 2464–2470. https://doi.org/10.1021/la001729o.

(12) Schilling, C.; Hofmann, A.; Hess, C.; Ganduglia-Pirovano, M. V. Raman Spectra of Polycrystalline CeO2: A Density Functional Theory Study. *J. Phys. Chem. C* **2017**, *121* (38), 20834–20849. https://doi.org/10.1021/acs.jpcc.7b06643.

(13) De Oliveira Jardim, E.; Rico-Francés, S.; Coloma, F.; Ramos-Fernández, E. V.; Silvestre-Albero, J.; Sepúlveda-Escribano, A. Superior Performance of Gold Supported on Doped CeO2 Catalystsfor the Preferential CO Oxidation (PROX). *Appl. Catal. A Gen.* **2014**, *487*, 119–129. https://doi.org/10.1016/j.apcata.2014.09.003.

(14) López, J. M.; Gilbank, A. L.; García, T.; Solsona, B.; Agouram, S.; Torrente-Murciano, L. The Prevalence of Surface Oxygen Vacancies over the Mobility of Bulk Oxygen in Nanostructured Ceria for the Total Toluene Oxidation. *Appl. Catal. B Environ.* **2015**, *174–175*, 403–412. https://doi.org/10.1016/j.apcatb.2015.03.017.

(15) Chen, A.; Yu, X.; Zhou, Y.; Miao, S.; Li, Y.; Kuld, S.; Sehested, J.; Liu, J.; Aoki, T.; Hong, S.; Camellone, M. F.; Fabris, S.; Ning, J.; Jin, C.; Yang, C.; Nefedov, A.; Wöll, C.; Wang, Y.; Shen, W. Structure of the Catalytically

Active Copper–Ceria Interfacial Perimeter. *Nat. Catal.* **2019**, *2* (4), 334–341. https://doi.org/10.1038/s41929-019-0226-6.

(16) Hadjiivanov, K. I.; Vayssilov, G. N. Characterization of Oxide Surfaces and Zeolites by Carbon Monoxide as an IR Probe Molecule. *Adv. Catal.* **2002**, *47*, 307–511. https://doi.org/10.1016/S0360-0564(02)47008-3.

(17) Badri, A.; Binet, C.; Lavalley, J. C. Use of Methanol as an IR Molecular Probe to Study the Surface of Polycrystalline Ceria. *J. Chem. Soc. - Faraday Trans.* **1997**, *93* (6), 1159–1168. https://doi.org/10.1039/a606628c.

(18) Siokou, A.; Nix, R. M. Interaction of Methanol with Well-Defined Ceria Surfaces: Reflection/Absorption Infrared Spectroscopy, X-Ray Photoelectron Spectroscopy, and Temperature-Programmed Desorption Study. *J. Phys. Chem. B* **1999**, *103* (33), 6984–6997. https://doi.org/10.1021/jp991127h.

(19) Vayssilov, G. N.; Mihaylov, M.; Petkov, P. S.; Hadjiivanov, K. I.; Neyman, K. M. Reassignment of the Vibrational Spectra of Carbonates , Formates , and Related Surface Species on Ceria : A Combined Density Functional and Infrared Spectroscopy Investigation. *J. Phys. Chem. C* **2011**, *115* (47), 23435–23454.

(20) Liu, B.; Li, C.; Zhang, G.; Yao, X.; Chuang, S. S. C.; Li, Z. Oxygen Vacancy Promoting Dimethyl Carbonate Synthesis from CO2 and Methanol over Zr-Doped CeO2 Nanorods. *ACS Catal.* **2018**, *8* (11), 10446–10456. https://doi.org/10.1021/acscatal.8b00415.

(21) Aresta, M.; Dibenedetto, A.; Pastore, C.; Cuocci, C.; Aresta, B.; Cometa, S.; De Giglio, E. Cerium(IV)Oxide Modification by Inclusion of a Hetero-Atom: A Strategy for Producing Efficient and Robust Nano-Catalysts for Methanol Carboxylation. *Catal. Today* **2008**, *137* (1), 125–131. https://doi.org/10.1016/j.cattod.2008.04.043.

(22) Aresta, M.; Dibenedetto, A.; Pastore, C.; Angelini, A.; Aresta, B.; Pápai, I. Influence of Al2O3 on the Performance of CeO2 Used as Catalyst in the Direct Carboxylation of Methanol to Dimethylcarbonate and the Elucidation of the Reaction Mechanism. *J. Catal.* **2010**, *269* (1), 44–52. https://doi.org/10.1016/j.jcat.2009.10.014.

(23) Mullins, D. R.; Robbins, M. D.; Zhou, J. Adsorption and Reaction of Methanol on Thin-Film Cerium Oxide. *Surf. Sci.* **2006**, *600* (7), 1547–1558. https://doi.org/10.1016/j.susc.2006.02.011.

(24) Beste, A.; Mullins, D. R.; Overbury, S. H.; Harrison, R. J. Adsorption and Dissociation of Methanol on the Fully Oxidized and Partially Reduced (1 1 1) Cerium Oxide Surface: Dependence on the Configuration of the Cerium 4f Electrons. *Surf. Sci.* **2008**, *602* (1), 162–175. https://doi.org/10.1016/j.susc.2007.10.024.

(25) Matolín, V.; Libra, J.; Škoda, M.; Tsud, N.; Prince, K. C.; Skála, T. Methanol Adsorption on a CeO2(1 1 1)/Cu(1 1 1) Thin Film Model Catalyst. *Surf. Sci.* **2009**, *603* (8), 1087–1092. https://doi.org/10.1016/j.susc.2009.02.010.

5 Aknowledments

The COZMOS project has received funding from the European Union's Horizon 2020 research and innovation programme under grant agreement 837733.

6 Appendix : list of published articles during the thesis

6.1 A : Ticali P., Salusso D., Catal. Sci. Technol., 2021,11, 1249

6.2 B : Salusso et al., J. Phys. Chem. C 2021, 125, 40, 22249–22261

6.3 C : Ramirez A., et al., JACS Au 2021, 1, 10, 1719–1732

6.4 D : Ruzzi et al., Applied Catalysis A, General 635 (2022) 118568

6.5 E : Barreau M. et al., Materials Today Chemistry 26 (2022) 101011